THERMAL FATIGUE OXIDATION AND SO_2 CORROSION OF AN ALUMINIDE-COATED SUPERALLOY

by

John W. Holmes

B.S./M.S., Pennsylvania State University (1981)
M.S., Massachusetts Institute of Technology (1983)

SUBMITTED IN PARTIAL FULFILLMENT
OF THE REQUIREMENTS OF THE
DEGREE OF

DOCTOR OF SCIENCE
IN MATERIALS SCIENCE AND ENGINEERING
at the

MASSACHUSETTS INSTITUTE OF TECHNOLOGY
September 1986

Signature of Author _____
Department of Materials Science and Engineering
September 1986

Certified by _____
Frank A. McClintock
Thesis Supervisor

Accepted by _____
Bernhardt J. Wuensch
Chairman, Departmental Committee on Graduate Students

Thermal Fatigue Oxidation and SO_2 Corrosion
of an Aluminide Coated Superalloy
by
John W. Holmes

Submitted to the Department of Materials Science and Engineering on September 4, 1986 in partial fulfillment of the requirements for the Degree of Doctor of Science in Metallurgy.

ABSTRACT

The effect of strain history and environment (air and SO_2-Na_2SO_4) on the degradation of an aluminide coating applied to a monocrystalline nickel-base superalloy (Rene N4) is examined. An experimental technique which allows simulation of the rapid heating rates and strain histories typical of gas-turbine airfoils is described. The technique utilizes high-frequency induction heating of anisotropic stepped-disk specimens and is suitable for both rapid screening tests and fundamental studies.

Tests performed in air show that both the compressive coating strain encountered on specimen heatup and the tensile strain encountered on cooldown critically affect aluminide coating degradation. After 6000 cycles of heating from 520 to 1080°C in 5 seconds followed by 30 second cooling, 80% coating penetration by scalloping was observed. A similar treatment with 6 second cooling resulted in alumina-filled coating cracks extending into the substrate.

Coating degradation by scalloping appears to be the result of initial oxide breakdown and surface roughening, followed by scallop growth due to a combination of cyclic creep and enhanced oxide cracking at the root of a scallop. Coating cracking appears to occur early in coating life, with subsequent depletion of Al along coating grain-boundaries, resulting in formation of Al-poor γ' films.

Tests performed in an environment that simulates the corrosive nature of turbine combustion gases (Na_2SO_4-SO_2-O_2) showed an acceleration of corrosive attack with increasing coating strain range. A mechanism for this increase in corrosion is proposed whereby oxide cracking results in direct interaction between the aluminide coating and Na_2SO_4 melt. This direct interaction increases the oxygen ion activity in the melt, resulting in precipitation of porous, non-protective, Al_2O_3.

Thesis Supervisor: Dr. Frank A. McClintock

Title: Professor of Mechanical Engineering

TABLE OF CONTENTS

LIST OF TABLES

LIST OF FIGURES

Nomenclature

B	bulk modulus
C_{mn}	stiffness constants [GPa]
E_C, E_{ox}	elastic moduli of polycrystalline CODEP coating and Al_2O_3 [MPa]
E_{100} , E_{110}	100 and 110 elastic moduli of substrate [MPa]
G_{100} , G_{110}	100 and 110 shear moduli of substrate [MPa]
n_j	moles of $j^{\underline{th}}$ gas component
P_j	partial pressure of $j^{\underline{th}}$ gas component
T	temperature, ^0C
α_C, α_{N4}, α_{ox}	mean coefficient of thermal expansion of CODEP coating, Rene N4, and Al_2O_3 oxide [$^0C^{-1}$]
δ	skin depth of magnetic field [mm]
ϵ_C , ϵ_S	elastic substrate, coating strain
ϵ_C , ϵ_S , ϵ_{ox}	total substrate, coating, oxide strain
f	frequency of induction generator [kHz]
μ_r	relative magnetic permeability
ρ	electrical resistivity of specimen [Ω-m]
σ_{ox}	oxide stress [MPa]
υ_{100}, υ_{110}	Poisson's ratio in 100 and 110 crystallographic directions

ACKNOWLEDGEMENTS

The author would like to thank his advisor, Prof. Frank McClintock, for the opportunity to conduct research at M.I.T and for his enlightening discussions and sense of humor.

The author is indebted to Prof. Turgay Erturk for his invaluable advice, encouragement and hospitality. The author also wishes to thank Prof. Samuel Allen and Prof. Walter Owen for their criticisms and comments both for this thesis and in regards to Courses 3.31 and 3.40.

The author is grateful for the consideration and helpfulness of technician, Mim Rich and microprobe operator Steve Recca. Special thanks also go to Kevin O'Hara of the General Electric Corp. in Lynn, Massachusetts for his help and time, to Esteban Busso for his help in the finite element work and to Carl Weiner for his excellent technical illustrations.

The author is truly indebted to Ann Jacoby of the Materials Science and Engineering Department who made this thesis possible. Her concern, encouragement and goodwill will be remembered always by the author.

The author would like to express his sincere thanks to Mary Jo Holmes for her technical assistance and for her help in editing of the text, and to his family for their continued patience and devotion.

The academic and research support provided by the National Science Foundation through Grant DMR 81-19295 is gratefully acknowledged.

Chapter 1

Introduction

Temperature History and Operating Environment For Advanced Gas Turbines

Cast monocrystal blades and vanes are currently used in advanced gas turbines. The improved high-temperature creep and thermal fatigue characteristics of the low modulus <100> oriented airfoils allow higher turbine operating temperatures and improved thermodynamic efficiency. Currently, the leading and trailing edges of first-stage blades and vanes can reach temperatures of 1100^{0}C during takeoff. During turbine operation, blades and vanes experience large thermal transients. For example, during takeoff of a jet-aircraft or helicopter the temperature along the leading and trailing edges of a first stage airfoil will increase from 500 to 1080^{0}C in 4 to 10 seconds. During turbine shutdown, after landing and thrust reverse, the temperature of first stage airfoils can decrease from 1080^{0}C to 500^0 in under 10 seconds. The maximum temperature encountered by second stage airfoils is approximately 950^{0}C.

Combustion gas composition. The air to fuel ratio of a gas turbine is typically 50:1, making the combustion gas very oxidizing. Under cruise conditions, typical mole fractions of exhaust gas constituents for a turbine burning petroleum fuel

would be 0.15-0.20 O_2, 0.73 N_2, 0.03-0.05 CO_2 and H_2O, 10^{-4} to 10^{-6} SO_2, and 10^{-6} to 10^{-7} Na_2SO_4. Other hydrocarbons (C_xH_y) and nitrous oxides (NO_x) are also present but at much lower concentrations. In addition, depending on operating environment, fuel and inlet air can contain the elements Na, Mg, Ca, and Si as well as the anions Cl^- and SO_4^{2-}.

Aluminide Coatings

For protection against oxidation and hot-corrosion attack, aluminide coatings are commonly applied to gas turbine blades and vanes. These coatings are formed by reacting the airfoil surface with aluminum to form the intermetallic NiAl, thus enriching the surface in aluminum. The NiAl layer is itself protected by the formation of an Al_2O_3 layer upon high temperature exposure of the coated component. As a result of high metal temperatures and the thermal strains due to temperature transients and internal blade cooling, coating degradation has become a dominant life-limiting phenomenon for gas turbine blades and vanes.

Structure of coating. Aluminide coatings consist of two zones (Fig. 1): a fine-grained internal zone, and a large grained external zone. The thickness of each of these zones is typically 25 to 50 microns, depending upon coating technique and specimen dimensions. For a coating formed by a low activity process [1], the internal zone is comprised of fine equiaxed grains (≈5μm) and

contains precipitates of those substrate elements that cannot be completely dissolved in the NiAl matrix during coating formation. The external zone is comprised of large columnar grains (≈40μm) which contain substrate elements up to their solubility limit in NiAl. Diffusion of substrate elements (e.g., Cr, Ti, W, Ta, Mo, Co) into the coating can influence its oxidation characteristics and mechanical properties.

Coating degradation. The primary causes of aluminide coating degradation are cracking, oxidation, and corrosive attack by molten sodium sulfate (hereafter referred to as hot-corrosion). Thermal fatigue can cause accelerated coating oxidation by the repeated spalling or cracking of the protective Al_2O_3 that forms on the coating during high temperature exposure. Hot corrosion is of concern when gas turbines are operated in sea-air environments. In these environments, sodium present in the air or fuel can combine with SO_2 to form Na_2SO_4 by the reaction:

$$2Na(v) + SO_2(g) + O_2(g) = Na_2SO_4(v)$$

$Na_2SO_4(v)$, which condenses on turbine vanes and blades at temperatures of 850 to 1000°C, can dissolve the protective Al_2O_3 oxide by, for example, the reaction

$$Na_2SO_4(l) + Al_2O_3 = 2NaAlO_2(l) + SO_2 + (1/2)O_2$$

After dissolution of the protective oxide by Na_2SO_4 , accelerated oxidation and sulfidation of the coating and substrate can occur.

In the first stage of an advanced gas turbine, where the temperature along the leading and trailing edges of airfoils is in excess of 1080^{0}C, coating oxidation is the dominant degradation mechanism. In the second and third stages, where airfoil temperatures are usually below 950^{0}C, hot-corrosion attack of the aluminide coating is the dominant coating degradation mechanism. The temperature dependence of the degradation mechanisms can be rationalized with reference to Fig. 2. The partial pressure of sodium sulfate in the combustion gas of a turbine is typically below 10^{-6} atm. Thus, sodium sulfate will not condense on first stage airfoils, where the gas stream temperature is in excess of 1300^{0}C and airfoil temperatures are above 1080^{0}C. However, the combustion gas cools as it expands, and the gas temperature drops to below 1100^{0}C by the time it reaches the second-stage airfoils. This lower gas temperature, and the corresponding lower airfoil temperatures (<950^{0}C) encountered in the lower stages, allow the condensation of Na_2SO_4 onto airfoil surfaces (note that at 900^{0}C the equilibrium vapor pressure of Na_2SO_4 is $\approx 10^{-7}$atm).

Thesis Objective

The overall goal of this thesis is to develop an experimental technique that allows studying the effects of strain history and

environment on protective coating durability and to apply the technique developed to a coated monocrystalline superalloy of current interest. The stress-strain histories, temperatures, and environments are chosen to allow characterization of the selected coating/substrate system for a variety of operating conditions occurring in a gas-turbine.

Two results distinguish this work from that of others [2-8]:

(1) the successful development of a low-cost experimental technique that can be used to characterize coating degradation for a variety of coating/substrate systems and environments and,

(2) correlation of coating degradation mechanisms with the *strain history* experienced by test specimens.

Thesis Synopsis

Induction heating of disk specimens as an improved alternative to the use of fluidized beds or gas burner rigs in thermal fatigue studies is discussed in Chapter 2. To illustrate the versatility of the technique, the influence of strain history on the durability of an aluminide coating applied to a monocrystalline nickel-based superalloy is studied in air. Also discussed in Chapter 2 are results obtained from a thermoelastic finite-element analysis for the stress-strain history of the disk specimens.

The simultaneous thermal-strain cycling and oxidation tests of Chapter 2 resulted in surface roughening and grain boundary cracking of the aluminide. The mechanisms responsible for these two modes of coating degradation are examined in Chapter 3 by correlation of coating stress-strain history with the results of microprobe analyses for changes in coating composition occurring as a result of thermal exposure and thermal-strain cycling.

The effect of a corrosive $Na_2SO_4/SO_2/O_2$ environment on aluminide coating degradation is examined in Chapter 4. The environment, temperature history, and strain history are chosen to roughly simulate the third-stage gas-turbine operating environment. A possible mechanism for the acceleration of coating degradation observed with thermal-strain cycling in the corrosive $Na_2SO_4/SO_2/O_2$ environment is discussed in detail.

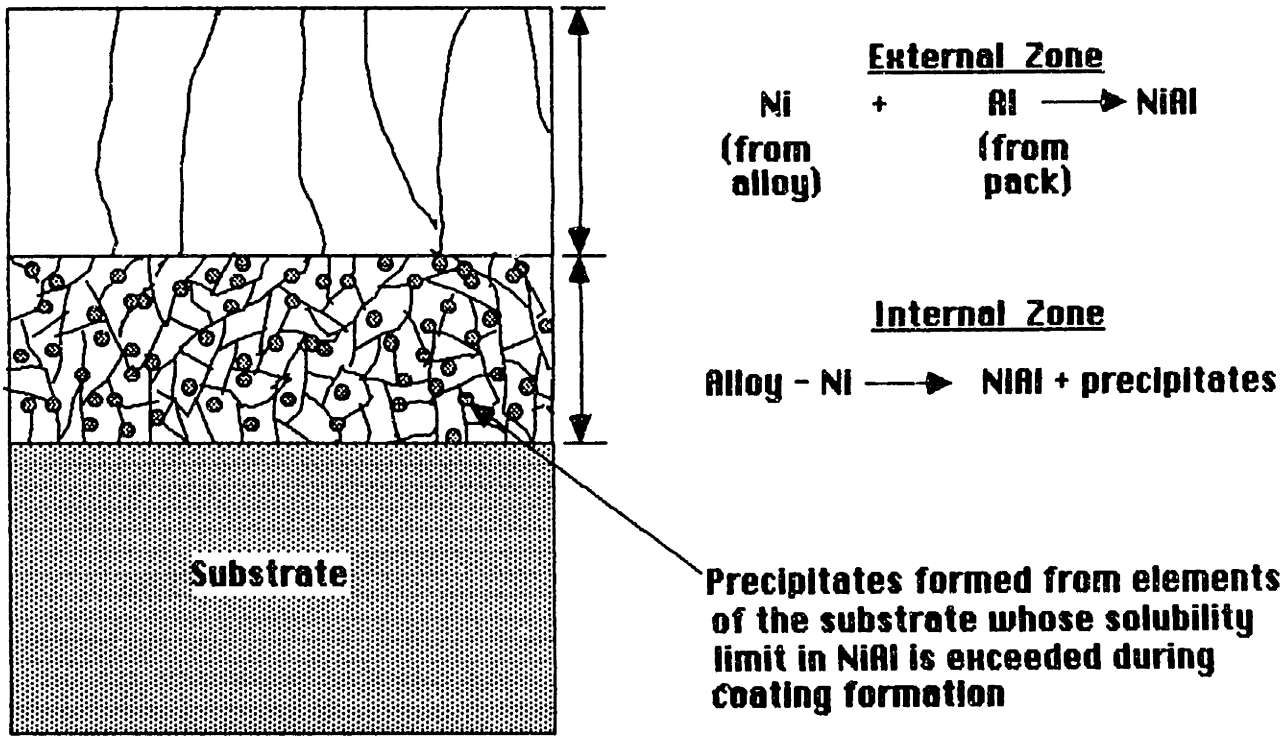

Fig. 1 Schematic illustration of an aluminide coating formed on a nickel-base superalloy (low activity coating process).

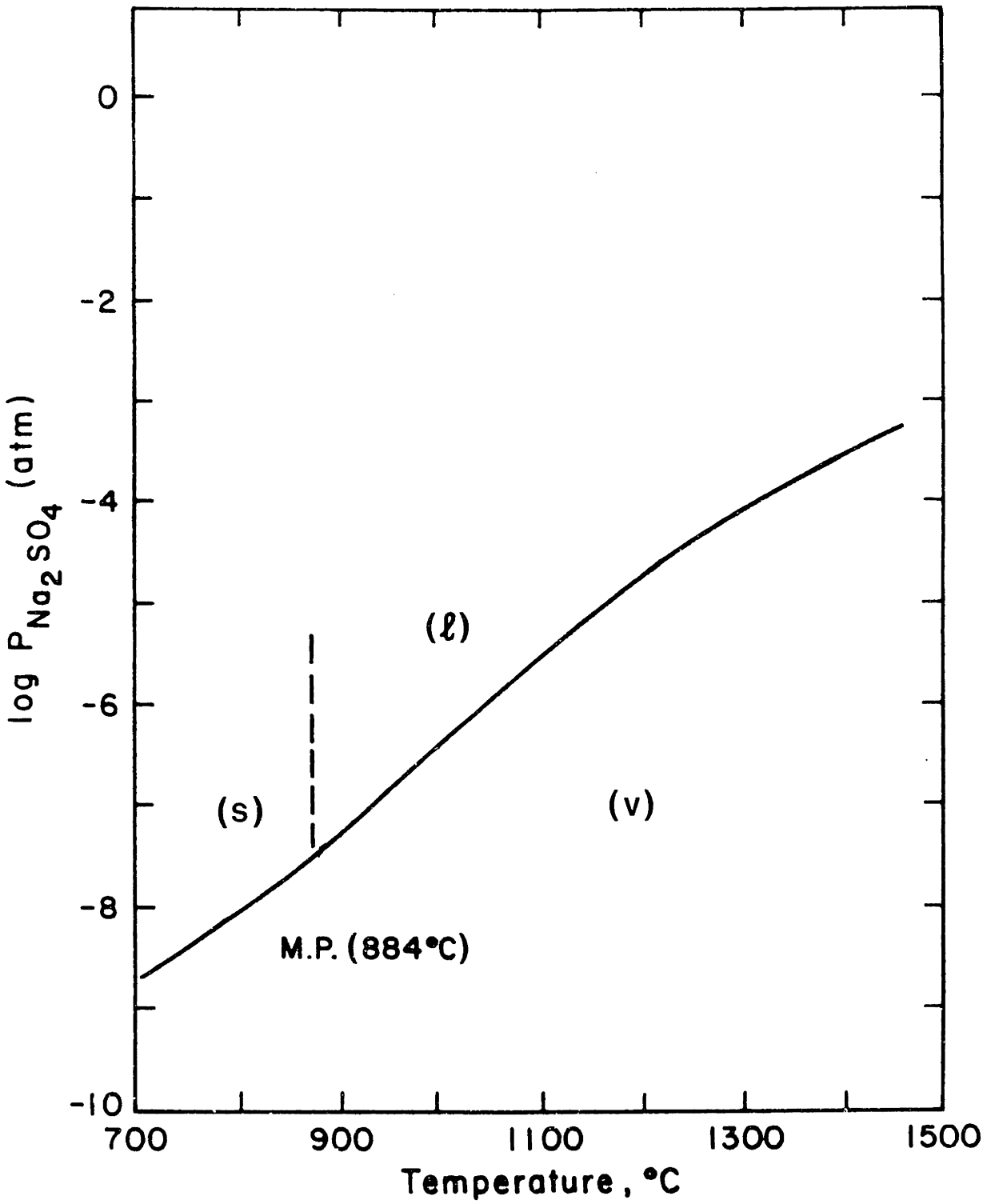

Fig. 2 Vapor pressure of sodium sulfate. After Elliot [9].

Chapter 2

Thermal Fatigue Testing of Coated Monocrystalline Superalloys

Abstract

Induction heating of stepped-disk specimens to study thermal fatigue of coated superalloys is well suited for studying anisotropic alloys, and is easily adaptable for corrosive or inert atmosphere testing. Details of the experimental apparatus and results of a thermoelastic finite element analysis to find the stress-strain history are given.

To illustrate the technique, the effect of cyclic thermal strains on the durability of an aluminide coating applied to a typical monocrystalline nickel-base superalloy was studied in air. Results show that both the compressive strain encountered on specimen heatup and the tensile strain encountered on cooldown critically affect the aluminide coating degradation. After 6000 cycles of heating from 520 to 1080^{0}C in 5 seconds followed by 30 second cooling, 80% coating penetration by scalloping was observed. A similar treatment with 6 second cooling resulted in alumina-filled "cracks" extending into the substrate.

Introduction

Coated monocrystal blades and vanes are currently used in

advanced gas turbines. The improved high-temperature creep and thermal fatigue characteristics of the low modulus <100> oriented airfoils allow higher turbine operating temperatures and improved thermodynamic efficiency.

Currently, the leading and trailing edges of first stage blades and vanes can rise from 500 to 1100^{0}C in 4 to 10 seconds during takeoff. During turbine shutdown, after landing and thrust reverse, the airfoil temperature can decrease from 1080 to 500^{0}C in under 10 seconds. As a result of high metal temperatures and the thermal strains due to temperature transients and internal blade cooling, coating degradation has become a dominant life-limiting phenomenon for gas turbine blades and vanes.

The properties of a substrate is in many cases affected by the presence of a protective coating and the thermal cycles associated with coating application [10-14]. The oxidation, corrosion, and mechanical properties of the protective coating itself are strongly influenced by substrate composition due to diffusion of substrate elements into the coating during coating application or interdiffusion between the coating and substrate during high-temperature exposure [15-19]. Therefore, when determining the mechanical behavior of a substrate, or the merit of using a specific coating, the substrate and coating should be examined as a unit. This testing should take into consideration the temperature and strain history of the coated component, as

well as the operating environment.

Currently there are several techniques available for studying the effect of thermal fatigue on coating-substrate durability. These include gas-burner rigs [20,21,22] and fluidized beds [23,24,25]. Gas-burner rigs suffer from high costs and a complex heat-transfer analysis, which makes it difficult to correlate coating durability with the stress-strain history of test specimens. The fluidized bed technique of studying thermal fatigue has two serious drawbacks: (1) incompatibility with corrosive atmosphere testing, and (2) lack of versatility in studying arbitrary temperature histories or mission profiles due to lack of easy control over specimen heating and cooling rates. (For a given maximum and minimum bed temperature, changing the heating or cooling rate of a specimen requires a change in specimen dimensions or geometry.) Thermo-mechanical fatigue tests are expensive and limit heating times to the order of a minute.

Induction heating of stepped-disk specimens is an alternative to the use of burner rigs and fluidized beds in thermal fatigue studies. The induction heating technique [26] allows one to subject test specimens to a variety of temperature and strain histories typical of those encountered by the leading and trailing edges of gas turbine blades and vanes. The technique is also easily modified to allow thermal fatigue testing in inert or

corrosive gas atmospheres (see Chapter 4).

In this chapter, the induction heating technique is illustrated by studying the effect of strain history on the degradation of an aluminide-coated Ni-base superalloy (Rene N4 [27,28]).

Experimental Procedure

Test Specimens. The constant thickness disk specimens used in an earlier feasibility study [26], have been changed to stepped-disk specimens (Fig. 3) to allow periphery radii typical of the trailing edge of a gas turbine airfoil. In addition, the decrease in thermal mass along the disk periphery allows modeling of the 4 to 10 second heating and 6 to 30 second cooling experienced by the edges of internally cooled gas turbine airfoils.

For the present study, specimens were machined from a single crystal rod of Rene N4 such that their faces were normal to the [001] crystal growth direction (see Fig. 3). Due to the anisotropic elasticity of the specimen substrate the strain history along the specimen periphery is a function of angular position, varying from a maximum along <100> directions to a minimum along <110> directions. Thus, this specimen orientation, which includes four radial <100> and <110> directions, allows use of a single specimen to study thermal fatigue of the coating under the different strain amplitudes developed along the specimen periphery.

Alloy composition, heat-treatment, and coating. The chemical composition of the monocrystalline Rene N4 used in this study is given in Table 1. Prior to the machining and coating operations, the 19 mm diameter crystal rod was given a solutionizing heat treatment in vacuum: 1270°C for 2 hr, followed by furnace cooling (average cooling rate measured at the surface of the rod was 40°C/min to 500°C).

After machining, specimens were aluminide coated [29,30]. The coating was applied by a low-activity pack-aluminization technique (CODEP B-1). The coating cycle was: 1050°C for 4 hr in argon followed by cooling to 25°C. To obtain the correct substrate microstructure after aluminization, specimens were heated in vacuum to 1050°C, held for 15 minutes, then cooled to 25°C in 5 minutes. Specimens were next aged for 16 hours at 870°C in vacuum.

Test apparatus. Thermal fatigue was obtained by inductively heating stepped disk specimens (Fig. 3) around their peripheries using a Lepel[1] solid state 2.5kw (450kHz) induction generator coupled to a plate concentrator coil (see [26], Figs. 4a,b, 5, and 6). This technique relies on the skin effect obtained with high frequency induction heating of metals (at 450 kHz the skin

---

[1]Lepel Corporation Model #T-2.5-1-KC1-B3W-T; supplied with a Research Incorporated Set-Point Programmer Model #73211 and a West Temperature Controller Model #1646A-1-9441A.

depth obtained in nickel-base superalloys is approximately one millimeter[2]. The concentrator coil is constructed with 5 turns of 3.2 mm diameter copper tubing, and has a base-plate thickness of 1.5 mm. The base-plate was machined with an 0.3 mm wide air-gap, which extends from the inner to outer base-plate radii. To prevent arcing, the air-gap was insulated with teflon. The central hole in the concentrator plate is 22 mm in diameter, which gives an air gap of 2.5 mm between the concentrator coil base-plate and specimen periphery.

Specimens are positioned in the induction coil using 304 stainless steel support-rods attached to aluminum forced-air cooling manifolds[3] (see Figs. 5,6). The support-rods thread

---

[2]The skin depth (the depth at which the strength of the magnetic field falls to 0.3679 of its surface value) is given by $\delta = \sqrt{(\rho/4\pi^2\times10^{-7}f\mu_r)}$ where, ρ = resistivity [Ω-m], f = frequency [Hz], and μ_r = relative permeability (=1 for non-magnetic materials).

[3]Due to the close proximity of the cooling manifolds to the specimen surface and induction coil, radiation from the specimen and fringing of the magnetic field cause heating of the manifolds. For the aluminum manifolds used the maximum manifold temperature reached was 350°C (for a specimen temperature of 1080°C). Had the manifolds been constructed of a metal of higher resistivity (e.g., stainless steel or nickel) the magnetic-field fringing would have resulted in much higher manifold temperatures, which could result in fatigue damage of the cooling manifolds. The expected increase in manifold temperature with resistivity was shown by tests with a 304 stainless steel manifold; for a specimen temperature of 1080°C the stainless steel manifold reached a temperature of 750°C versus 350°C for the aluminum manifold.

together where they pass through the specimen center. The support-rods also serve as heat-sinks for maintaining a radial temperature gradient in the specimen. Heat transfer from the specimen core to the support-rods is aided by passage of cooling air through the core of the support rods. The cooling manifolds were designed such that high velocity air (up to 200 m/s), exiting from a 0.17 mm gap in a circular annulus 2.5 mm from the specimen surface, impinged directly on the reduced thickness periphery. Varying the airflow thru the annulus allows control of the tensile strains encountered during the cool-down portion of the temperature cycle. A microprocessor-based temperature controller was used to give automatic control of the induction generator and the on/off air supply to the cooling manifolds.

The rapid temperature transients (Figs. 7a,b,c,d) and the dependence on measured temperatures in the specimen stress-strain analysis, necessitated the use of extreme care in using thermocouples for temperature measurement and control. As described below, the accuracy and response time of the thermocouple measurements was improved by maximizing the contact area between the thermocouple-junction and specimen surface and by using fine-gage thermocouples with low thermal-mass junctions.

To increase the contact area between the thermocouple junction and specimen and to position the thermocouples

accurately on the specimen, 0.3 mm diameter by 0.15 mm deep holes were drilled at specimen radii of 3.5, 4.0, 5.0, 6.0, and 6.5 mm. Fine-gage chromel-alumel thermocouples (0.13 mm wire diameter) with 0.3 mm diameter ball-junctions were then spot-welded into these positioning holes. It was undesirable to locate thermocouple positioning holes along the highly stressed periphery (radius = 7.15 to 8.5 mm). Therefore, to optimize the response time and accuracy of temperature measurements made in this region, the thermocouple junctions were thinned prior to attachment such that the overall junction size measured 0.3 mm square by 0.1 mm thick. For the temperatures of interest in this study (up to 1080^{0}C) the 0.13 mm diameter chromel-alumel thermocouples could be used for only 25 hr before oxidation led to reading errors and embrittlement. Therefore, for long-term feedback to the temperature controller, a Pt/Pt-10% Rh thermocouple (0.20 mm wire diameter) was positioned at a specimen radius of 6.5 mm.

To ensure that the specimens heated uniformly, six thermocouples were located 60^{0} apart at a distance of 2 mm from the specimen periphery. The specimen was positioned such that one of these thermocouples was adjacent to the base-plate air-gap. The lateral position of the specimen relative to the coil was then adjusted[4] until the temperature difference between these six thermocouples was less than 5^{0}C.

In contrast to other coil geometries (e.g., helical coils), the magnetic field produced by the plate concentrator coil did not interfere with temperature measurements. The thermocouple temperature measurements were found to be within 2.1% of the temperatures indicated by an optical pyrometer (width of pyrometer filament = 0.8 mm) and within 1.1% of the temperature indicated by melting point standards applied to the specimen by stencil and airbrush as 0.5 mm wide annular rings.

For the particular specimen geometry and control system used, the system could be tuned to allow periphery heating from 520 to 1080^{0}C in 3 seconds with less than a 2.5% overshoot in temperature. Cooling from 1080^{0}C to 520^{0}C was possible in as little as 4 seconds with a 3% overshoot in temperature. For the 520 to 1080^{0}C temperature range of interest in this study the response time of the thermocouple/chart-recorder system used to record temperature history was less than 0.3 seconds.

---

[4]Due to the reduction in magnetic field intensity near the 0.3 mm wide air-gap in the concentrator-coil base-plate, uniformity of periphery heating was improved with the specimen offset approximately 0.8 mm from the geometric center of the base-plate hole, towards the base-plate air-gap. The variation in circumferential periphery temperature was approximately 25^{0}C with the specimen centered in the coil, versus 5^{0}C with the specimen offset. Uniformity of heating can be improved by increasing the specimen-to-base-plate air-gap. However, efficiency decreases with increasing specimen-to-base-plate air-gap. Magnetic-field fringing effects are also accentuated by increasing this air-gap.

Thermal fatigue tests. To determine the effect of strain history on coating oxidation and cracking, four different periphery temperature histories were used; all with minimum temperatures of 520°C and a 60 s hold at 1080°C:

Heating Time (s)	Cooling Time (s)	Figure
5	30	7a
8	30	7b
35	30	7c
8	6	7d

The strain histories corresponding to these temperature histories are discussed in the next section. The rapid heating of Figs. 7a,b and slow heating of Fig. 7c are included to show how the magnitude of the compressive periphery strains, encountered during specimen heatup, affect coating durability. The slow cooling of Fig. 7b and the fast cooling of Fig. 7d (30s versus 6s) are included to show the effect of tensile strains on coating durability.

Stress and strain history of test specimens.

The thin skin analysis used in [26], which assumes an abrupt change in radial temperature between the specimen periphery and core, was found to be inadequate for the diffuse radial

temperature gradients encountered in this study, since it does not account for core deformation which can have a large effect on strain history. It was therefore necessary to perform a thermoelastic finite element analysis to obtain more accurate stress-strain histories of the induction heated specimens.

Finite-element model. The elastic stress-strain history of the test specimens was determined using the finite-element program ABAQUS [31]. To determine if it was appropriate to use generalized plane-stress elements for the stress-strain analysis of the stepped-disk specimen, an axisymmetric z-r isotropic mesh with the actual specimen thickness was compared to the same mesh with a thickness 10% as large. The results show that, except in the step itself, the through-the-thickness stresses were negligible and the circumferential stresses agreed within 3% .

Due to symmetry, it was only necessary to model a 45^0 octant of the anisotropic stepped-disk specimen. The 136 element mesh used (Fig. 8) was made up of 8-node bi-quadratic plane-stress elements, each with nine Gaussian integration points. The element width near the hole was chosen to ensure that the stress concentration at the specimen-hole, linearly extrapolated from integration points, would be accurate to within 1% . To maintain symmetry, the displacements of all nodes along the <100> and <110> radial directions were constrained to the radial direction

and the shear stresses were set to zero.

The finite element analysis was simplified by noting that the thin coating (<0.1 mm versus a specimen radius of 8.5 mm) gives negligible constraint. It can therefore be assumed that the coating undergoes the same strain history as the substrate periphery. Prior to yielding of the coating, the stress history of the coating differs by the ratio of the elastic moduli of the coating and substrate. For the temperature range 25°C to 1100°C the elastic modulus of the coating is approximately 40% higher than the <100> elastic modulus of the substrate and approximately 20% lower than the <110> substrate modulus. As Rene N4 and CODEP B-1 coating have similar thermal expansion coefficients (Table 2) over the temperature range of interest, the effect of thermal expansion mismatch on coating stress history would be small in comparison to elastic modulus effects.

Material properties. The stiffness constants and mean coefficient of thermal expansion of Rene N4, which are required as input data for the finite element program, are given in Fig. 9 and Table 2, respectively. The original data for elastic moduli and Poisson's ratio, determined by an ultrasonic technique, indicated an abrupt increase in bulk modulus for temperatures greater than 870°C (see Appendix A). This abrupt increase in bulk modulus was due to Poisson's ratio approaching 0.5, apparently caused by inelasticity present even at the 5000 Hz at

which the data were taken. To circumvent this problem, the bulk modulus B versus temperature was extrapolated upward from 870°C, and these extrapolated values were used to normalize E_{100} and G_{100}. E_{100}/B and G_{100}/B were then extrapolated in Fig. A2 (Appendix A) to obtain the corrected values for E_{100} and G_{100} as a function of temperature. These corrected values were then used to obtain the stiffness constants C_{mn} of Fig. 9. (In ABAQUS [31] the stiffness constants are denoted E_{ijkl}.) A run with isotropic values of the stiffness constants in the orthotropic finite element program gave results identical to the isotropic solution.

Temperature history. As described earlier, the temperature history of the test specimens was determined from thermocouple data. Because of the radial heating and thin specimen (only 1.8 mm), it was assumed that there was no temperature gradient through the thickness of the specimens.

Results of thermoelastic finite element analysis. The circumferential periphery stress and strain histories along the <100> and <110> substrate orientations for the different heating and cooling rates of Figs. 7a,b,c,d are given in Figs. 10a,b,c,d. (Sample input and output files for the finite element analysis are given in Appendix B.) Note that the loops are caused by the interaction of anisotropy and the changing thermal strains in the core relative to the periphery and not by material hysteresis. For the rapid heating rates of Figs. 7a,b,d, the maximum

circumferential compressive strain in the periphery occurs along the <100> directions at 1053°C and decreases as the specimen core increases in temperature. For the slow heating rate of Fig. 7c, where the transient radial temperature gradient is minimized, the peak circumferential compressive strain occurs at the peak temperature of 1080°C. Prior to substrate yielding[5], the coating stress along the <100> directions will be 40% higher than the substrate, due to the modulus differences mentioned above. Cyclic stress-strain data for stress in the aluminide coating could not be found.

Results and Discussion

After completion of testing, specimens were nickel-plated and then ground parallel to their faces, down to the mid-plane. The specimens were next diamond polished to a final finish of 0.25μm.

---

[5]The results of this analysis assume entirely ***elastic*** substrate behavior. For the moderate heating rate of Figs. 8b,d data supplied by General Electric, Lynn Massachusetts, shows that the initial compressive yield strength of Rene N4 (0.1% offset, 1093°C) is exceeded by approximately 8.5% along <100> directions. This data also shows that for a total strain range of 0.40% the widths of the 1093°C hysteresis loops increased from an initial value of 0.05% to a maximum of 0.15% at 1000 cycles. It is important to note that inelastic strains in the thin periphery will have relatively little effect on the circumferential strains induced by the thicker core of the specimen.

The backscattered-electron micrographs of Figs. 11a-h show two distinct types of coating degradation: surface scalloping and through thickness cracking. These micrographs clearly show the greater degree of coating degradation obtained along <100> periphery directions compared to the <110> directions. The initial coating was found to be isotropic in microstructure with substrate crystallographic orientation. In addition, a microprobe analysis along the circumference of an as-coated specimen showed no variation in coating composition with substrate orientation. Thus, the difference in coating degradation with substrate orientation can be attributed to the larger substrate strains and hence larger coating strains along <100> directions, consistent with the thermoelastic analysis.

The compressive periphery strain encountered during specimen heating produced degradation in the form of scalloping at the scale of the coating grain size (Figs. 11a-f). The 5s heating of Fig. 7a, which gave the largest compressive periphery strains (0.56%), caused severe scalloping, with oxidation attack extending to approximately 80% of the coating thickness along <100> directions. The moderate (8s) heating of Fig. 7b (0.45% compressive strain) resulted in <100> scalloping extending to 50% of the coating thickness. The slow (35s) heatup of Fig. 7c (0.20% compressive strain) produced very little coating degradation.

Tensile periphery strain increments were produced by decreasing the cooling time from the 30s of Fig. 7b to 6s (Fig. 7d). This rapid cooling gave tensile strains of 0.20% along <100> peripheries and resulted in crack-like defects extending into the substrate (Figs. 11g,h). Microprobe analysis showed these defects to be alumina-filled. This "cracking" is to be compared with the coating scalloping (Fig. 11c,d) found after the 30s cooling of Fig. 7b.

Conclusions

1. Induction heating of stepped-disk specimens provides a versatile technique for studying the thermal fatigue degradation of coated anisotropic materials. The apparatus can heat low thermal mass disk specimens through a temperature difference of 600^{0}C in as little as 3s, with less than a 2.5% overshoot in temperature. The cooling rate of the specimen can be varied to obtain rates as rapid as a 600^{0}C drop in temperature in 4s. In addition to allowing the study of the effect of a wide variety of temperature histories, the technique can also be modified (by use of a 22 mm o.d. x 19 mm i.d. length of quartz tube for atmosphere containment) to study the effect of corrosive or inert atmospheres on coating or substrate durability.

2. 6000 thermal cycles, between a peak compressive substrate strain of -0.56% at 1080^{0}C and a peak tensile strain of 0.03% at 590^{0}C, gave coating scalloping to 80% of the coating thickness,

but did not cause coating or substrate cracking. For 6000 cycles between a peak compressive strain of 0.20% at 1080^{0}C and a peak tensile strain of 0.01 at 590^{0}C no coating scalloping was observed.

4. 6000 thermal cycles between a peak compressive substrate strain of -0.45% at 1080^{0}C and a peak tensile strain of 0.20 at 750^{0}C, resulted in alumina-filled coating "cracks" extending into the substrate.

TABLE 1 - Chemical composition of Rene N4 (weight percent).

Al	Cb	Cr	Co	Cu	Fe	Hf	Mo	Ni	Ta	Ti	V	W
3.7	0.5	9.3	7.5	0.1	0.2	0.1	1.5	Bal	4.0	4.2	0.1	6.0

TABLE 2 - Mean coefficient of thermal expansion versus temperature for Rene N4 and CODEP coating. (Values given are for a reference temperature of 25°C.)

Temperature, °C	α_{N4}, $^{o}C^{-1}$ (Rene N4)	α_{C}, $^{o}C^{-1}$ (CODEP)
100	11.97×10^{-6}	---
200	12.06	---
300	12.15	---
400	12.51	---
500	12.78	13.82×10^{-6}
600	13.14	14.04
700	13.41	14.31
800	13.97	14.47
900	14.62	14.78
1000	15.41	15.39
1100	16.52	16.41

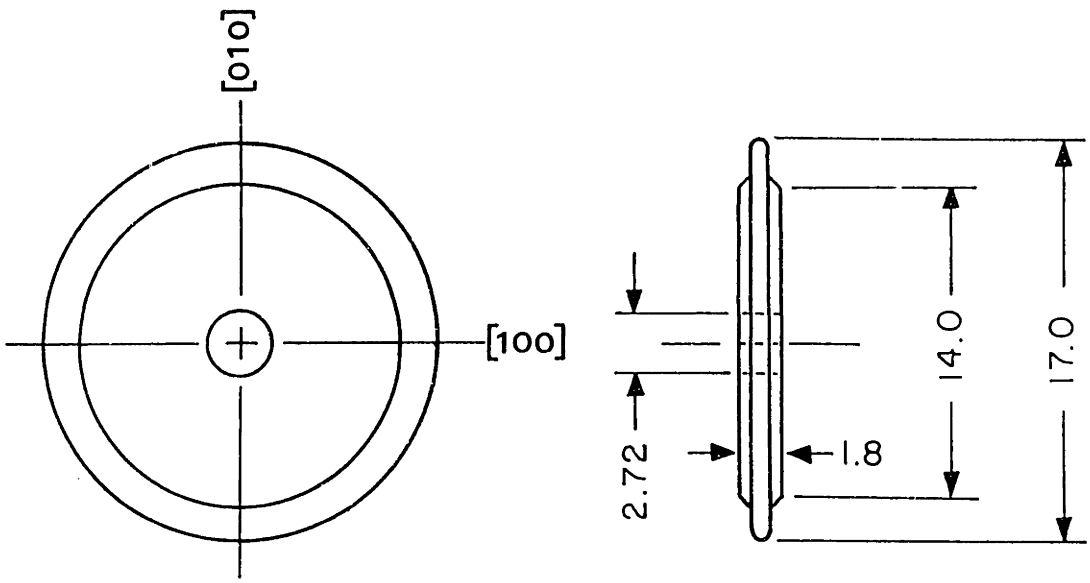

(a) specimen geometry

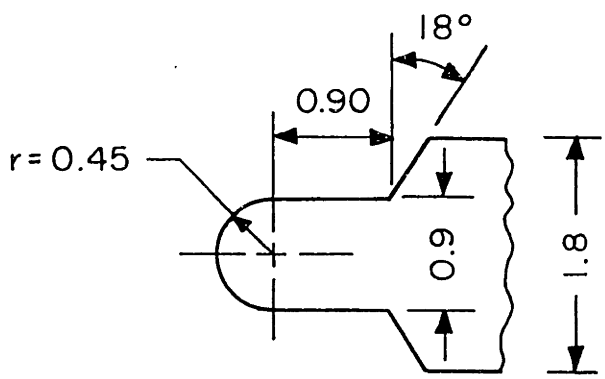

(b) detail of specimen periphery

Fig. 3 Detailed drawing and orientation of stepped-disk specimen used in coating durability studies. All dimensions in millimeters.

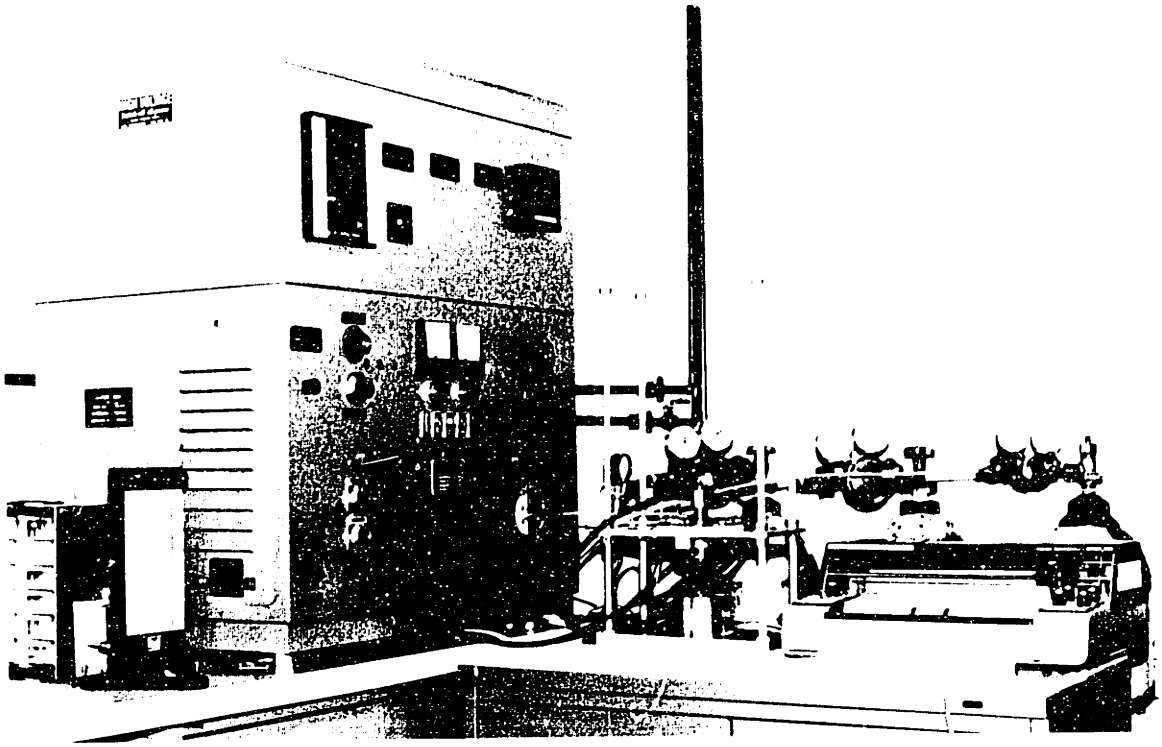

(a) Overall view of experimental setup.

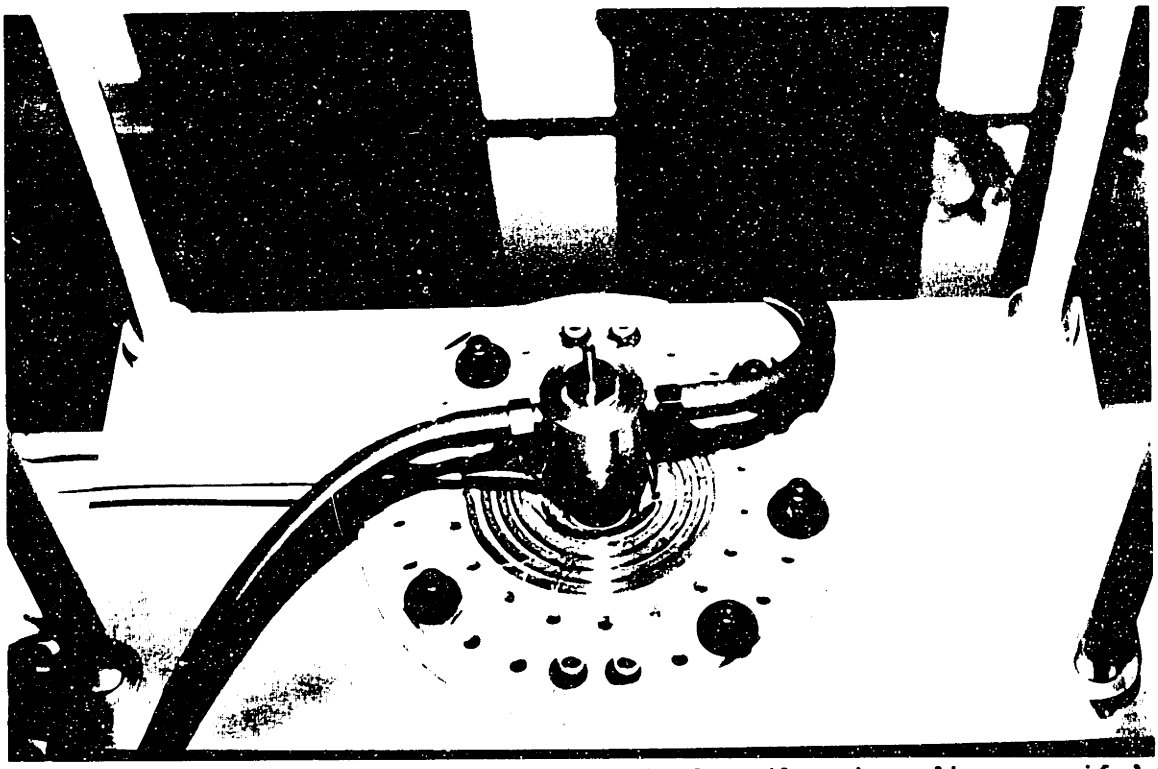

(b) Top view of apparatus showing spiral-coil and cooling manifold.

Fig. 4a,b Pictures of induction heating apparatus used to study thermal fatigue of coated monocrystals.

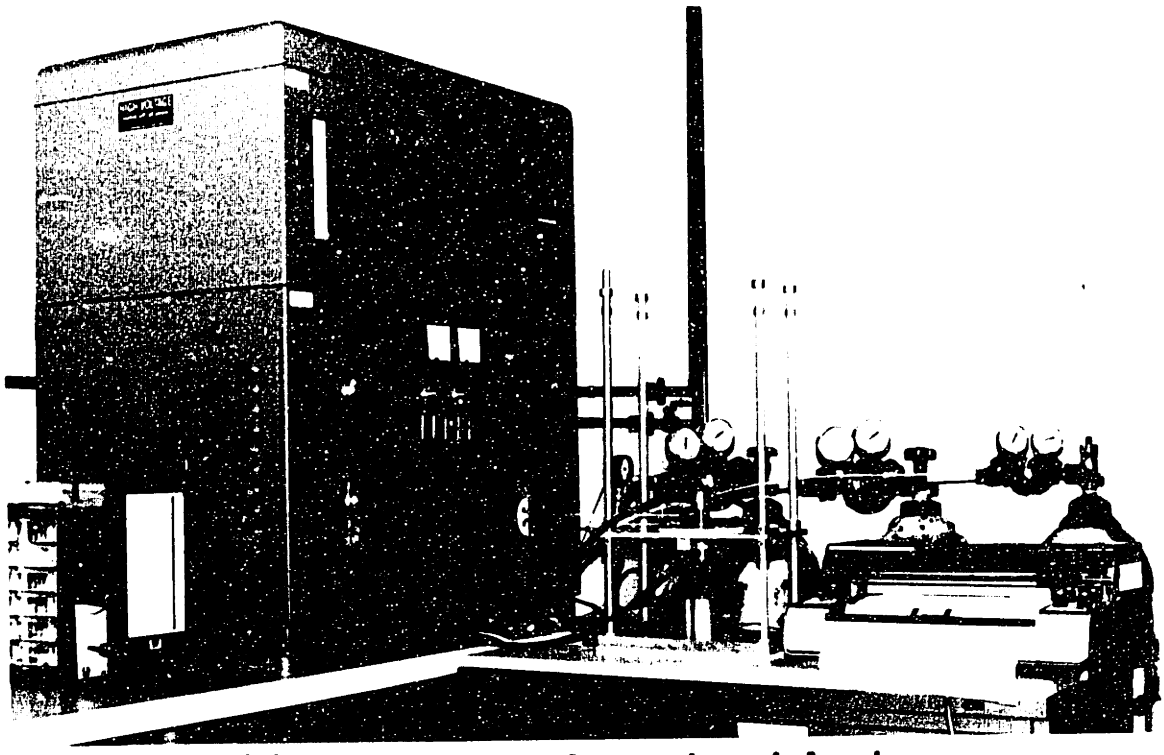

(a) Overall view of experimental setup.

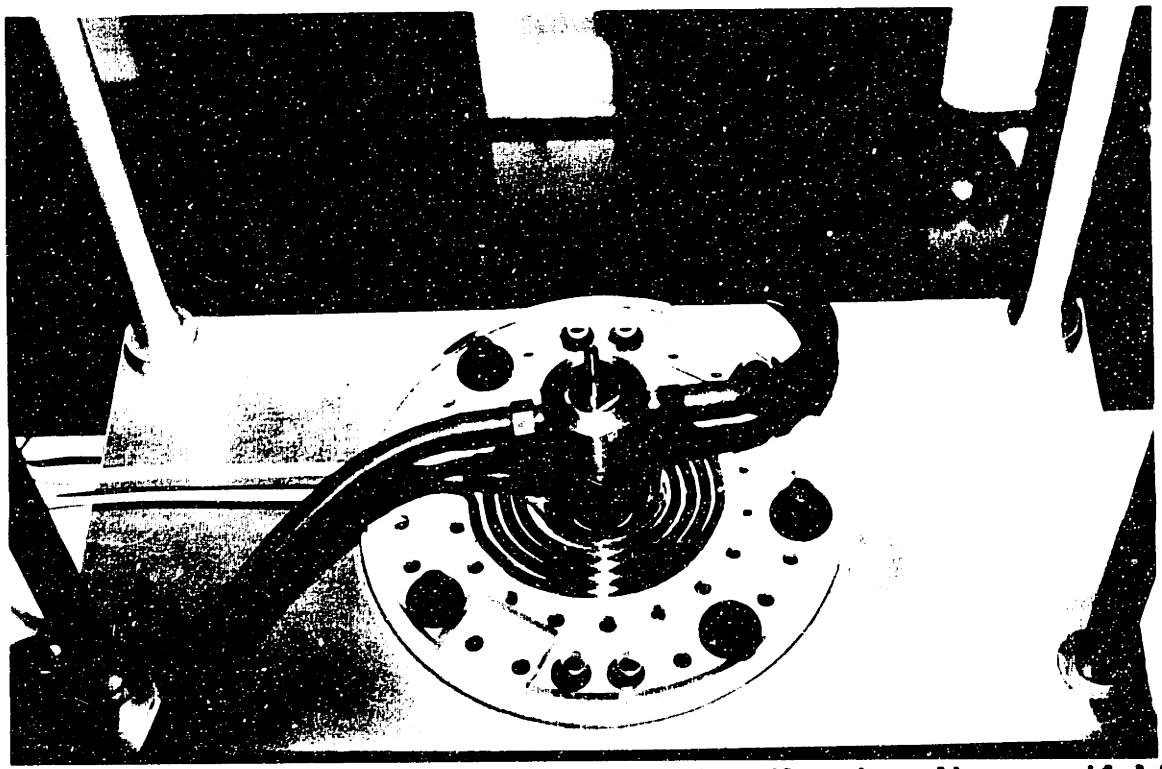

(b) Top view of apparatus showing spiral-coil and cooling manifold.

Fig. 4a,b Pictures of induction heating apparatus used to study thermal fatigue of coated monocrystals.

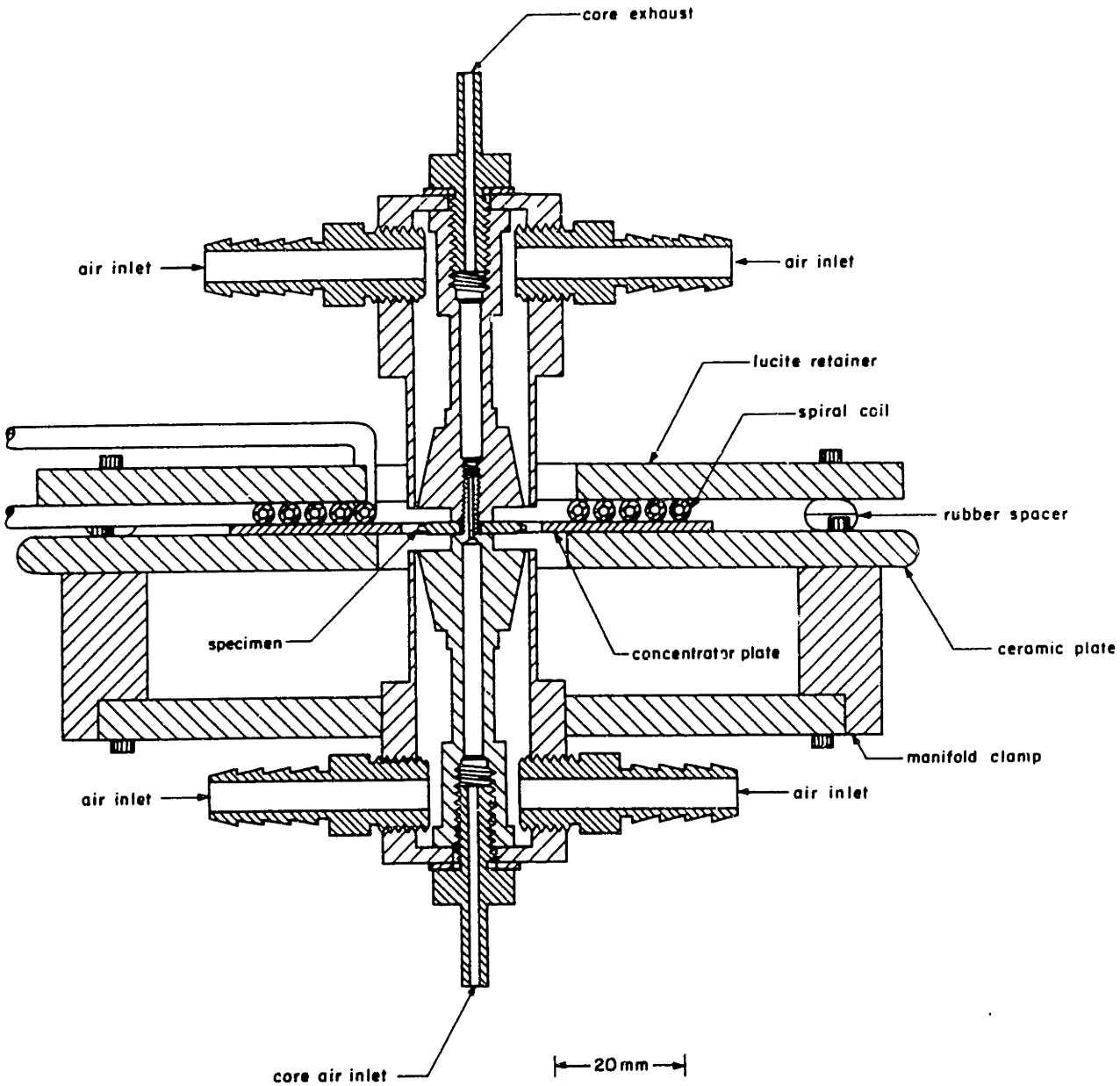

Fig. 5 Schematic of test apparatus for studying thermal fatigue in air.

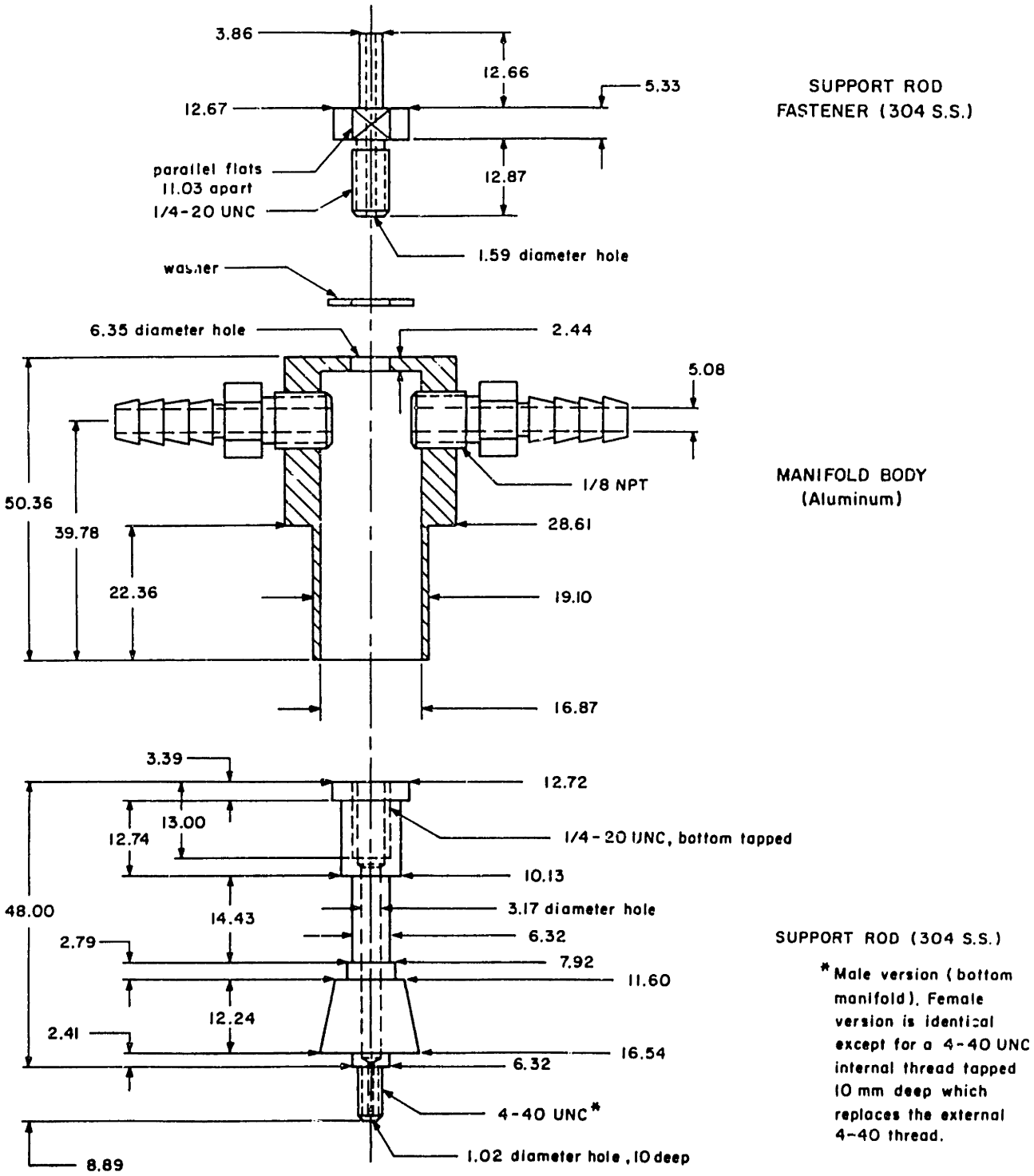

Fig. 6 Detail drawing of cooling manifold showing manifold body, specimen support rod, and support rod fastener. All dimensions in millimeters.

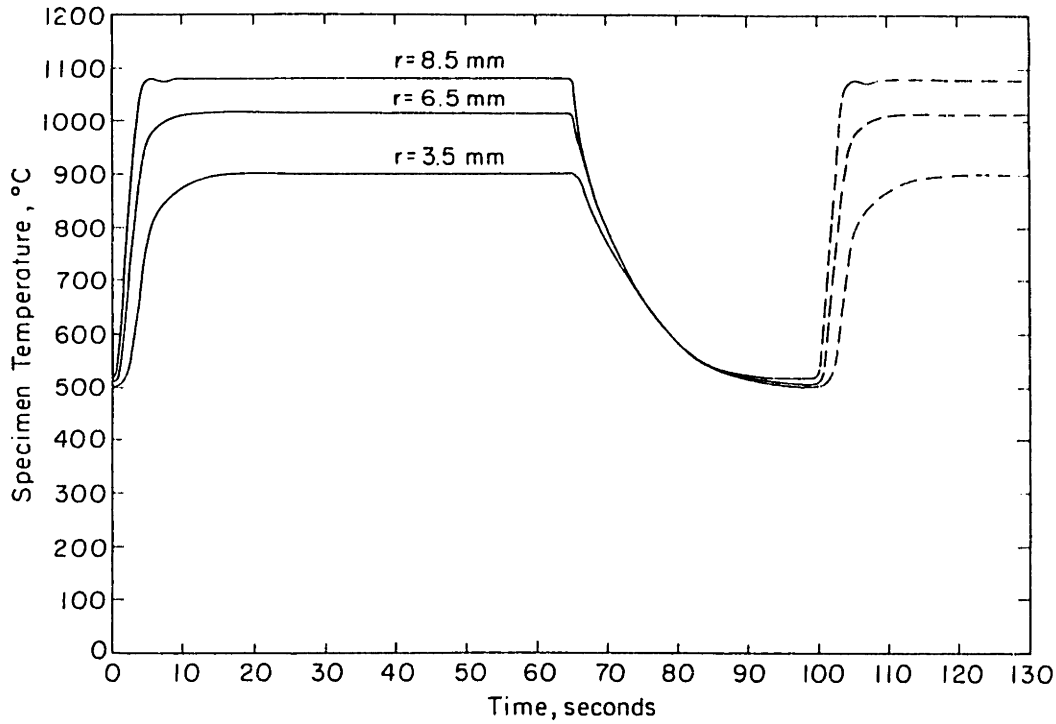

(a) Periphery heating from 520°C to 1080°C in 5s, followed by a 60s hold at 1080°C, followed by cooling to 520°C in 30s.

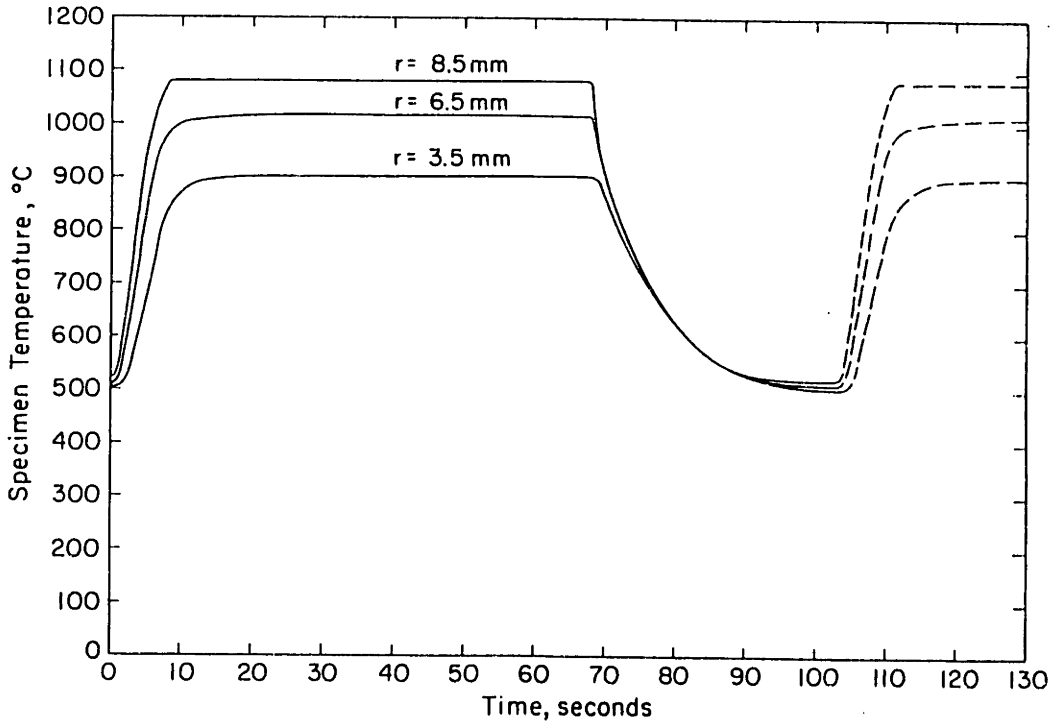

(b) Periphery heating from 520°C to 1080°C in 8s, followed by a 60s hold at 1080°C, followed by cooling to 520°C in 30s.

Fig. 7a,b Temperature history of stepped-disk specimens used in coating durability study (air environment).

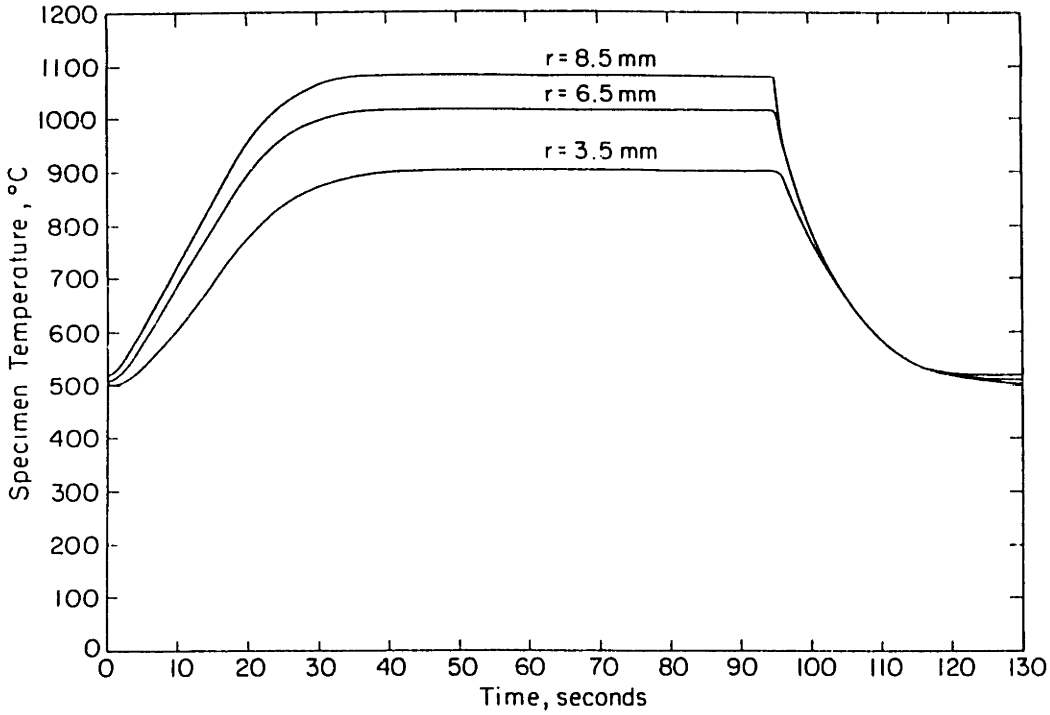

(c) Periphery heating from 520°C to 1080°C in 35s, followed by a 60s hold at 1080°C, followed by cooling to 520°C in 30s.

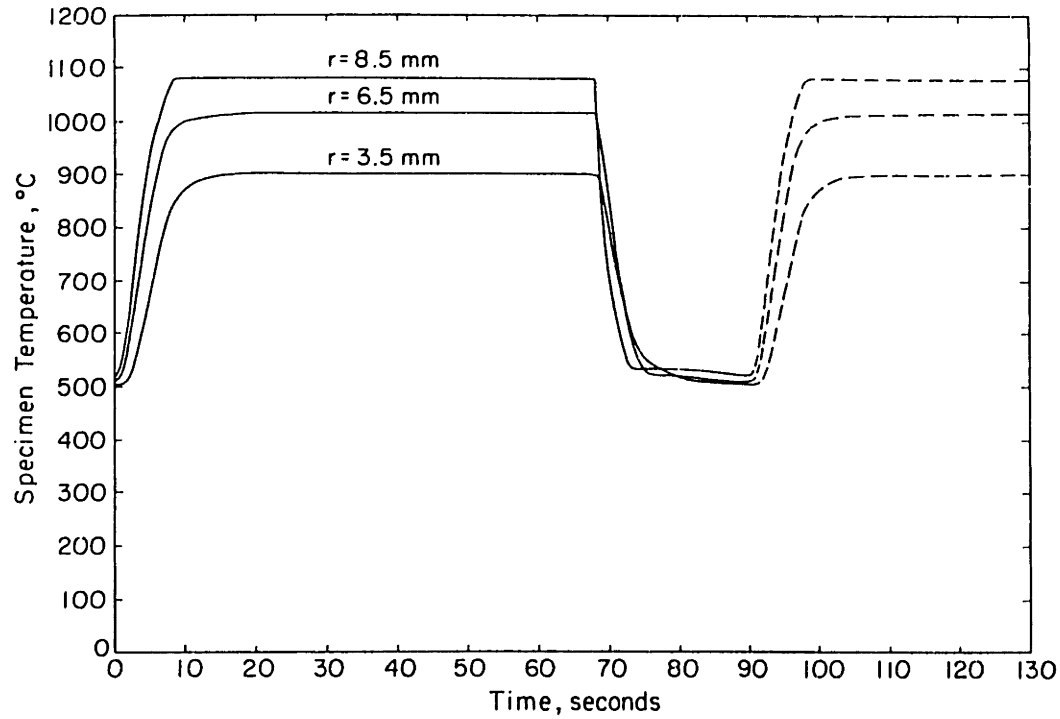

(d) Periphery heating from 520°C to 1080°C in 8s, followed by a 60s hold at 1080°C, followed by cooling to 520°C in 6s.

Fig. 7c,d Temperature history of stepped-disk specimens used in coating durability study (air environment).

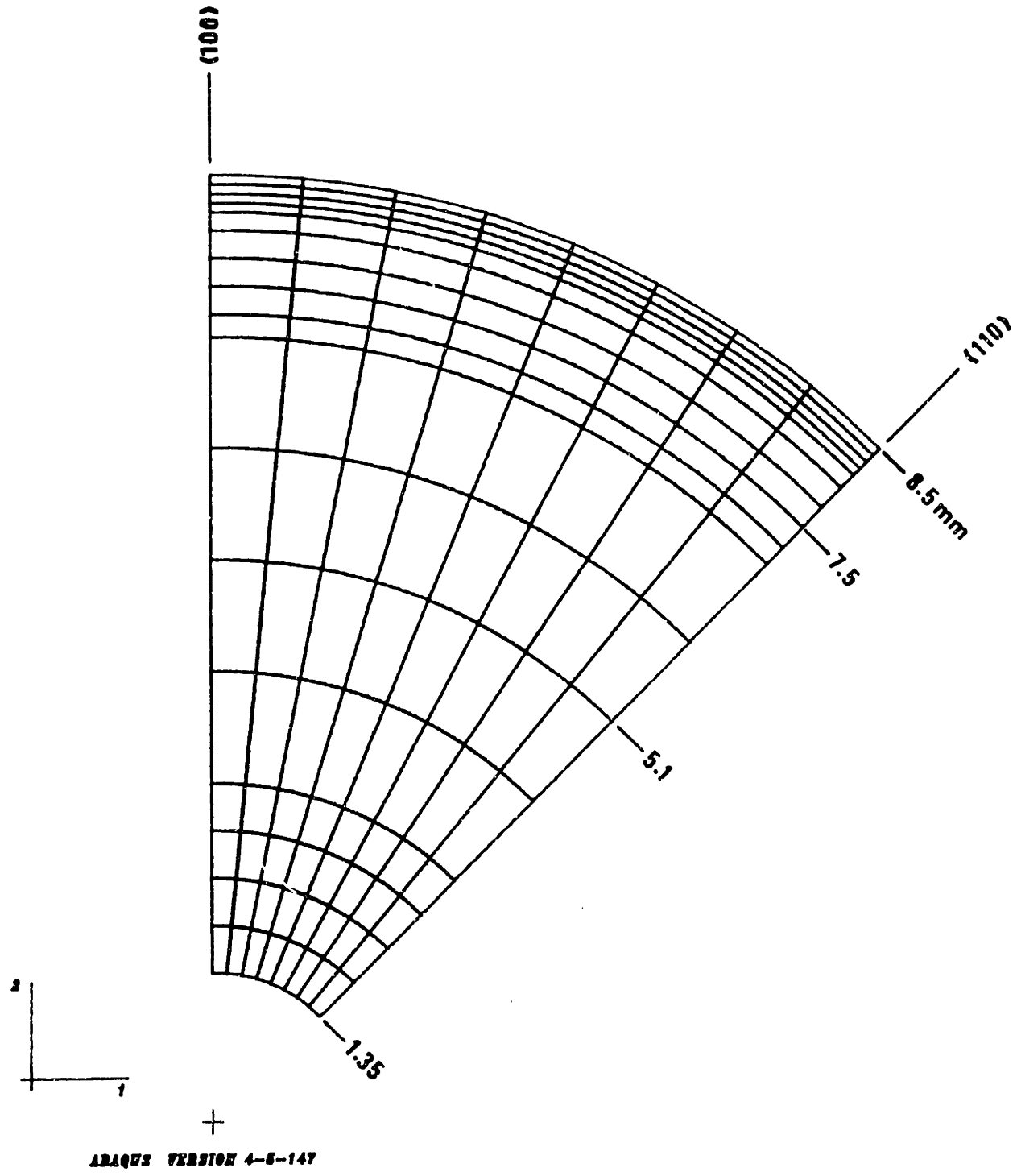

Fig. 8 Mesh used in anisotropic thermoelastic finite-element analysis of specimen stress-strain history.

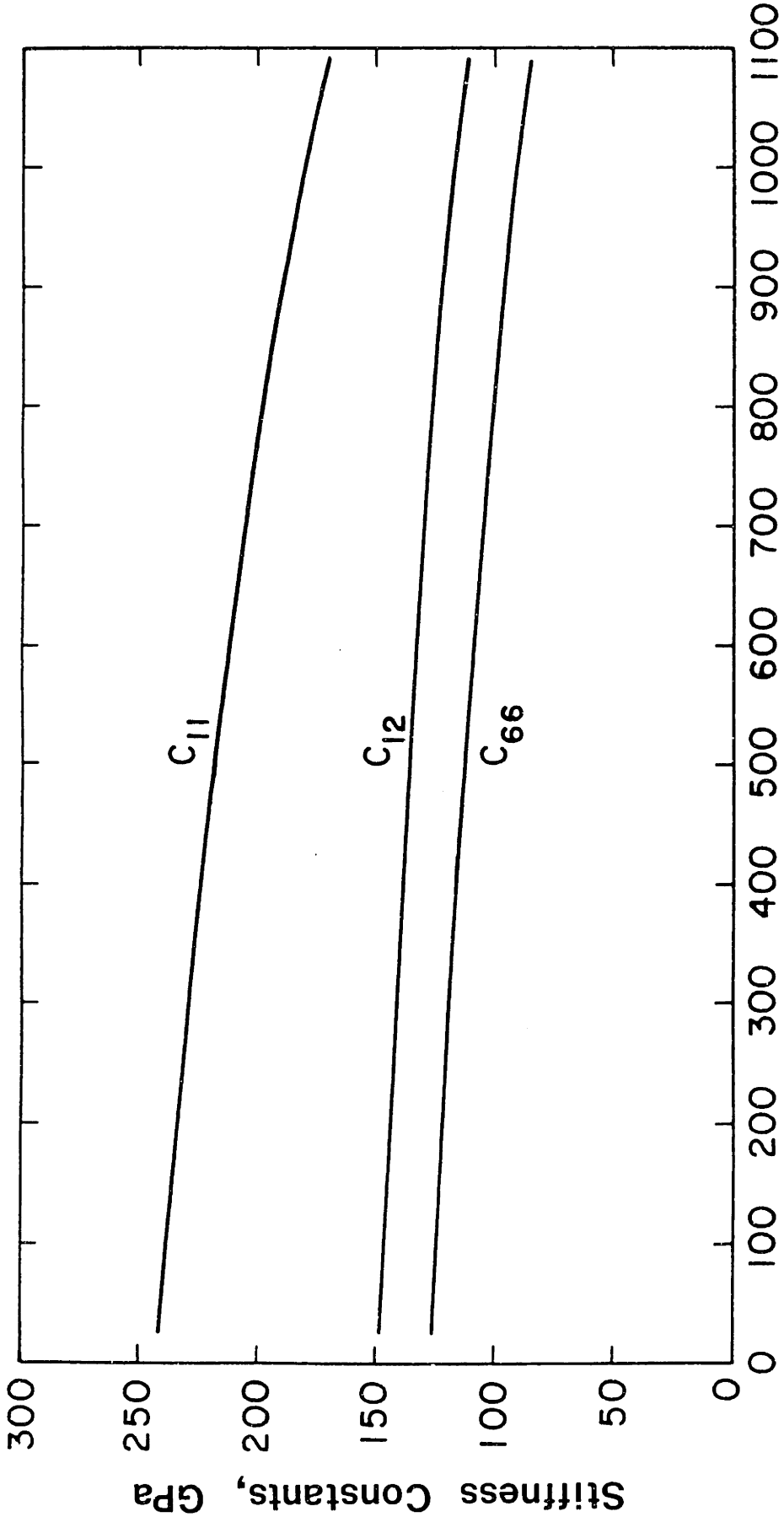

Fig. 9 Stiffness constants C_{ij} for Rene N4 as a function of temperature.

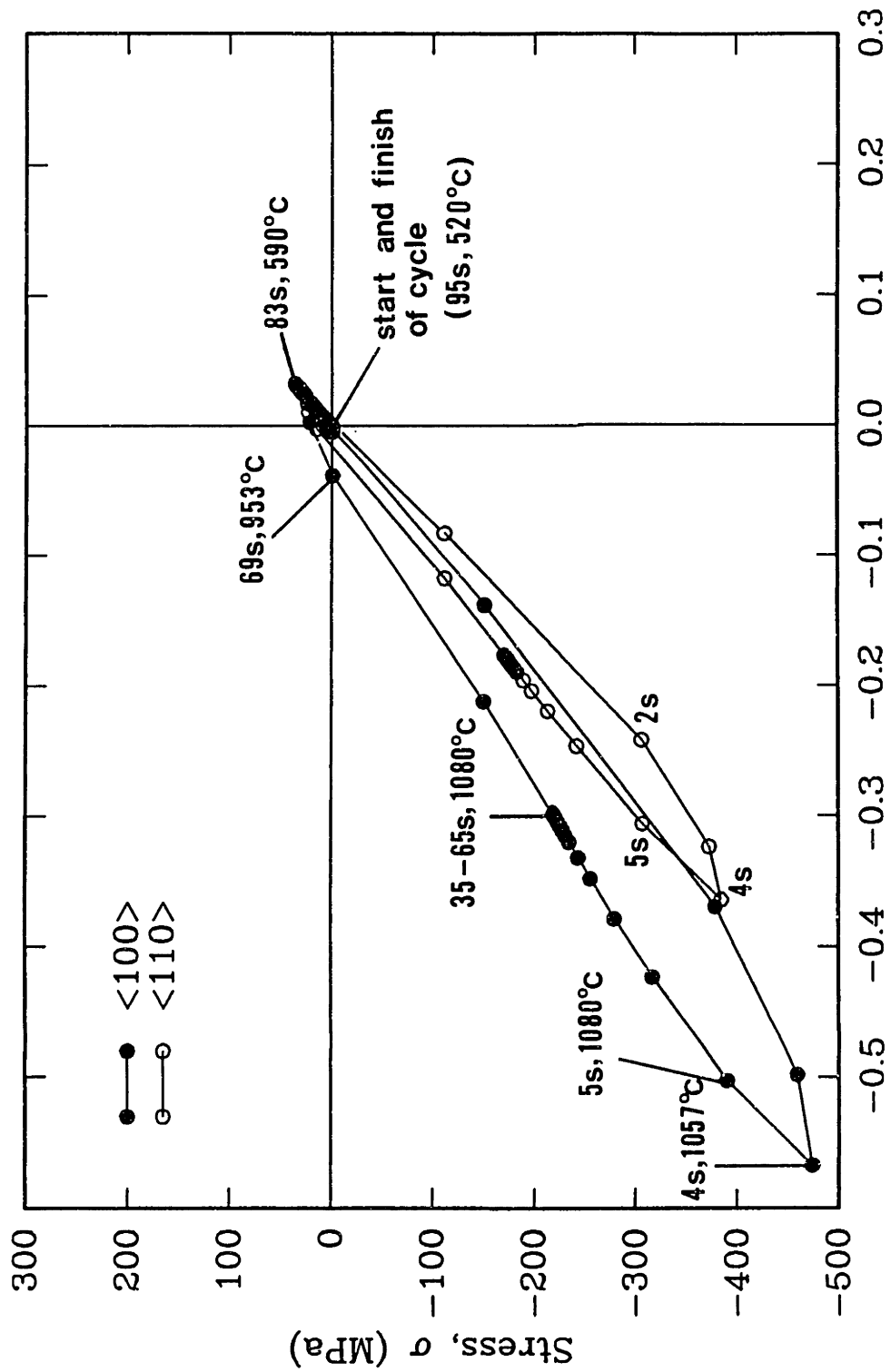

Fig. 10a Circumferential stress-strain history for the <100> and <110> directions of the specimen periphery, determined by a thermoelastic finite-element analysis for the 5s heating and 30s cooling of Fig. 7a.

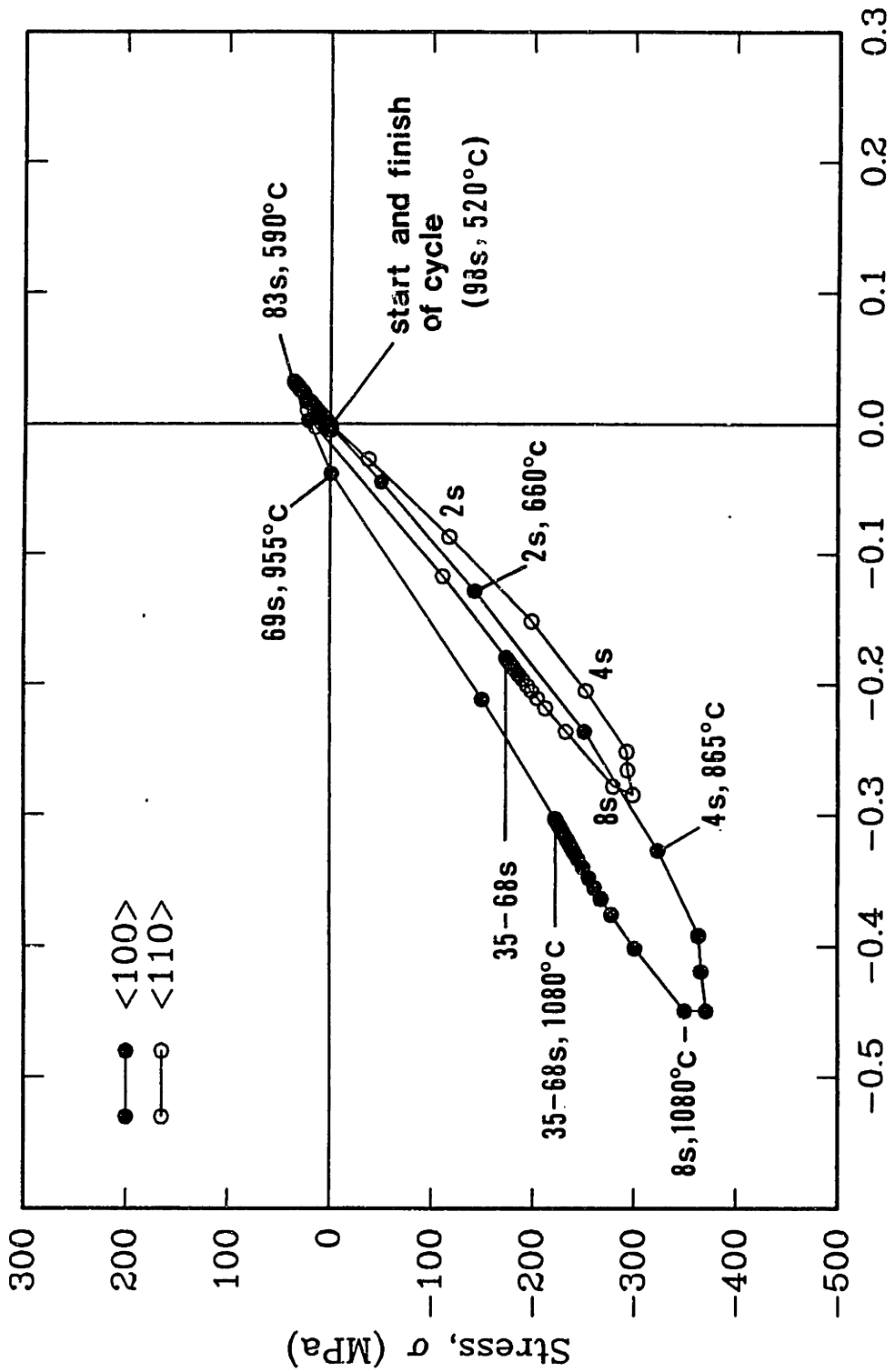

Fig. 10b Circumferential stress-strain history for the <100> and <110> directions of the specimen periphery, determined by a thermoelastic finite-element analysis for the 8s heating and 30s cooling of Fig. 7b.

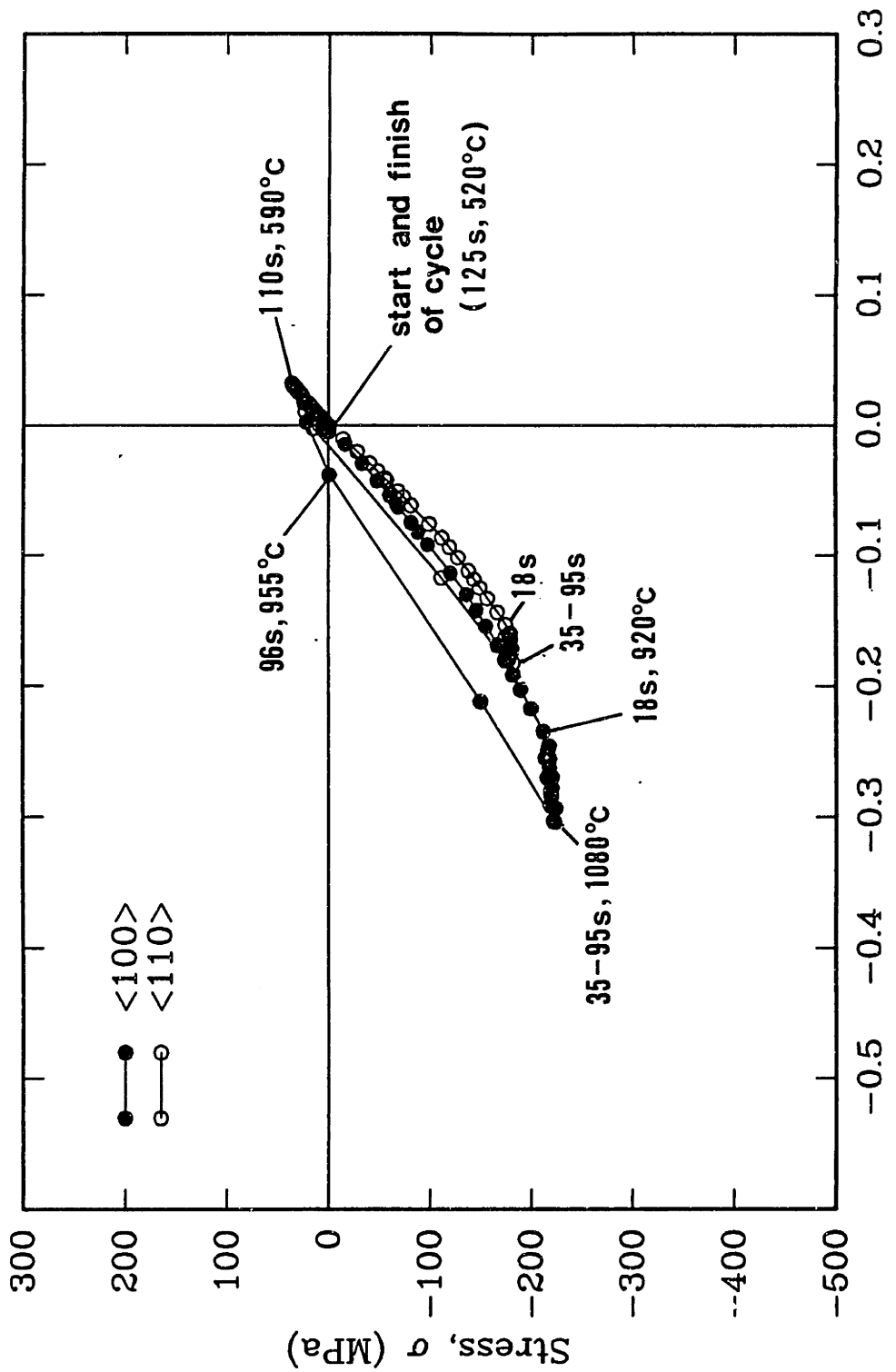

Fig. 10c Circumferential stress-strain history for the <100> and <110> directions of the specimen periphery, determined by a thermoelastic finite-element analysis for the 35s heating and 30s cooling of Fig. 7c.

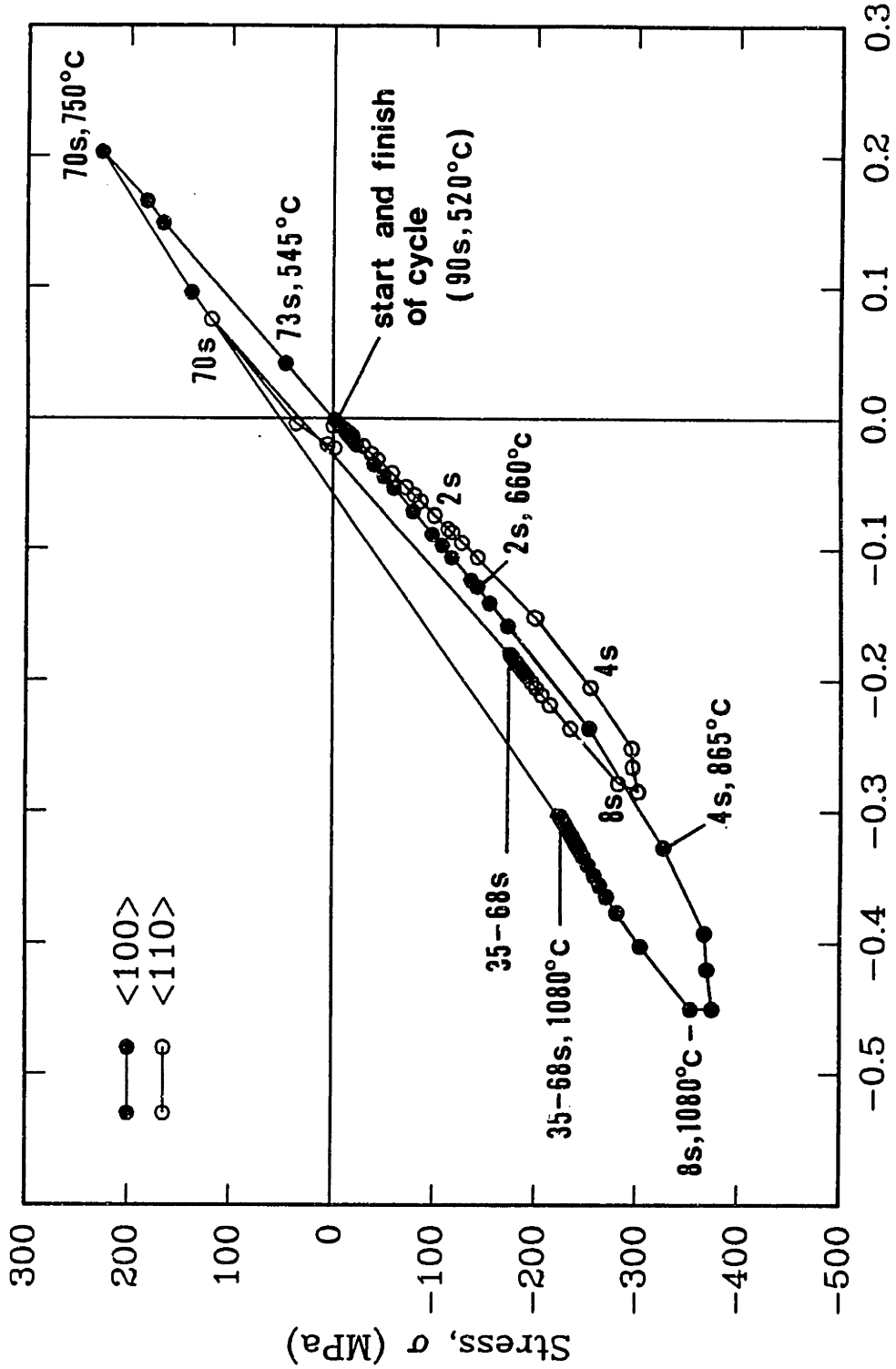

Fig. 10d Circumferential stress-strain history for the <100> and <110> directions of the specimen periphery, determined by a thermoelastic finite-element analysis for the 8s heating and 6s cooling of Fig. 7d.

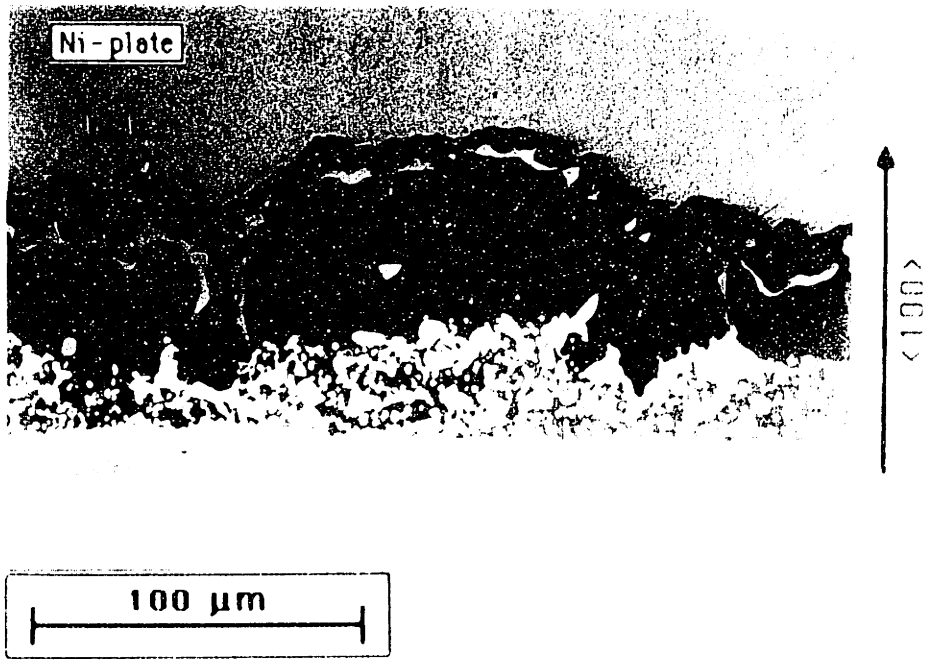

(a) <100> periphery direction (-0.56% < ε < 0.03%).

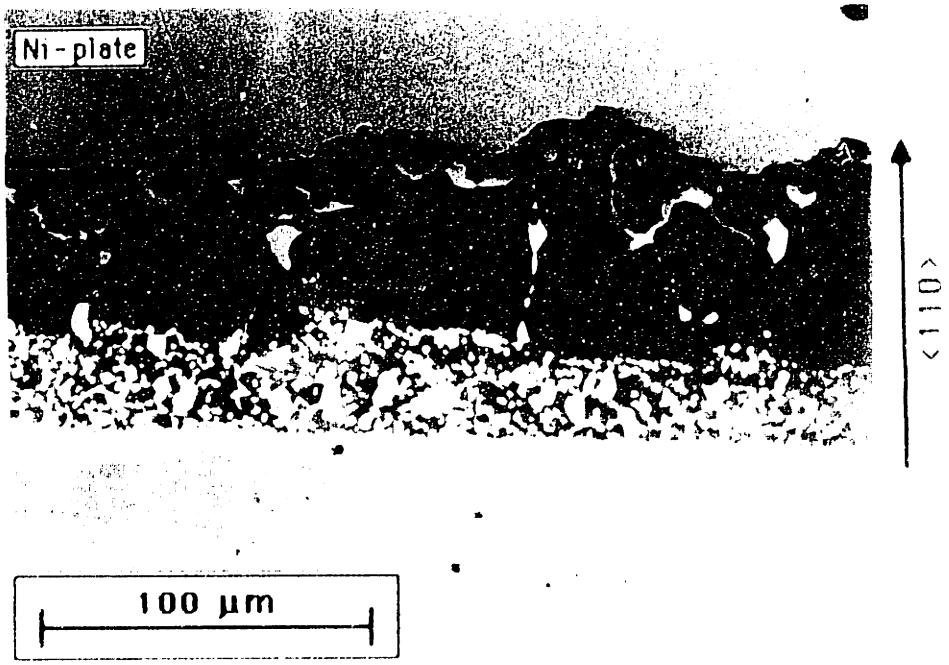

(b) <110> periphery direction (-0.36% < ε < 0.01%).

Figs. 11a,b Coating degradation along periphery after 6000 fatigue cycles. Periphery temperature history (Fig. 7a): 520 to 1080°C in 5s + 60s hold at 1080°C, followed by cooling to 520°C in 30s.

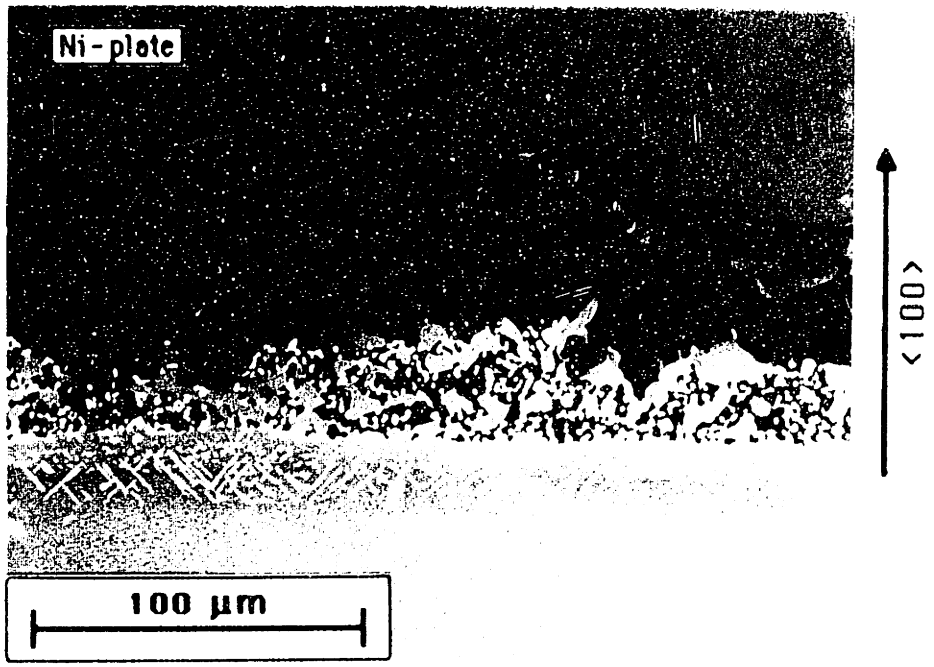

(a) <100> periphery direction (-0.56% < ϵ < 0.03%).

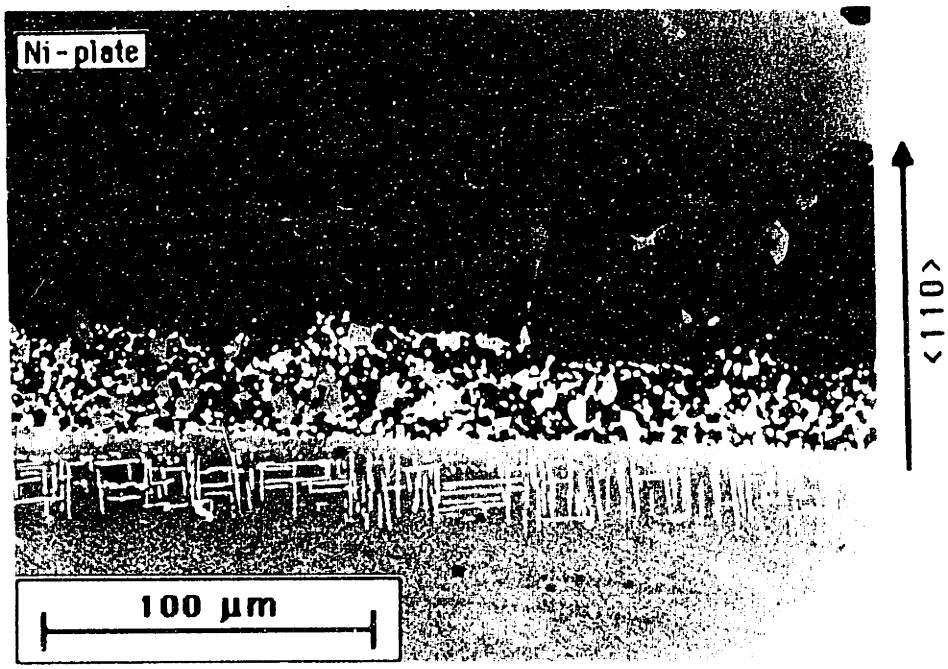

(b) <110> periphery direction (-0.36% < ϵ < 0.01%).

Figs. 11a,b Coating degradation along periphery after 6000 fatigue cycles. Periphery temperature history (Fig. 7a): 520 to 1080°C in 5s + 60s hold at 1080°C, followed by cooling to 520°C in 30s.

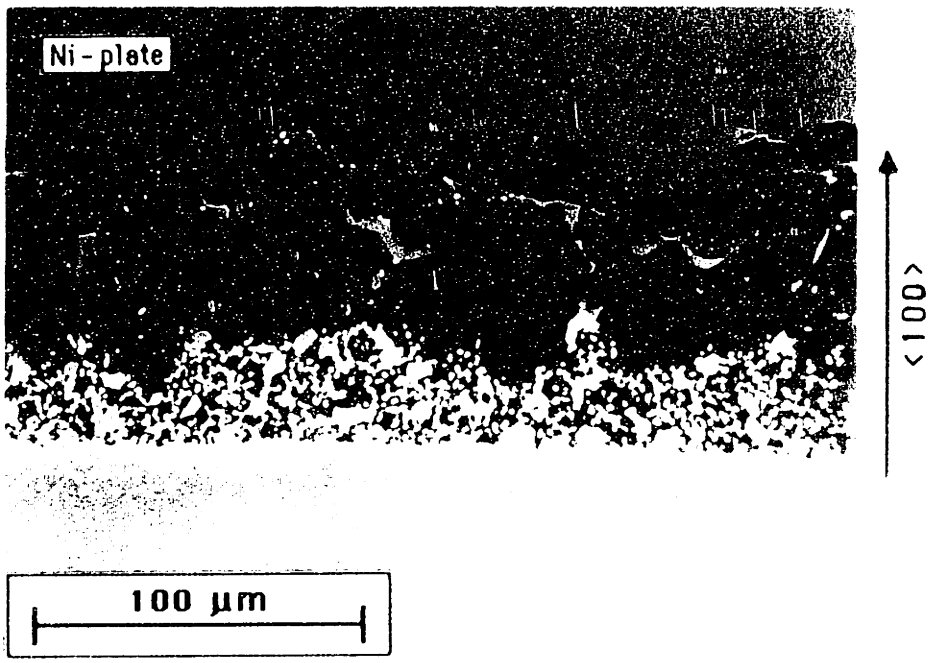

(c) <100> periphery direction (-0.45% < ϵ < 0.03%).

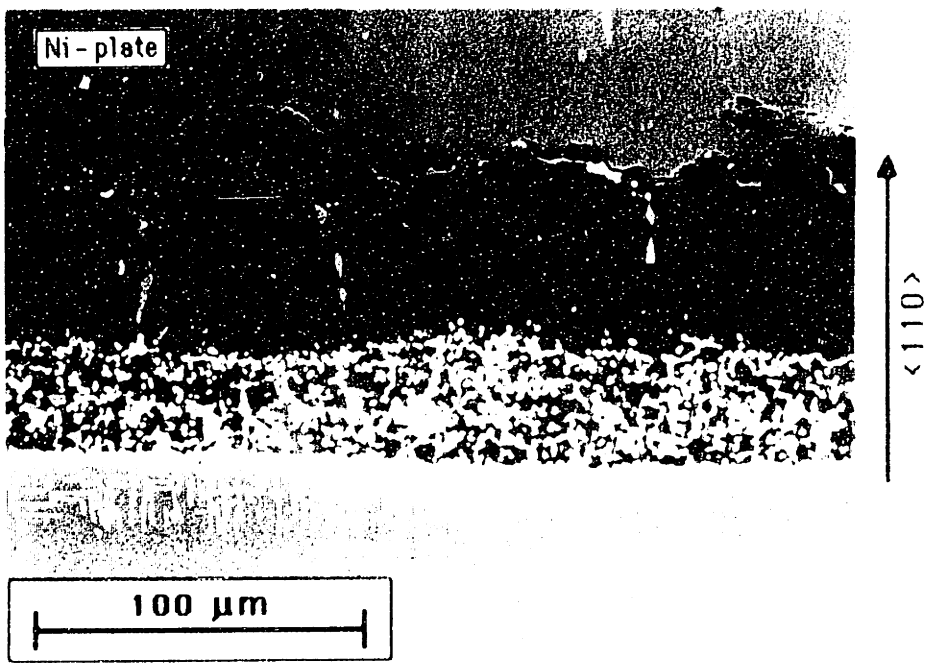

(d) <110> periphery direction (-0.29% < ϵ < 0.01%).

Figs. 11c,d Coating degradation along periphery after 6000 fatigue cycles. Periphery temperature history (Fig. 7b): 520 to 1080^{0}C in 8s + 60s hold at 1080^{0}C, followed by cooling to 520^{0}C in 30s.

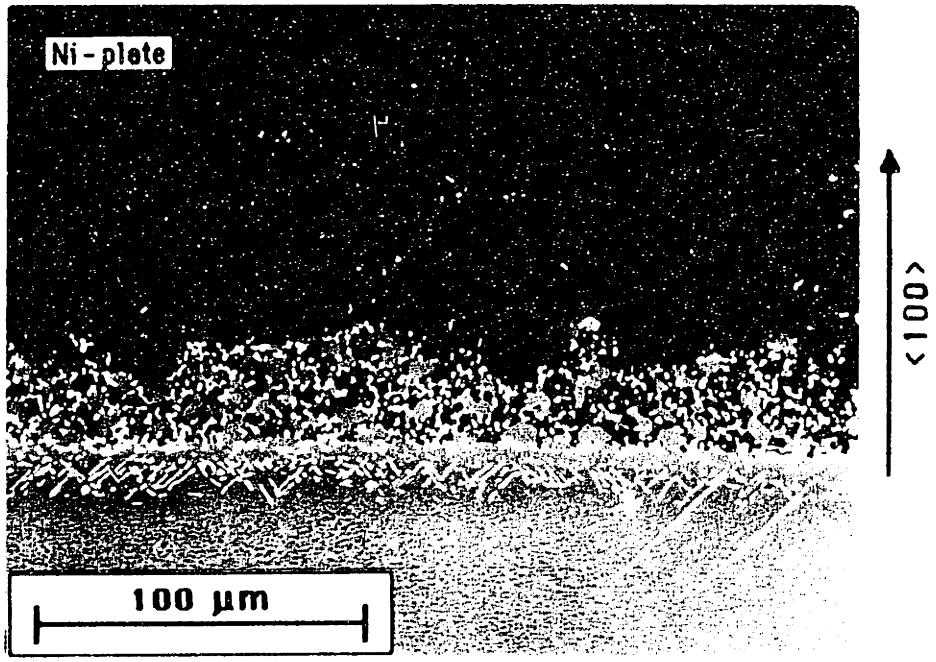

(c) <100> periphery direction (-0.45% < ε < 0.03%).

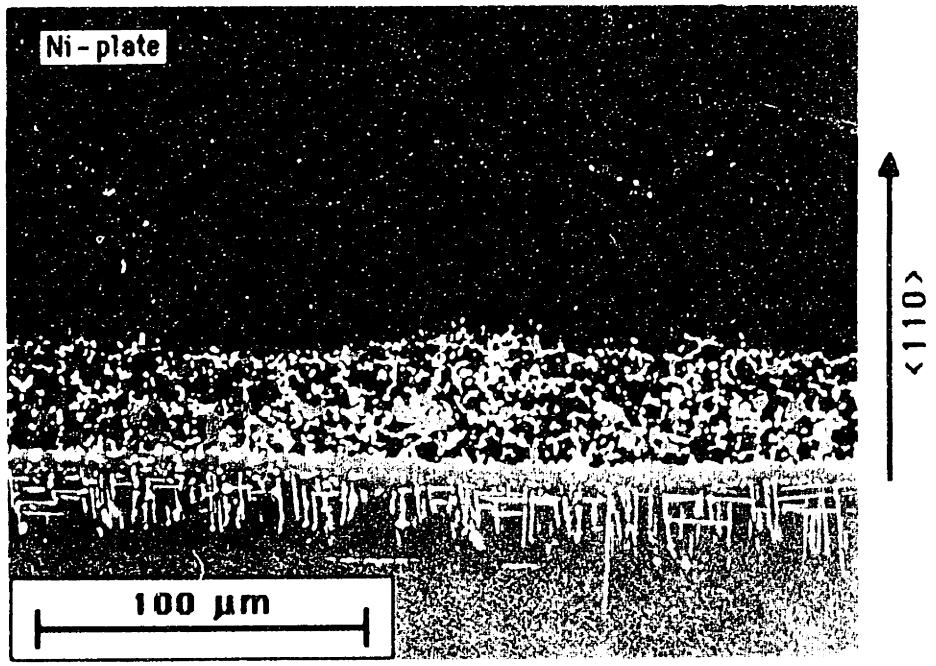

(d) <110> periphery direction (-0.29% < ε < 0.01%).

Figs. 11c,d Coating degradation along periphery after 6000 fatigue cycles. Periphery temperature history (Fig. 7b): 520 to 1080°C in 8s + 60s hold at 1080°C, followed by cooling to 520°C in 30s.

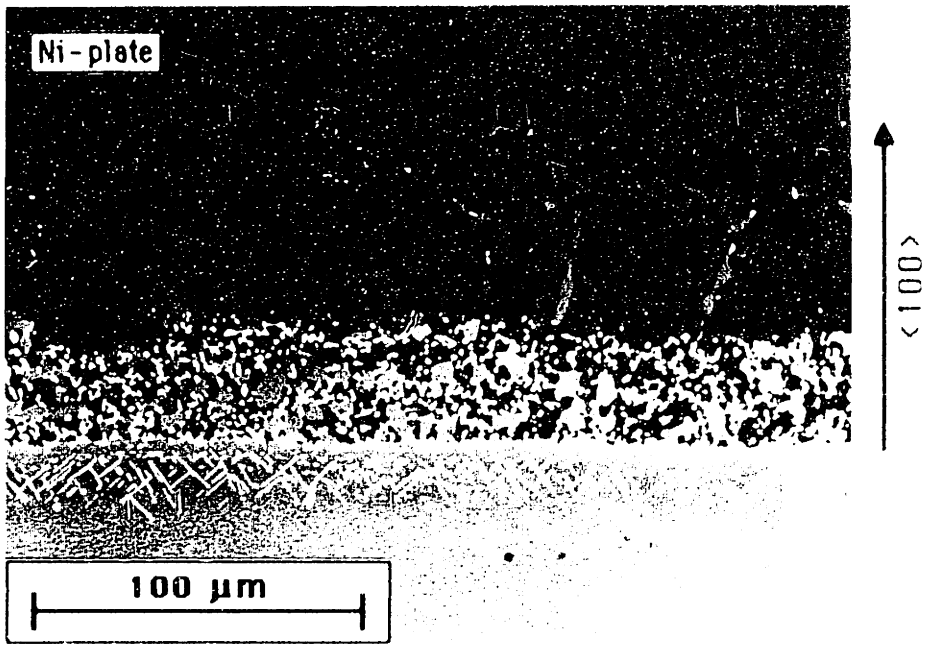

(e) <100> periphery direction (-0.30% < ϵ < 0.03%).

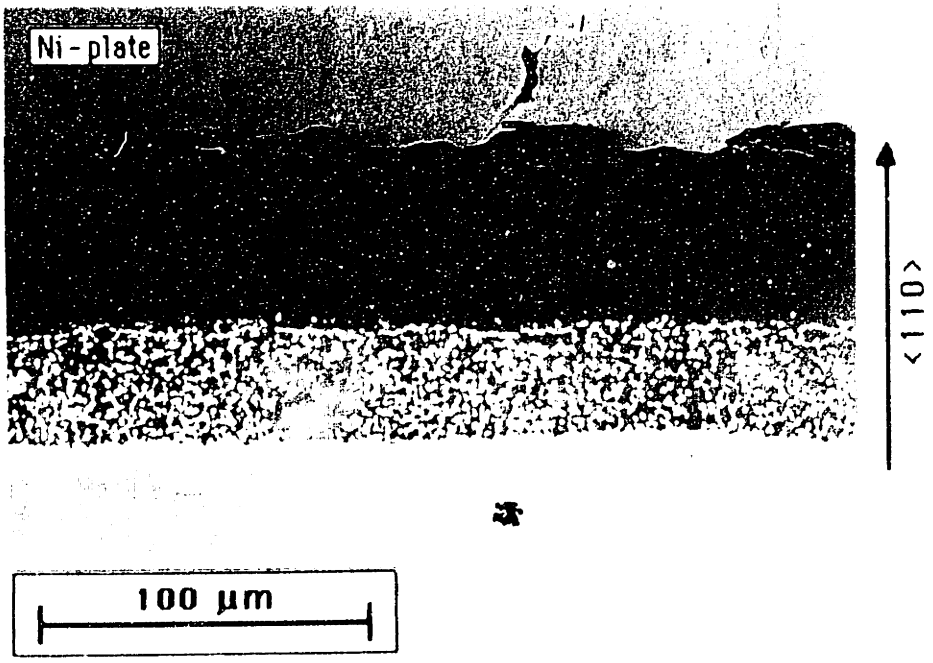

(f) <110> periphery direction (-0.20% < ϵ < 0.01%).

Figs. 11e,f Coating degradation along periphery after 6000 fatigue cycles. Periphery temperature history (Fig. 7c): 520 to 1080°C in 35s + 60s hold at 1080°C, followed by cooling to 520°C in 30s.

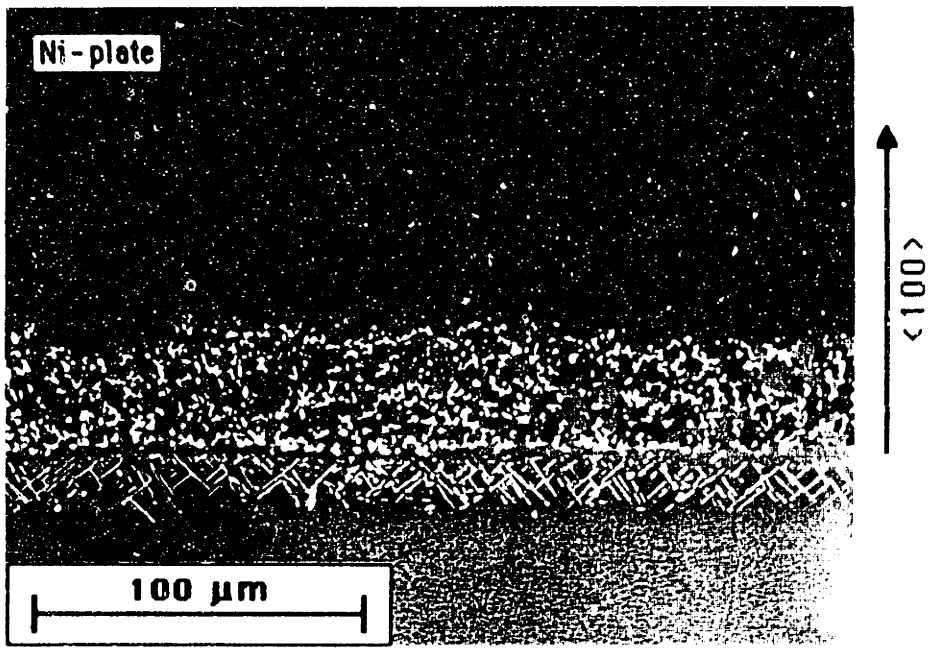

(e) <100> periphery direction (-0.30% < ϵ < 0.03%).

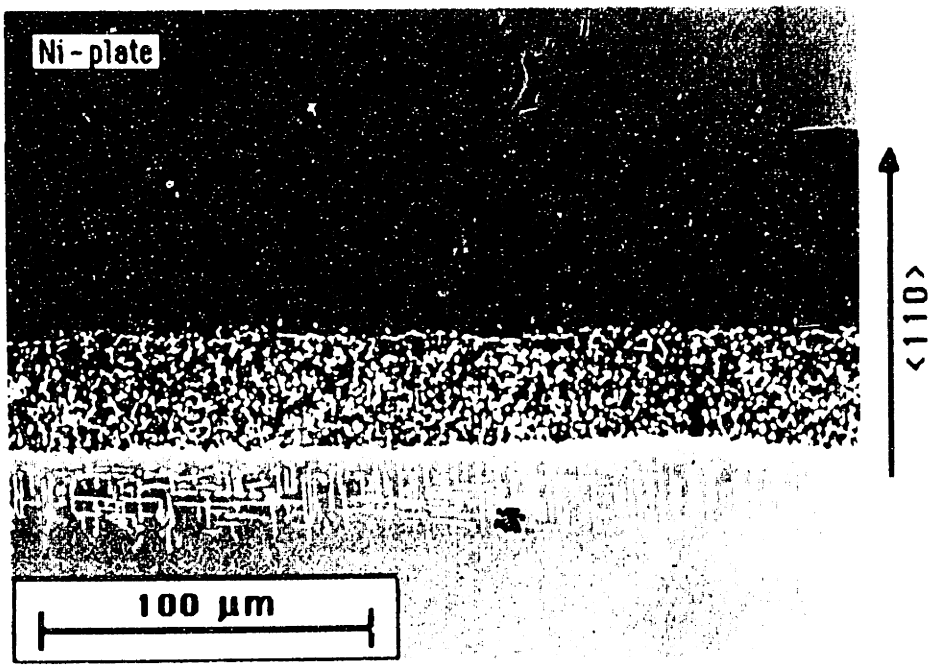

(f) <110> periphery direction (-0.20% < ϵ < 0.01%).

Figs. 11e,f Coating degradation along periphery after 6000 fatigue cycles. Periphery temperature history (Fig. 7c): 520 to 1080°C in 35s + 60s hold at 1080°C, followed by cooling to 520°C in 30s.

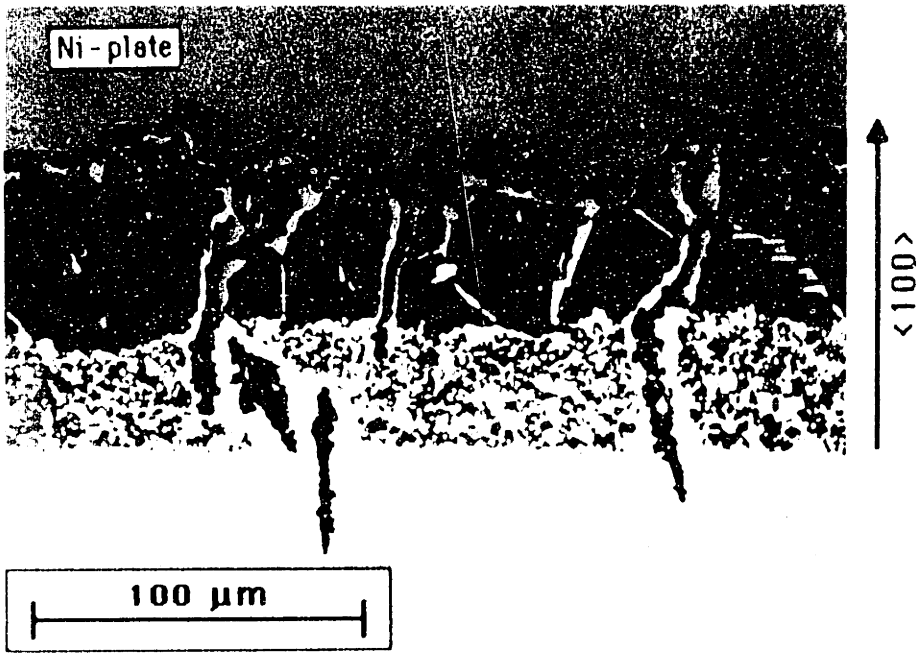

(g) <100> periphery direction (-0.45% < ε < 0.20%).

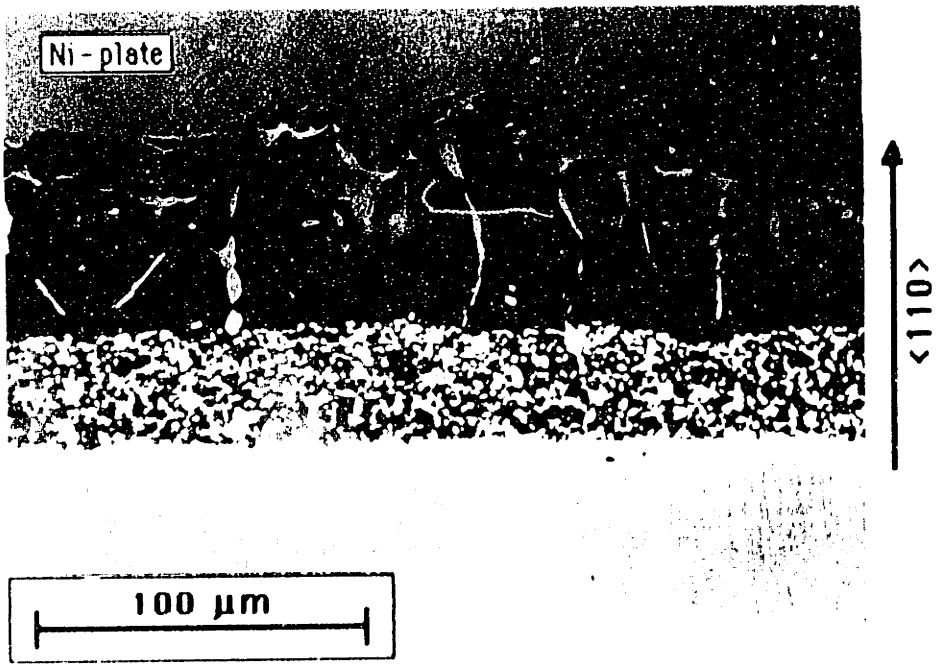

(h) <110> periphery direction (-0.29% < ε < 0.08%).

Figs. 11g,h Coating degradation along periphery after 6000 fatigue cycles. Periphery temperature history (Fig. 7d): 520 to 1080°C in 8s + 60s hold at 1080°C, followed by cooling to 520°C in 6s.

Chapter 3

The Chemical and Mechanical Processes of Thermal Fatigue Degradation of an Aluminide Coating

Abstract

The effect of strain history on the degradation of an aluminide coating applied to a monocrystalline nickel-base superalloy is examined by induction heating of anisotropic stepped-disk specimens, which allow the simultaneous study of several crystallographic orientations and corresponding strain histories typical of service.

Depending on substrate strain history, two modes of coating degradation were observed: surface scalloping and through-thickness cracking. Tolerable coating scalloping (<10% of total coating thickness) was observed for 6000 cycles between strains of -0.45% at 1080^{0}C and 0.01% at 590^{0}C. Degradation by through-thickness coating cracking was observed for 6000 cycles between strains of -0.45% at 1080^{0}C and 0.20% at 750^{0}C.

The depth of coating scalloping correlates well with peak compressive substrate strain. Based on this correlation, a mechanism for scallop initiation and growth involving cyclic oxide cracking and creep is discussed.

Coating cracking appears to be the result of tensile coating strains applied below the transition temperature of the aluminide coating.

Introduction

In many instances the useful life of a gas-turbine airfoil is determined by the life of the protective coating. Aluminide coatings are typically degraded by the combined effects of oxidation, hot-corrosion, and thermal fatigue. As noted in Chapter 1, for airfoil temperatures in excess of approximately 1000^{0}C, oxidation is the dominant mechanism of coating degradation. For airfoil temperatures below 950^{0}C, which is typical of the leading and trailing edges of second and third stage airfoils, hot-corrosion attack is typically the dominant mode of coating degradation (this mode of coating degradation is discussed in Chapter 4).

Recent isothermal and cyclic oxidation and corrosion studies pertaining to aluminide coating degradation [18,20] have not addressed the important effect of strain history on coating degradation.

In this chapter the effect of substrate strain history on aluminide coating degradation is examined. The degradation observed is correlated with the temperature and strain history of the test specimens.

Experimental Procedure

Specimen geometry, substrate composition and aluminide coating. As discussed in Chapter 2, 17mm diameter stepped-disk specimens were machined from a monocrystal rod of Rene N4, such that their faces were normal to the [001] crystal growth direction (see Fig. 3). The composition of the monocrystalline Rene N4 substrate and details of the specimen heat treatment and aluminization process are given in Chapter 2.

Test apparatus. As described in detail in Chapter 2, induction heating of stepped-disk specimens (Fig. 3) was used to produce cyclic thermal strains in the aluminide coated Rene N4 specimens.

Isothermal oxidation test. To determine the effect of isothermal exposure on aluminide coating degradation and to provide a reference to compare with the coating degradation obtained as a result of cyclic thermal strains, a specimen was isothermally oxidized in air for 120 hr at 1080^{0}C. The 120 hours represents the sum of the 6000 hold times of 60 s each used in the cyclic oxidation tests, plus a time-weighted average to account for the effect of slow cooling in the cyclic tests.

Cyclic oxidation tests. To determine the effect of strain history on coating oxidation and cracking, the temperature histories of Figs. 7a-d were selected. The corresponding

substrate strain histories (Figs. 10a-d) were determined in Chapter 2 by a thermoelastic finite element analysis.

Microprobe analysis and backscattered electron micrographs. Distributions of the major coating elements (Al, Cr, Co, Ni, Mo, Ta, Ti, and W) present in the as-coated and thermally exposed specimens were determined with a JOEL Model 7320 electron microprobe. A wavelength scan indicated that the concentration of the minor substrate elements Cu, Fe, Hf, and Nb in the coating were below detectable limits (about 0.1 at%). For the quantitative analyses the incident electron beam was operated at an accelerating potential of 15 kV and a current of 20.00 nA. The beam diameter at the specimen surface was 0.8 μm with a positioning accuracy of better than 5 nm. For an accelerating potential of 15 kV, the depth of penetration of X-rays, which is dependent upon the density of the phase analyzed, is less than 2 μm for the Ni and refractory-rich phases analyzed in this study. To help preclude changes in beam current caused by mechanical effects, all specimens and standards were mounted simultaneously in the microprobe vacuum chamber prior to standardization and analysis; this prevents straining of the filament due to changes in pressure encountered with installation and removal of samples. For all analyses performed in this study beam-current drift was less than 0.03 nA. To prevent erroneous analyses, each specimen was carefully focused at a magnification of 20,000X. The quantitative analyses involved measurement of

the X-ray intensities in the Kα lines of the coating elements and comparing them with the X-ray intensities from pure elemental standards. Composition was obtained using a ZAF (atomic number adsorption and florescence) correction program.

For the backscattered electron micrographs used in this Chapter (Figs. 12-15) the optimal accelerating voltage for obtaining good contrast between coating phases was found to be 25 kV. Note that the various shades of gray in backscattered electron micrographs are due to differences in average atomic number. The lighter the shade, the higher the average atomic number of elements in that region.

Results and Discussion

As-coated specimen

Background. The driving force for aluminization is the difference between the activity of the source aluminum in the pack and activity of the aluminum at the substrate surface. Marker studies, performed by Janssen and Rieck [32] on Ni-Al couples, show that for a low activity of source Al, the coating forms by predominant ***outward*** diffusion of Ni from the substrate through the growing NiAl layer; substrate elements other than Ni essentially remain stationary in the substrate during coating formation. This outward diffusion of Ni during coating formation in low-activity packs has also been verified by Goward et al [30,33] for the aluminides formed on nickel-base

superalloys. The outward diffusion of Ni results in a two-zone coating (see Fig. 1); an outer zone which forms **above** the original substrate surface and an inner zone which forms in a narrow region **below** the substrate surface. The inner coating zone can be identified by its high density of micron-size refractory rich precipitates, which form as a result of the high concentration of Cr, W, and Mo in the inner coating zone and their low solubility in β(NiAl).

Coating morphology. The coating thickness along the entire specimen periphery was within 70±4μm. Any variation in coating thickness was gradual, and amounted to no more than a 4μm variation over an arc of approximately 30^0.

Results of microprobe analysis. Due to the sub-micron phase separation present in the outer-zone matrix it was necessary to increase the beam diameter from the 0.8 μm, used in other analyses, to 2μm. Thus, the values obtained represent the nominal composition of the outer-zone. For analysis of the inner-zone matrix and precipitates the beam diameter was reduced to 0.8 μm. The quantitative microprobe analyses performed along <100> and <110> peripheries showed that within the resolution of the microprobe (better than 0.5 at% for all elements analyzed) no variation in coating composition (matrix and precipitates) was observed between these two substrate orientations. A high magnification backscattered-electron

micrograph showing typical coating structure is given in Fig. 12 along with results of a microprobe analysis for coating composition along this typical <100> periphery direction.

In Fig. 12 the outer and inner coating zones are clearly visible. As shown on the Ni-Cr-Al ternary phase diagram of Fig. 16, the outer zone is near-stoichiometric β (see Point 2)[10]. Note that the coating formation temperature was 1050°C; however, little difference exists between the extent of the β-phase field at 1050 and 1080°C. The sub-micron phases present in this zone were too small to be analyzed by the microprobe, but have been identified in previous studies as α(Cr,Mo) precipitates [33,34].

The removal of Ni from the subsurface region of the substrate during coating formation has resulted in the transformation of this region from $\gamma + \gamma'$ to a near-stoichiometric β(NiAl) (see Points 1 and 2 on the ternary of Fig. 16). The high density of

---

[10]When plotting coating composition on the Ni-Cr-Al phase diagram it is assumed that Co substitutes for Ni, with Ti, Ta and Mo substituting for Al. This is consistent with phase extraction studies of superalloys [35,36,37]. Further justification for including Co with Ni is provided by the observation that (1) the Co-Cr-Al phase diagram is similar to the Ni-Cr-Al diagram, (2) Co has an atomic radius only 1% larger than Ni and (3) the diffusion of Al and Cr is approximately the same in cobalt and in nickel. It should be noted however that Co is known to reduce the solubility of Al and Ti in γ [38]. This decreased solubility would shift the $\gamma + \gamma'$ phase boundaries of the Ni-Cr-Al ternary towards the Ni corner.

elongated refractory-rich precipitates in the inner zone (labeled "1" in the micrograph of Fig. 12) are refractory rich (W, Cr, Mo) precipitates which, as mentioned above, form as a result of the low solubility (<4 wt%) of W and Cr in near-stoichiometric β at the coating formation temperature of 1050°C.

To summarize, the pack-aluminizing process and post-aluminizing heat treatment forms a coating based on near-stoichiometric β(NiAl). The coating is comprised of an outer zone which contains a sub-micron dispersion of precipitates (probably Cr, Mo rich) and an inner zone containing a dense dispersion of refractory rich Cr and W precipitates.

Isothermal oxidation.

Coating morphology. 120 hours at 1080°C has increased the total coating thickness along the specimen periphery from 70 μm to 90±5μm. Changes in coating thickness along the periphery were gradual, with no scalloping or localized oxidation of the coating observed. Comparison of Figs. 12 and 13 shows that the thickness of the outer-zone matrix has increased by approximately 13% (from 48 to 55μm) after isothermal exposure, with the thickness of the inner-zone matrix increasing by approximately 38% (from 22 to 35μm).

Results of microprobe analysis. Microprobe analyses performed along <100> and <110> periphery directions showed

essentially no variation in coating composition (matrix and precipitates) between these two substrate orientations. The results of a typical analysis for a <100> orientation is presented in Fig. 13. The lack of gradient in element concentration observed in the coating matrix indicates that diffusion and equilibrium partitioning of elements between the two coating zones occurs within 120 hr at 1080°C.

Isothermal exposure has increased the nickel equivalent (Ni + Co) in the outer coating zone from an average of 49 at% to 55.4 at%. The Al-equivalent (Al+Ti+Ta+Mo) has decreased from an average of 49 at% to 39 at%. The Cr content has increased from 3 to 6 at%. The Ni-Cr-Al phase diagram of Fig. 16 shows that this changes the bulk coating composition in the outer-zone from near stoichiometric β, as coated, to a composition that is close to the $\beta/(\beta+\gamma)$ phase boundary (see Points 2 and 3, Fig. 16). In the outer coating zone, the sub-micron phase which was present in the as-coated condition dissipated, due to the increased solubility of α(Cr,Mo) with increasing Ni content (see Fig. 16 and the Ni-Cr-Mo ternary of [38]). In the inner coating zone, the refractory-rich (W, Cr) precipitates present in the as-coated condition have coarsened and agglomerated (analysis pt. "2", Fig. 13). Extending from the coating/substrate interface are fine refractory-rich (W, Cr, Mo) needles, aligned with <110> substrate directions (analysis pt. "3", Fig. 13). These σ-phase needles form as a result of the continued diffusion of Ni from the

substrate into the coating, which decreases the Ni content, and hence solubility of W, Cr, and Mo in the sub-coating zone [39].

Coating oxidation. As a consequence of the 120 hr isothermal exposure an oxide approximately 2.5 μm thick has developed along the coating surface (black band in backscattered electron micrograph of Fig. 13). SEM examination of the oxide showed it to be continuous with only minor cracking observed along 100 and 110 substrate orientations: <100> oxide crack-opening < 1 μm (crack length < 28 μm), <110> oxide crack-opening < 0.5 μm (crack length < 15 μm). A quantitative microprobe analysis showed the oxide to be stoichiometric Al_2O_3.

Pettit [40] gives the parabolic rate constant for oxidation of Ni-25 wt %Al at 1080°C as $k_p = 5\times10^{-13}$ g^2/cm^4-s (see Fig. 17). Based on this data, the oxide thickness after 120 hours at 1080°C should be 2.48μm[11]; in excellent agreement with the average

---

[11]The increase in weight due to oxidation (Δm g O^{2-}/cm^2) is related to the parabolic rate constant k_p and time t by $(\Delta m)^2 = k_p \times t$. Thus, for $k_p = 5\times10^{-13}$ g^2/cm^4-s and t = 432,000 s (120 hr), $\Delta m = 4.65\times10^{-4}$ g O^{2-}/cm^2. For $\rho_{Al_2O_3} = 3.97$ g/cm^3 the oxide thickness h_{ox} is:

$$h_{ox} = \frac{\Delta m \text{ g } O^{2-}}{\text{cm}^2} \left| \frac{102 \text{ g } Al_2O_3}{48 \text{ g } O^{2-}} \right| \frac{\text{cm}^3}{3.97 \text{ g } Al_2O_3} = 2.46\times10^{-4} \text{ cm}$$

2.5μm thick oxide observed (Fig. 13).

To summarize, isothermal exposure for 120 hours at 1080°C results in a 20% increase in coating thickness, to approximately 90 μm. The bulk aluminum concentration drops from 48 at% as-coated to approximately 34 at% after isothermal exposure (Al equiv. decreases from 49 to 39 at%). Coarsening and agglomeration of the refractory-rich precipitates present in the as-coated condition occurs, along with precipitation of σ-phase needles in the subcoating zone.

Thermal cycling and oxidation.

Coating morphology. The nominal coating thickness of all specimens after thermal cycling was roughly 90 μm, which was the same as obtained with isothermal oxidation. The increase in nominal thickness of the inner and outer coating zones was also similar to that obtained with isothermal oxidation.

The low magnification micrographs of Figs. 11a-g and the high magnification companion micrographs of Figs. 15a-h indicate that there are two distinct types of coating degradation: scalloping, which occurs for the rapid heating and slow cooling rates of Figs. 7a,b,c, and cracking, which occurs along the high strain <100> directions for the rapid cooling rate of Fig. 7d. Both of these modes of coating degradation are typically observed in service [41,42]. After a brief discussion of the quantitative microprobe

analyses for coating composition, the mechanisms responsible for these two distinct modes of coating degradation are discussed separately below.

Results of microprobe analyses of coating matrix. The results of typical microprobe analyses of the coating matrix along <100> and <110> orientations for the specimen subjected to rapid 5 s heating are presented in Figs. 14a,b. As with the isothermally oxidized specimen, the microprobe traces of the thermally cycled specimens showed no discernible gradient in element concentration through the coating thickness. For ease of comparison of coating composition between specimens, the results of the microprobe analyses at a distance of 2-5μm from the coating surface (outer-zone matrix), at the coating mid-thickness, and at a distance of 4-8μm from the coating/substrate interface (inner-zone matrix) are summarized in Table 3a, along with results obtained from the isothermally oxidized and as-coated specimens.

Table 3a shows that, except for the low-strain <110> orientations of the specimen subjected to slow 35s heating, the element concentrations in the coating matrix of the thermally cycled specimens were similar, varying between specimens by no more than 0.8 at% for any element. This low-strain <110> orientation of the slowly heated specimen was found to contain approximately 33.7 at% Al, which is roughly 1 at% higher than the

Al content of other thermally cycled specimens. For all thermally exposed specimens there was essentially no gradient in element concentration in the coating matrix.

Results of microprobe analyses of coating precipitates. The low magnification micrographs of Figs. 11a-h and higher magnification companion micrographs of Figs. 15a-h show a bright precipitate film approximately 2 μm wide that appears along most of the coating surface, whether scalloped or not (see analysis points "D"). Similar precipitates occur along many coating grain boundaries and adjacent to cracks formed along <100> directions of the specimen subjected to the rapid cooling cycles (see analysis points "C"). From Table 3b, the Al concentration of these bright precipitates is between 15.9 and 17.2 at% Al (24.6 to 25.7 at% equiv. Al), whereas the Al concentration in the outer-zone matrix of the thermally cycled specimens was approximately 32.5 at%: this corresponds to δ' in a β-matrix (see Fig. 16, Points 4a and 4b).

Microprobe traces performed with 1μm steps showed the change in concentration between the coating matrix and δ' precipitates (surface, grain-boundary, and lower-zone) to be abrupt, indicating that the growth of δ' is interface-controlled, rather than diffusion-controlled. It is interesting to note that the diffusivity of Al in δ' is about an order of magnitude lower than the diffusivity of Al in β [43], which is in agreement with

the lack of a concentration gradient observed in the β-matrix. The angular nature of the interface between the γ' and β-matrix suggests that the interfaces formed have low surface energy.

It is interesting to note that both the isothermally oxidized and thermally cycled specimens show approximately the same drop in bulk Al-concentration in the coating matrix when compared to the as-coated composition (from ≈ 48 at% as-coated, to approximately 34 at% after isothermal exposure, and 32.5 at% after cyclic exposure). This suggests that the ***major*** decrease in bulk-Al coating concentration is the result of interdiffusion between the coating and substrate during long term thermal exposure, rather than significant consumption of Al due to Al_2O_3 formation. The ***pronounced*** Al depletion that results in γ' formation along the coating surface is, however, caused by a more local phenomenon such as continued cyclic cracking of Al_2O_3, allowing localized oxidation of the coating.

The Al depletion and subsequent γ' formation along coating grain boundaries can be attributed at least in part to the increased flux of Al through these boundaries to the coating surface, in response to both cyclic cracking of Al_2O_3 above the boundaries, and the increased grain-boundary flux of Al due to compressive stress acting normal to the columnar grain boundaries.

Coating oxidation. After 6000 cycles the average oxide thickness obtained by thermal cycling varies between 11.5μm for cycling between strains of -0.20% and 0.01% to 24μm for cycling between strains of -0.56% and 0.03% (see Figs. 11a,f). This compares with the 2.5μm thick oxide obtained with isothermal oxidation. With reference to the <110> micrograph for the specimen subjected to the mild 35 s heating (see Fig. 11f), it appears that a critical value of strain or strain rate is required for oxide breakdown and subsequent formation of γ' along the coating surface. This is consistent with the findings of Rahmel [44] which show that cyclic cracking or spalling of Cr_2O_3 on a flat surface requires a critical value of strain.

Oxide stress-strain history

It is likely that oxide breakdown is a precursor to coating scalloping. Thus, to identify those portions of the specimen strain histories that are likely to result in damage of the protective Al_2O_3 oxide, a thin-skin analysis is used here to relate substrate strain history to the stress-strain history of the oxide. The analysis assumes initially that the oxide forms on a flat surface.

As shown in Fig. 18, the Al_2O_3 oxide that forms on the aluminide coating during high temperature exposure has a coefficient of thermal expansion that is 65% that of the coating and substrate. The elastic modulus of polycrystalline Al_2O_3

(Fig. 19) is approximately 70% higher than the <100> substrate modulus and 45% higher than the <110> substrate modulus. Thus, as discussed in detail below, the oxide undergoes a stress history that differs considerably from that of the substrate which sets the strain history of the coating and oxide.

For all temperature histories the Al_2O_3 oxide forms predominantly during the 60 s hold at 1080°C. Thus, prior to specimen cooldown, the oxide stress will be due entirely to intrinsic growth strains[12]. Since the thin oxide offers negligible constraint to the substrate, the increment in total oxide strain $\delta\epsilon_{ox}$ during specimen cooldown or heatup must equal the change in total substrate periphery strain $\delta\epsilon_s$. The increment in total oxide strain $\delta\epsilon_{ox}$ is equal to the sum of the elastic strain $\delta\epsilon_{ox}$ $(=\delta\sigma_{ox}/E_{ox})$ and the strain due to thermal expansion of the oxide $\alpha_{ox}\delta T$:

$$\delta\epsilon_{ox} = \delta\epsilon_s = \delta\epsilon_{ox} + \alpha_{ox}\,\delta T \ . \qquad (2)$$

---

[12]Extrapolation of data for the diffusivity of Al^{3+} and O^{2-} ions in polycrystalline Al_2O_3 [45] shows that at 1080°C the bulk diffusivity of Al^{3+} is an order of magnitude higher than O^{2-} diffusion. Thus, the oxide grows at the oxide/gas interface. This fact, in addition to a low Pilling-Bedworth ratio of 1.3 (P.B. ratio ≡ Vol. of 1 mol. of oxide/Vol. of metal to produce 1 mol. of oxide), would tend to minimize growth stresses. Furthermore, the oxide that forms is polycrystalline; thus strains caused by epitaxial oxide growth are absent.

Equating this strain increment to the total strain increment in the substrate which, ignoring inelastic deformation, has only elastic ($\delta\epsilon_S$) and thermal ($\alpha_{ox}\,\delta T$) components, gives

$$\delta\epsilon_{ox} = \delta\epsilon_S + (\alpha_S - \alpha_{ox})\delta T \quad . \tag{3}$$

It is important to note that the substrate strain, and therefore the oxide strain, is a function of periphery orientation (see Figs. 10a-d).

For a change in oxide strain given by Eq. 3 the change in circumferential stress in the oxide is[13]

$$\delta\sigma_{ox} = E_{ox}[\delta\epsilon_S + (\alpha_S - \alpha_{ox})\delta T] \quad . \tag{4}$$

The peak tensile and compressive oxide stress and stress range determined from Eq. 4 are summarized in Table 4.

---

[13]The present discussion is limited to initiation of a surface scallop. Once a scallop has developed the stress and strain in the oxide predicted by Eqs. 3 and 4 would be increased by strain intensification at the root of the scallop.

During **cooling**, the oxide that formed on the already compressively strained periphery, will tend to expand as the compressed periphery undergoes elastic expansion from redistribution of stress in the disk. This elastic substrate expansion upon cooling gives a **positive** contribution to the elastic oxide stress $\delta\sigma_{ox}$. This positive increment in oxide stress is countered by the strain generated due to differences in thermal expansion between the coating and oxide, so that for $\alpha_s > \alpha_{ox}$ and $\delta T < 0$, a compressive contribution to the oxide stress increment results. The total stress increment in the oxide $\delta\sigma_{ox}$ depends upon the relative magnitude of these elastic and thermal components, according to Eq. 4. Thus, in the **early** stages of specimen cooldown, where the decrease in elastic compressive substrate strain (increase in $\delta\epsilon_s$) is rapid and of greater magnitude than the negative thermal contribution $(\alpha_s - \alpha_{ox})\delta T$, **tension** is produced in the oxide. Since the compressive substrate strain developed **prior** to specimen cooldown from 1080^0C is greatest along <100> peripheries, whereas the thermal strain increment is isotropic, the oxide tension produced during cooldown will be greatest along <100> peripheries. For all orientations of the slowly cooled specimens, the peak oxide tension develops at 950^0C and decreases in magnitude with further cooling, becoming compressive at approximately 700^0C.

During **heating**, elastic compression of the substrate due to unequal heating results in a negative contribution to oxide stress

($E_{ox}\delta\epsilon_s < 0$), whereas the mismatch in thermal expansion coefficients between substrate and oxide produces a positive contribution to the oxide stress ($E_{ox}(\alpha_s-\alpha_{ox})\delta T > 0$). The large negative increments in elastic substrate strain which occur on initial heatup for the rapid 5s heating rate results in a maximum oxide compression of -900 MPa at 1057°C, prior to achievement of a steady-state temperature at 1080°C. For all other temperature histories the maximum compressive oxide stress during specimen heatup was reached at a lower temperature (see Table 4). Since oxide growth stresses and inelastic behavior are ignored, the oxide stress and strain must return to zero at the completion of a full temperature cycle (1080°C to 1080°C). It should be noted that a shift in mean coating-stress towards zero will not affect the oxide stress history, which is governed by the coating **strain**.

Coating Scalloping

Possible mechanisms for the initiation and growth of a surface scallop are discussed with reference to the stress-strain history of the surface oxide and the strain history of the aluminide coating.

Scallop initiation. Oxide breakdown (by cracking or spallation) and subsequent surface roughening by coating oxidation is a likely precursor to scallop initiation. Oxide cracking can occur during specimen cooling where, as discussed earlier, tensile stresses

develop in the oxide. Compressive shear cracking or spallation of the surface oxide is possible during the initial stages of specimen heating where elastic substrate compression produces oxide compression. Initial oxide breakdown would be expected to occur first at coating grain boundaries where a higher than average oxide growth rate typically occurs due to rapid Al diffusion to the coating surface along coating grain boundaries [46].

SEM examination of the oxide formed on the thermally cycled specimens showed the presence of oxide cracking and spallation (on a scale small compared to the oxide thickness) along all substrate orientations. These examinations showed that many of the oxide cracks were inclined at angles between 30 and 60°C from the circumferential stress direction; implying compressive shear cracking of the surface oxide may have occurred. The extent of oxide cracking and spallation was most severe along the highly strained <100> substrate orientations (see Figs. 20a,b for SEM micrographs of the surface oxide developed after 6000 cycles of 8s heating and 30s cooling).

Examination of Table 4 shows that the tensile oxide stress developed along like orientations of the slowly cooled specimens is identical: 600 MPa for <100> orientations and 260 MPa for <110> orientations. Thus, the contribution to oxide breakdown by tensile cracking is the same along like orientations of the slowly cooled specimens. The lack of appreciable coating

roughening observed along the <110> orientations of the specimen subjected to 35s heating and slow cooling (Fig. 11f), suggests that tensile oxide stress acting alone is not responsible for the initial surface roughening that is a likely precursor to scallop growth.

Examination of Table 4 shows that for a given substrate orientation the compressive oxide stress increases as the specimen heating rate increases. Thus, along a given substrate orientation, the extent of shear-cracking and compressive spallation of the oxide should increase with an increase in specimen heating rate, as verified by SEM examination of the surface oxide formed on all specimens. Thus, compressive shear cracking of the oxide, acting alone or in conjunction with tensile oxide stresses, and if of sufficient magnitude, offers another avenue for initial oxide breakdown and localized coating oxidation.

To summarize, it appears that oxide compression, acting alone or in conjunction with oxide tension, is responsible for initial breakdown of the protective surface oxide. Once oxide breakdown has occurred, surface roughening can develop by the cyclic process of oxide cracking and localized coating oxidation.

Scallop growth by repeated oxide cracking. As discussed above, the tensile oxide stress developed during cooldown along

like orientations of the slowly cooled specimens is identical (see Table 4). Therefore, if repeated tensile oxide cracking during specimen cooldown were the **principal** parameter that determined growth of a coating scallop, a similar degree of scalloping would be expected along like orientations of these specimens; the scalloping shown in Figs. 11a-f shows that this is clearly not the case (see also Table 4).

Although compressive shear cracking of the oxide can contribute to the initial surface roughening which is a precursor to scalloping, cyclic oxidation tests by Fleetwood [47] suggest that continued scallop growth by this mechanism is unlikely and that, in addition, elastic substrate straining is necessary for scallop growth. In Fleetwood's work, 12 mm dia. by 6 mm thick button specimens of polycrystalline Ni-Cr-Al-Ti-Co-Mo alloys (which form Al_2O_3 during high-temperature oxidation) were subjected to 1500 cycles consisting of 15 minutes heating to 1050^{0}C in a refractory furnace, followed by 5 minutes cooling in air to 150^{0}C. The results of Fleetwood's work show that although a continuous layer of $\gamma'(Ni_3Al)$ had formed beneath the Al_2O_3 as a result of long term exposure (500 hrs), only minor surface roughening and no scalloping of the aluminide coating had occurred. Unfortunately, Fleetwood gives no data for the expected stress-strain history of the specimens or oxide (heating and cooling curves are also not given). However, as an approximation, it can be assumed that the slow heating and cooling rates produce

uniform heating and cooling of the substrate. Thus, with negligible constraint from the thin surface-oxide, the elastic substrate strains during heating and cooling are essentially zero. In the absence of elastic substrate strains, the stress and strain developed in the oxide is due entirely to differences in thermal expansion between the substrate and surface oxide. This gives an approximate compressive oxide strain of $(\alpha_S - \alpha_{OX})\delta T = -(8.5 - 14.0)\times10^{-6}\ {}^{o}C^{-1} \times (-900^{o}C) = \mathbf{-4.95\times10^{-3}}$ and a compressive stress of $E_{OX}(\alpha_S - \alpha_{OX})\delta T = \mathbf{-1690\ MPa}$. These values are larger than those encountered in the present study, where a maximum compressive oxide strain of $\mathbf{-2.8\times10^{-3}}$ and stress of **-900 MPa** are encountered (see Table 4). Thus, the **absence** of surface scalloping observed in Fleetwood's specimens, with their negligible elastic substrate strain but approximately 50% higher compressive oxide stress, suggests that although **initial** surface roughening can occur as a result of cyclic shear cracking of the oxide, elastic or plastic substrate straining is required for further scallop growth.

It should be noted that although tensile or shear oxide cracking does not appear to be the mechanism ***directly*** responsible for scallop growth, the strain intensification at the root of a coating scallop could produce enhanced oxide cracking. Thus, it is possible that oxide cracking could act in parallel with another mechanism for further scallop growth.

Scallop growth by kinematically irreversible cyclic creep. As shown in Figs. 21a,b the average depth of coating scalloping correlates approximately with peak compressive substrate strain (≡ peak compressive coating strain) and substrate strain-range (≡ coating strain range). A mechanism for scallop growth consistent with this correlation is kinematically irreversible cyclic creep of the aluminide coating produced by elastic substrate strains.

If primary creep has a Bauschinger component on load reversal, continued scallop growth due to cyclic creep is possible[14]. Growth by this mechanism is in analogy with the continued surface roughening found by McClintock [49] for cyclic plastic straining of power-law hardening materials under constant strain amplitude. As shown schematically in the 1-D model of Fig. 22, an area difference between two adjacent regions of the coating undergoing cyclic creep produces a strain difference between the two regions. This strain difference ***increases*** with continued cycling due to the kinematically irreversible Bauschinger component of creep. This increasing strain difference ***increases*** the area difference between the two deforming regions. The essential feature of this mechanism is the increased area difference expected with increasing creep amplitudes, **consistent** with the correlation of average scallop depth with

---

[14]Pure power-law creep is kinematically reversible and would therefore give no net scallop growth, as proven by Berg and McClintock [48].

coating strain range (Fig. 21b).

Proposed mechanism for coating scalloping. The proposed mechanism for coating scalloping involves the following steps:

1. Initial breakdown of the oxide due to tensile or compressive (shear) oxide cracking, followed by localized coating oxidation and surface roughening. A likely site for initial oxide breakdown would be near coating grain boundaries, where a high initial flux of Al would be expected to result in rapid oxide formation and an initially larger than average oxide thickness.

2. Continued growth of coating scallops as a result of the inherent instability of a surface depression subjected to kinematically irreversible cyclic creep and enhanced oxide cracking at the root of a surface depression.

Coating cracking.

For the rapidly cooled specimen, cracking along coating grain boundaries is observed for <100> directions. No coating cracking was observed along <110> directions. Examination of Fig. 15g and Table 3b, shows that the cracks are lined with Al-poor δ' (Point C), of similar composition to the δ' that forms along the coating surface (Point D).

For the <100> orientations the 6s cooling time produced a

peak tensile strain of 0.20% during cooldown, at a temperature of 700°C (see substrate strain history of Fig. 10d). Allowing for a possible shift in mean-stress towards zero would give a maximum tensile strain of 0.50% in the coating during cooldown from the hold strain of -0.30% at 1080°C. For zero mean-stress an upper limit for the strain rate in the coating is 0.0050/2s = 0.0025 s^{-1} (from Fig. 10d). For this strain rate and a temperature of 700°C, Fig. 23 shows the strain to cracking for CODEP coatings applied to Rene 125 (an alloy of similar composition to Rene N4) is approximately 1% [42]. Thus, one is tempted to conclude from Fig. 23 that early coating cracking is unlikely and therefore cracking must occur after formation of the less ductile grain-boundary δ'. Two factors tend to discount this and suggest that grain boundary cracking occurs early in the test:

(1) Had cracking occurred after δ' formation along grain boundaries, we would expect to observe signs of deformation between the discontinuous δ' islands that line uncracked grain boundaries. The lack of this deformation suggests that cracking occurs early in the test prior to <u>extensive</u> δ' formation.

(2) Fig. 23 and similar coating ductility plots [1,50,51] are typically constructed by using a 20X objective to visually observe cracking of coatings applied to cylindrical tensile-type specimens. Thus, the strain recorded will be that for

macroscopic coating and substrate cracking, with early cracking occurring at lower strains.

It is interesting to note that the degradation observed along <110> orientations (Fig. 11f), where coating cracking did not occur, correlates roughly with substrate peak compressive strain and strain range (Figs. 21a,b).

In summary, the critical substrate strain for coating cracking lies in the range $0.08\% < \epsilon_{crit} < 0.20\%$. For this range, coating cracking appears to occur early in the coating life, with subsequent depletion of Al along coating grain-boundaries, resulting in formation of Al-poor δ' films.

Conclusions

1. No influence of substrate crystallographic orientation on coating composition was observed, except through substrate strain amplitude.

2. Aluminide coating degradation in oxidizing atmospheres depends critically upon the strain history of the substrate, which in turn sets the strain history of the thin aluminide coating and Al_2O_3 surface oxide.

3. Depending upon periphery strain history, two modes of coating degradation are observed: (1) scalloping, which occurs during

rapid heatup and slow cooling for $\Delta\epsilon > 0.21\%$ and (2) coating cracking, which was observed during rapid cooldown of the coating for $\Delta\epsilon = 0.65\%$.

4. Coating scalloping is not observed for a peak compressive coating strain below **-0.20%**, with a strain range of **0.21%**. Tolerable scalloping (<10% of total coating thickness) was observed for a peak compressive strain of -0.29%, with a strain range of 0.30%. Thus, to prevent coating scalloping, which is the result of compressive strains generated in the substrate during heatup, it is necessary to maintain the peak compressive coating strain below -0.20%, with the strain range held below 0.21%. For ship and commercial aircraft gas turbines, coating degradation due to compressive scalloping can be reduced by increasing the turbine to full power at a slower rate (e.g., in 15s rather than 5s). This will reduce the temperature gradients in the airfoils which are responsible for compressive strains.

5. To preclude early coating cracking in oxidizing environments it is necessary to limit substrate tensile strains to approximately **0.06%** (based, on a pseudo-elastic analysis). As tensile strains are encountered on turbine cooldown after thrust reverse, the practical solution would be to reduce engine speed at a slower rate after thrust reverse, a practice that is not currently employed by commercial aircraft companies but could be implemented.

6. Average scallop depth correlates well with peak compressive substrate strain and substrate strain range. A mechanism for coating scalloping consistent with this correlation involves initial surface roughening by tensile or compressive (shear) oxide cracking, followed with scallop growth by kinematically irreversible cyclic creep.

Table 3a Composition of coating matrix 2-5μm from coating surface (o), at coating mid-thickness (m), and 4-8μm from coating/substrate interface (i). See figures referenced for location of analysis points along microprobe trace line. See Figs. 10a-d or Table 4 for corresponding periphery strains.

Fig.	Temp. hist heat	Temp. hist cool	<iji>	location	Element Ni	Co	Al	Ti	Ta	Mo	W	Cr
12	as-coated		<100>	o	45.1	4.0	48.2	0.4	0.1	0.1	0.1	2.0
				m	46.5	4.3	46.1	0.5	0.1	0.1	0.1	2.8
				i	48.0	5.5	36.6	4.4	0.4	0.4	0.6	4.1
13	isothermal		<100>	o	49.4	6.0	34.3	3.9	0.5	0.2	0.1	5.7
				m	49.3	5.8	34.3	3.9	0.5	0.2	0.1	5.7
				i	49.1	5.9	34.8	3.8	0.5	0.1	0.1	5.5
15a	5	30	<100>	o	50.9	5.6	32.3	3.5	0.4	0.2	0.0	7.1
				m	50.4	5.8	32.5	3.5	0.5	0.1	0.1	7.2
				i	50.9	5.6	32.4	3.3	0.5	0.2	0.1	7.0
15b	"	"	<110>	o	50.8	5.8	32.1	3.5	0.5	0.2	0.0	7.3
				m	50.8	5.7	32.2	3.4	0.5	0.2	0.0	7.2
				i	50.8	5.6	32.3	3.4	0.5	0.2	0.1	7.2
15c	8	30	<100>	o	50.7	5.5	32.2	3.6	0.5	0.1	0.0	7.3
				m	50.7	5.8	32.4	3.4	0.5	0.2	0.0	7.1
				i	50.6	5.8	32.4	3.4	0.3	0.2	0.0	7.1
15d	"	"	<110>	o	50.6	5.6	32.8	3.6	0.5	0.1	0.1	7.9
				m	50.5	5.8	32.8	3.6	0.4	0.1	0.0	7.8
				i	50.8	5.7	32.7	3.4	0.4	0.1	0.0	7.8
15e	35	30	<100>	o	50.9	5.6	32.2	3.4	0.4	0.1	0.0	7.2
				m	51.1	5.4	32.4	3.4	0.4	0.2	0.0	7.1
				i	50.9	5.4	32.6	3.5	0.4	0.2	0.1	7.0
15f	"	"	<110>	o	49.9	5.8	33.6	3.7	0.3	0.1	0.0	6.5
				m	50.0	5.7	33.6	3.7	0.4	0.1	0.0	6.5
				i	49.9	5.6	33.8	3.7	0.4	0.2	0.0	6.3
15g	8	6	<100>	o	51.0	5.6	32.1	3.4	0.4	0.0	0.0	7.4
				m	51.1	5.4	32.2	3.4	0.4	0.1	0.0	7.4
				i	51.2	5.5	32.2	3.1	0.4	0.0	0.0	7.4
15h	"	"	<110>	o	50.8	5.6	32.6	3.7	0.3	0.1	0.0	7.1
				m	50.2	5.5	32.8	3.6	0.6	0.2	0.0	7.2
				i	50.2	5.5	32.7	3.6	0.6	0.2	0.1	7.2

Table 3b Range of compositions of precipitates present in aluminide coating applied to Rene N4 (see analysis points A-D, Figs. 15a-h).

Point	Description	Element							
		Ni	Co	Al	Ti	Ta	Mo	W	Cr
A	refractory ppt. (lower-zone)	20.6 ±0.5	14.0±0.5	2.2±0.4	0.8±0.3	3.0±0.4	8.2±0.4	19.7±0.7	30.5±0.8
B	γ' (inner- zone)	64.9±0.5	6.2±0.3	16.8±0.4	6.5±0.4	2.8±0.3	0.1±0.1	0.3±0.1	3.1±0.4
C	γ' (g.b.)	65.2±0.4	6.1±0.4	16.4±05	6.4±0.3	2.6±0.3	0.1±0.1	0.2±0.1	3.0±0.3
D	γ' (surface)	65.0±0.5	6.2±0.4	16.5±0.5	6.3±0.4	2.5±0.3	0.1±0.1	0.3±0.1	3.2±0.4

Table 4 Peak substrate strain and strain range, peak oxide stress and stress range, and depth* and spacing of major scallops.

Temp. history		Orientation	Substrate strain history, peak, %			Peak oxide stress and range, Mpa			Depth and spacing of major scallops	
heat	cool	<iii>	comp.	range	tension	comp.(T,^{0}C)	range	tension (T,^{0}C)	depth	spacing
5	30	100	-0.56	0.59	0.03	-900 (1060)	1500	600 (950)	74μm	62μm
		110	-0.36	0.37	0.01	-890 (830)	1150	260 (")	26	65
8	30	100	-0.45	0.48	0.03	-535 (950)	1135	600 (")	49	60
		110	-0.29	0.30	0.01	-530 (630)	790	260 (")	17	78
35	30	100	-0.30	0.33	0.03	-280 (680)	880	600 (")	29	70
		110	-0.20	0.21	0.01	-330 (595)	590	260 (")	neg.	neg.
8	6	100	-0.45	0.65	0.20	-535 (950)	1415	880 (720)	100**	62**
		110	-0.29	0.37	0.08	-530 (555)	840	312 (850)	21	65

*Scallop depth was determined by measuring the distance between the substrate and scallop root and subtracting these values from the nominal coating thickness of 90μm. Only those depths that measured over 10% of the maximum depth observed for a given specimen were included in the calculation of average scallop depth.

**These distances correspond to the length and spacing of coating cracks.

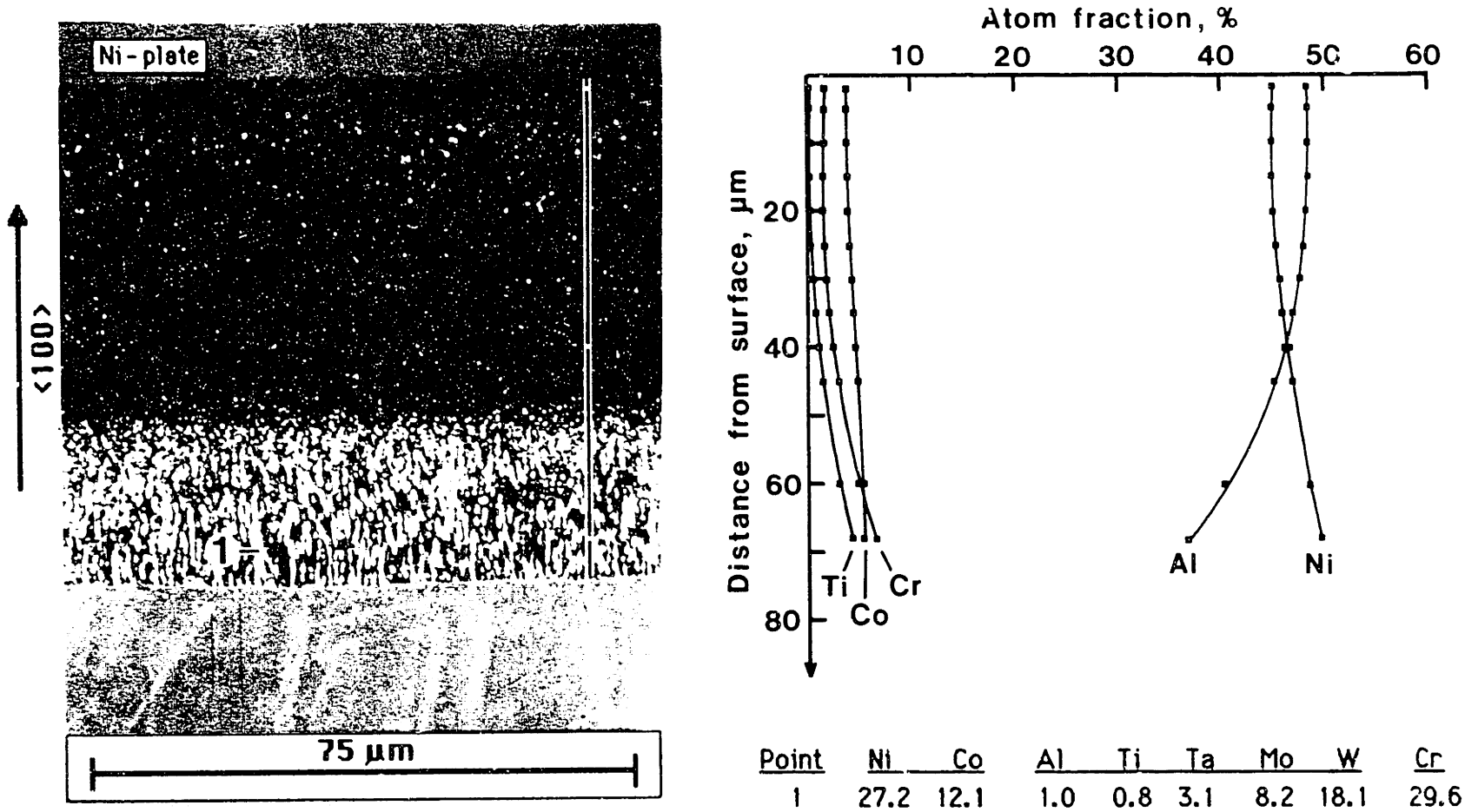

Point	Ni	Co	Al	Ti	Ta	Mo	W	Cr
1	27.2	12.1	1.0	0.8	3.1	8.2	18.1	29.6

Fig. 12 Backscattered electron micrograph of aluminide coating and results of microprobe analyses *prior* to isothermal or cyclic exposure. Matrix analysis is given in graph (performed along black trace-line). Precipitate analysis (Point 1) is given in Table.

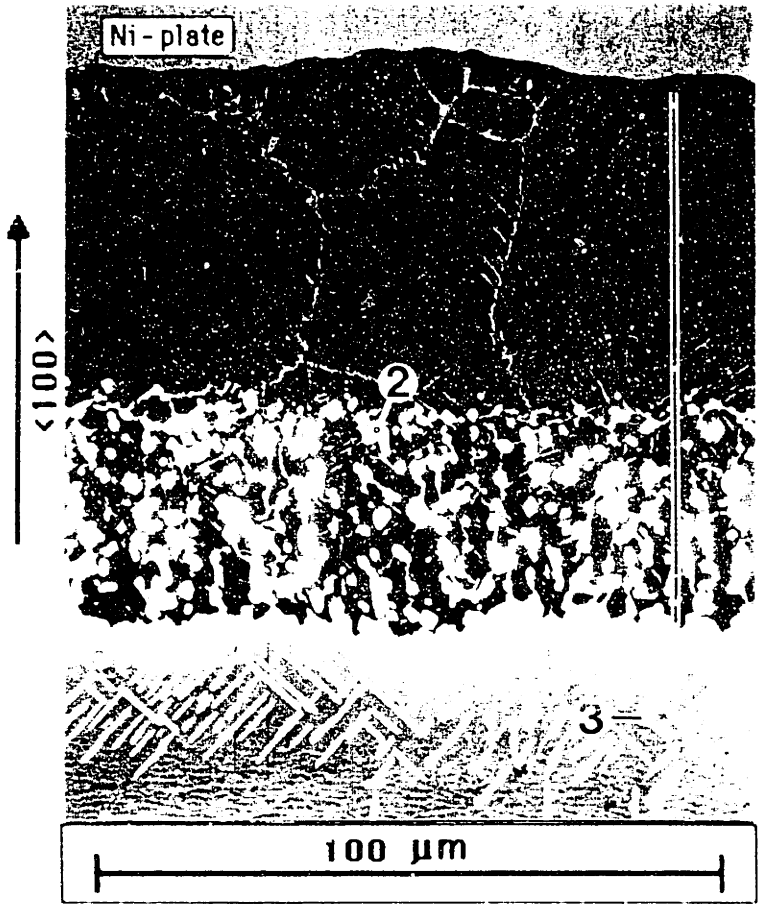

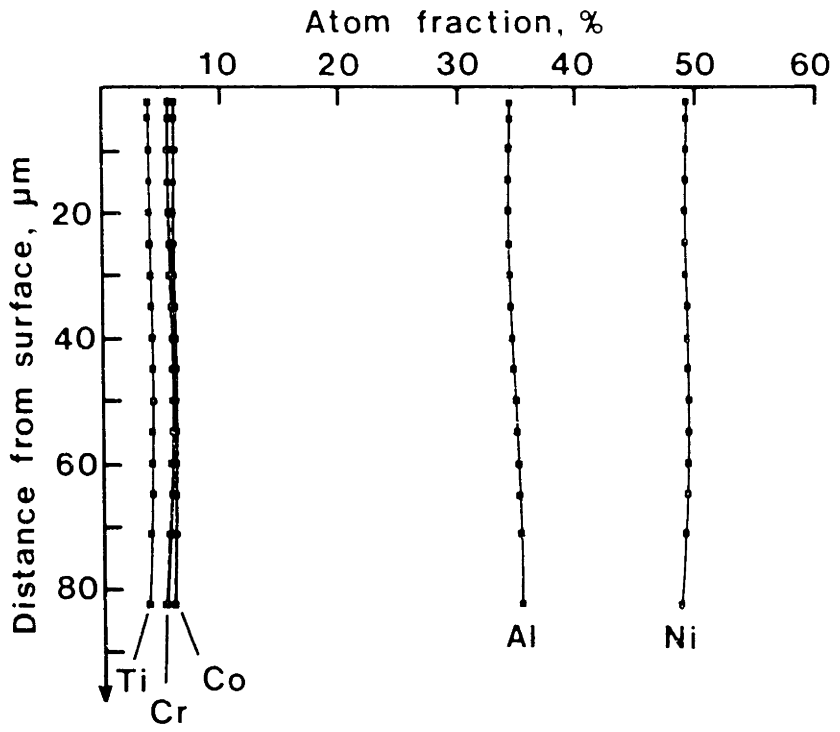

Point	Ni	Co	Al	Ti	Ta	Mo	W	Cr
2	23.5	13.1	1.3	0.8	3.2	8.0	20.2	29.2
3	30.7	12.5	2.3	2.6	0.3	5.3	8.0	38.0

Fig. 13 Backscattered electron micrograph of aluminide coating and results of microprobe analyses *after* isothermal exposure (120 hr at 1080°C). Matrix analysis is given in graph (performed along black trace-line). Precipitate analyses (Points 2,3) are given in Table.

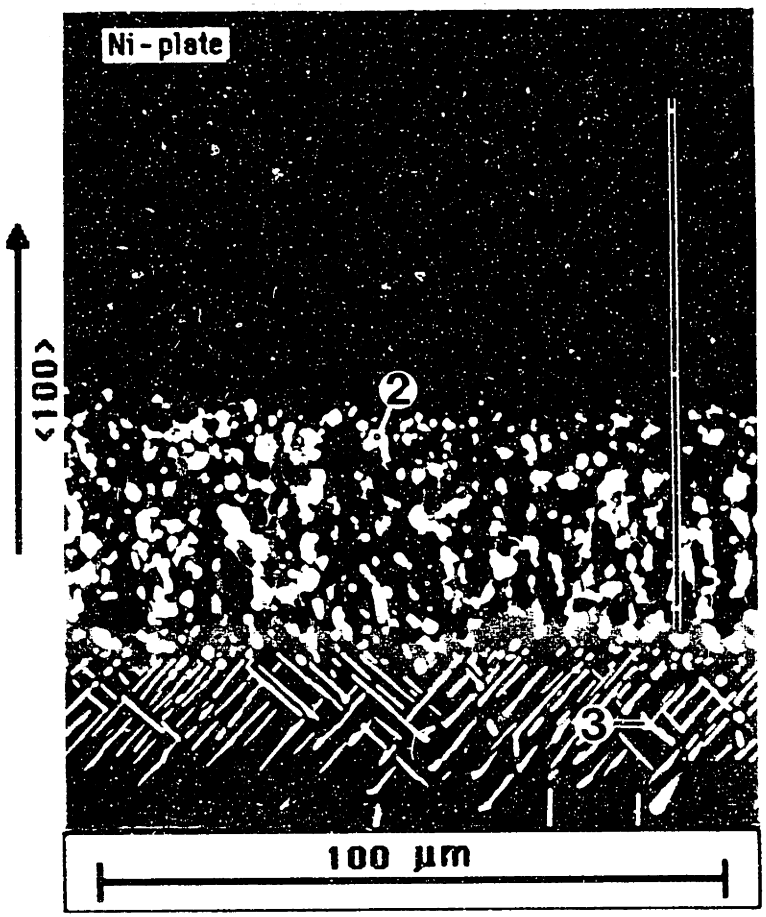

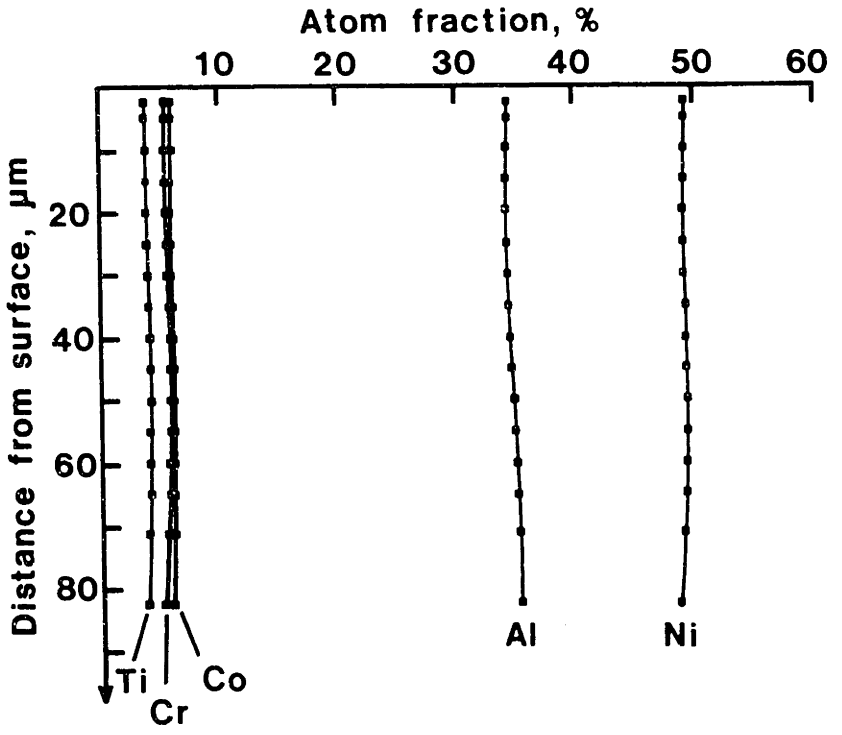

Point	Ni	Co	Al	Ti	Ta	Mo	W	Cr
2	23.5	13.1	1.3	0.8	3.2	8.0	20.2	29.2
3	30.7	12.5	2.3	2.6	0.3	5.3	8.0	38.0

Fig. 13 Backscattered electron micrograph of aluminide coating and results of microprobe analyses *after* isothermal exposure (120 hr at 1080°C). Matrix analysis is given in graph (performed along black trace-line). Precipitate analyses (Points 2,3) are given in Table.

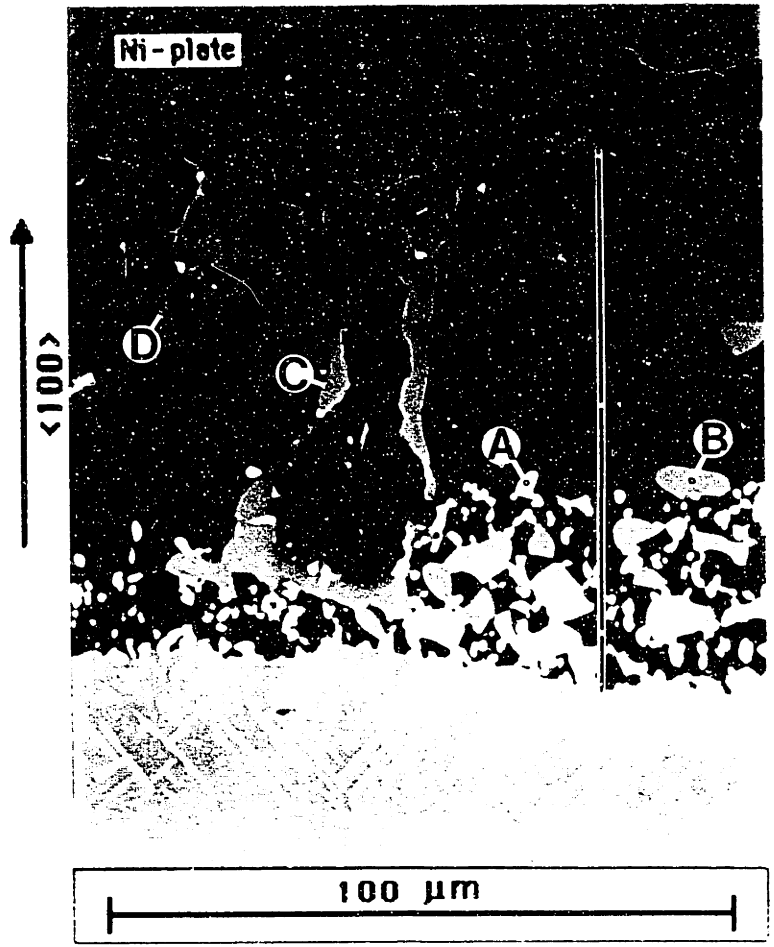

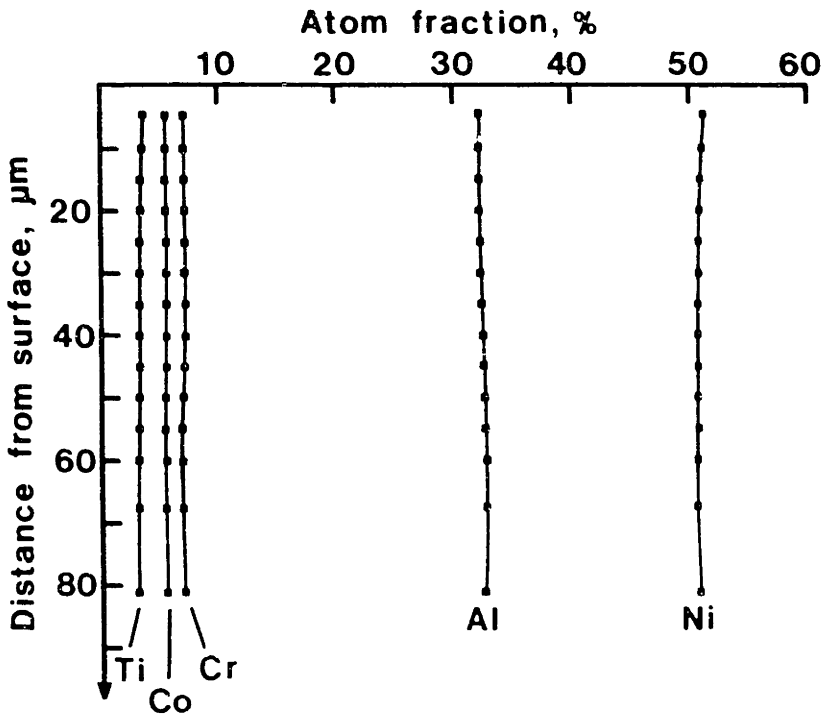

Point	Ni	Co	Al	Ti	Ta	Mo	W	Cr
A	21.0	13.9	2.5	0.9	3.0	8.5	19.6	30.6
B	64.5	6.2	16.8	6.8	2.8	0.0	0.4	3.3
C	65.1	6.2	16.2	6.6	2.6	0.1	0.2	3.0
D	65.0	6.4	16.5	6.7	2.5	0.1	0.4	3.2

Fig. 14a Backscattered electron micrograph of aluminide coating and results of microprobe analyses *after* cyclic exposure. Periphery strain history: $-0.56\% < \epsilon < 0.03\%$. Temperature history (Fig. 7a): 5s heat, 30s cool. Matrix analysis is given in graph (performed along black trace-line). Precipitate analyses (Points A-D) are given in Table.

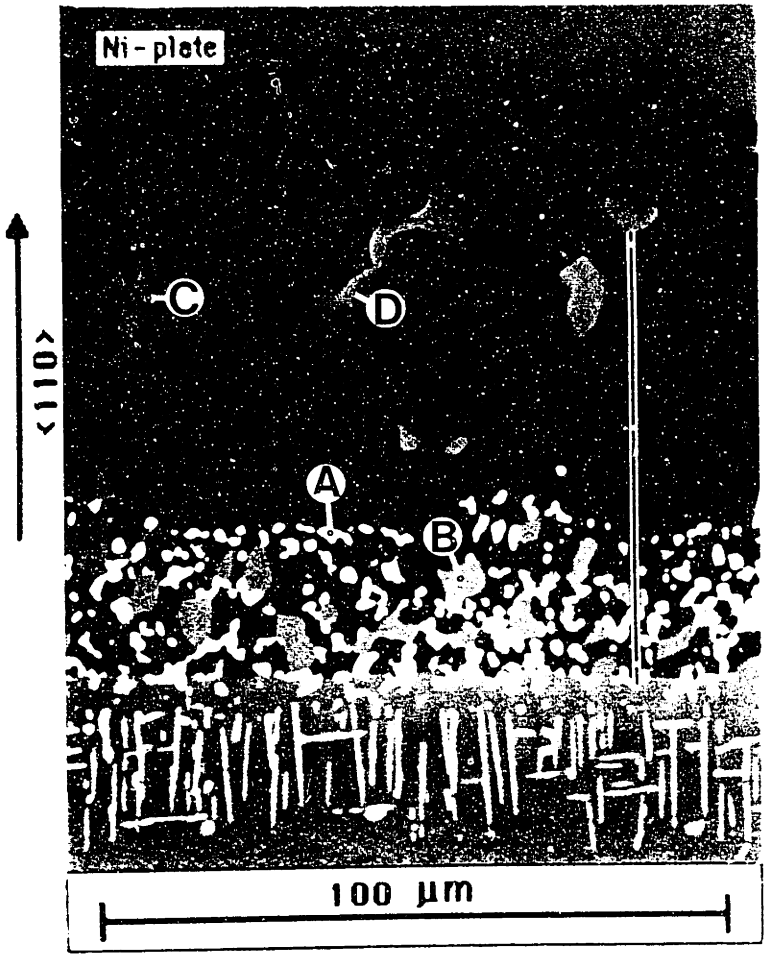

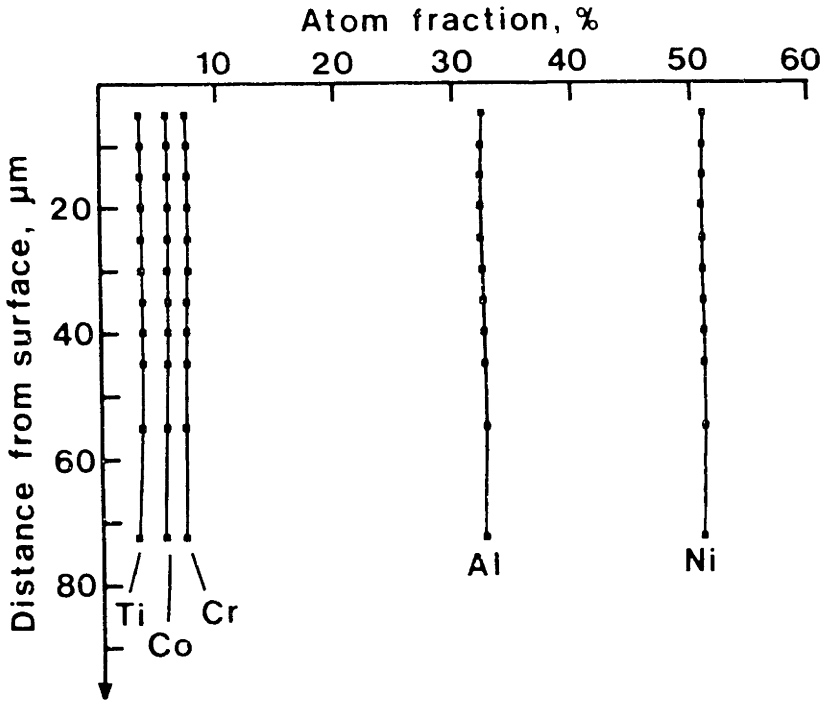

Point	Ni	Co	Al	Ti	Ta	Mo	W	Cr
A	20.3	14.4	2.1	0.7	3.2	8.0	20.0	31.2
B	65.1	6.2	16.5	6.1	2.9	0.1	0.3	2.8
C	65.5	6.0	16.4	6.1	2.7	0.1	0.2	2.9
D	64.8	5.9	16.8	6.2	2.6	0.1	0.3	3.2

Fig. 14b Backscattered electron micrograph of aluminide coating and results of microprobe analyses *after* cyclic exposure. Periphery strain history: $-0.36\% < \epsilon < 0.01\%$. Temperature history (Fig. 7a): 5s heat, 30s cool. Matrix analysis is given in graph (performed along black trace-line). Precipitate analyses (Points A-D) are given in Table.

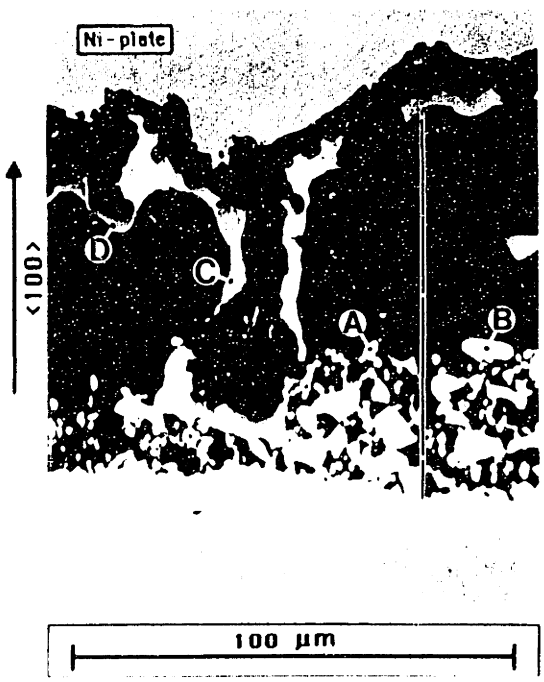

(a) <100> (-0.56% < ε < 0.03%)

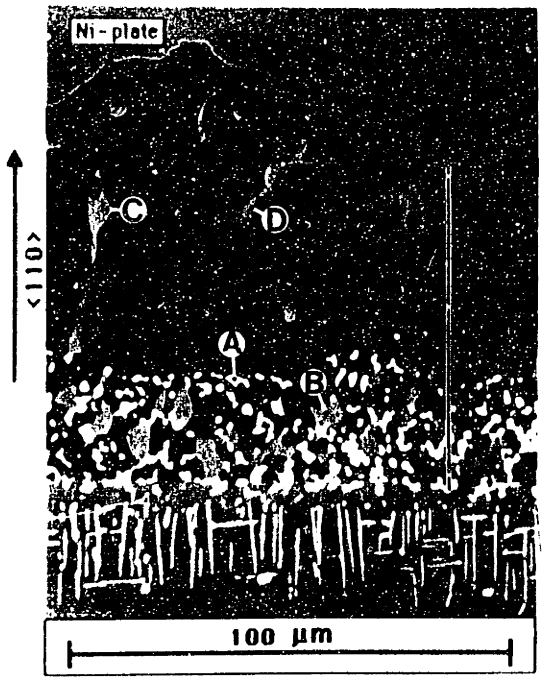

(b) <110> (-0.36% < ε < 0.01%)

Periphery temperature history (Fig. 7a): 5 s heat, 30 s cool.

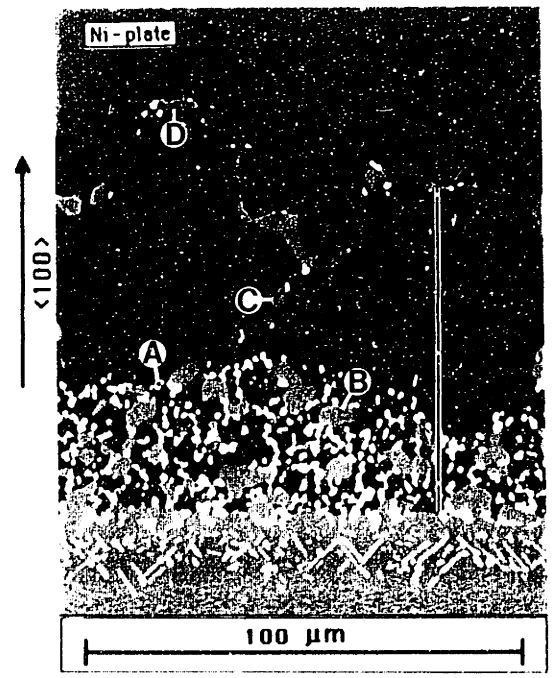

(c) <100> (-0.45% < ε < 0.03%)

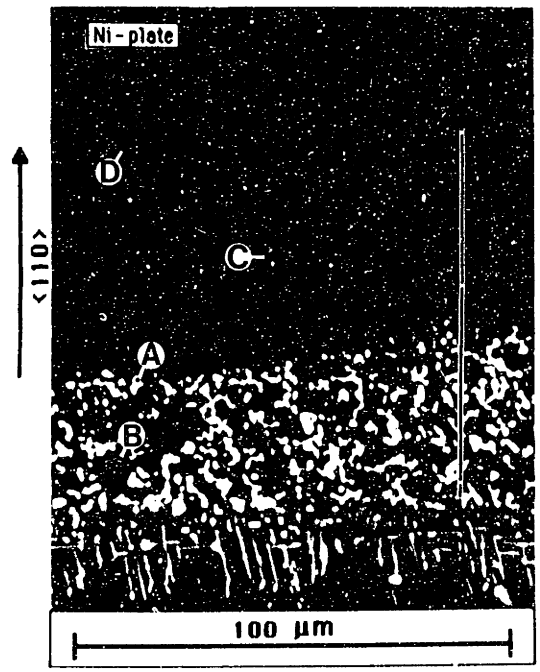

(d) <110> (-0.29% < ε < 0.01%)

Periphery temperature history (Fig. 7b): 8 s heat, 30 s cool.

Figs. 15a-h Backscattered electron micrographs of aluminide coating showing microprobe analysis points along <100> and <110> orientations. Breaks in the black trace-line indicate analysis points referenced in Table 3a. Analysis points A-D are given in Table 3b. Substrate strain history is given in parentheses below Figures. Lower magnification companion micrographs are given in Figs. 11a-h.

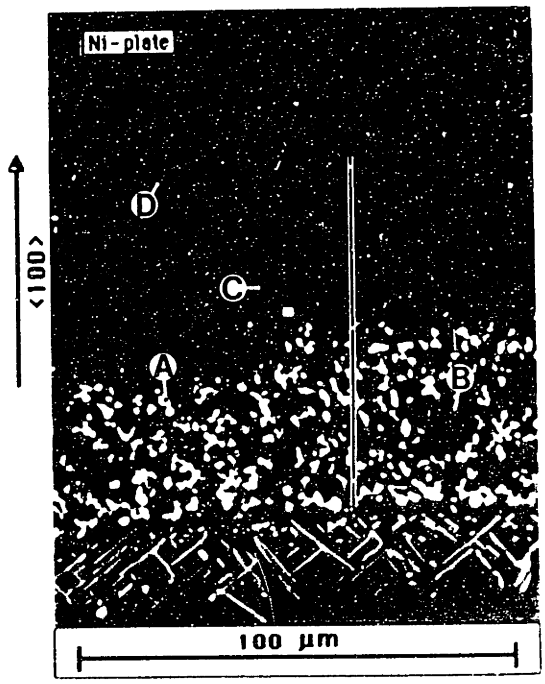

(e) <100> (−0.30% < ϵ < 0.03%)

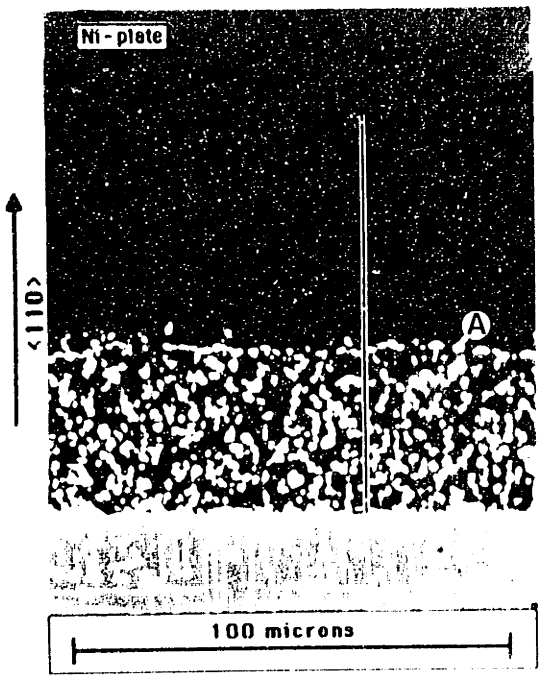

(f) <110> (−0.20% < ϵ < 0.01%)

Periphery temperature history (Fig. 7c): 35 s heat, 30 s cool.

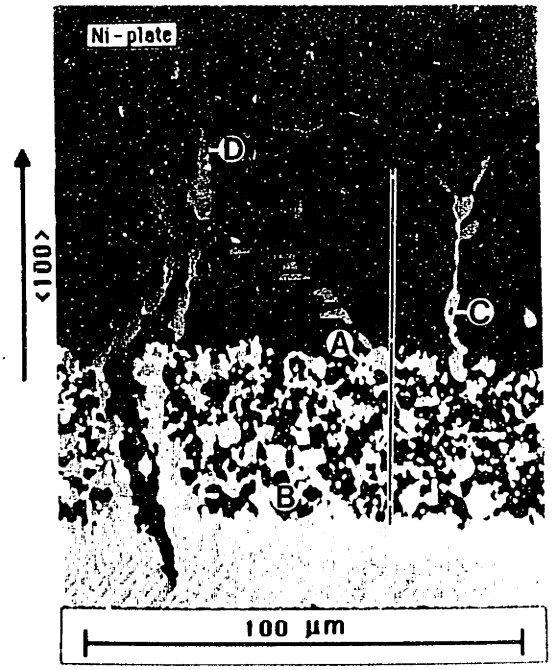

(g) <100> (−0.45% < ϵ < 0.20%)

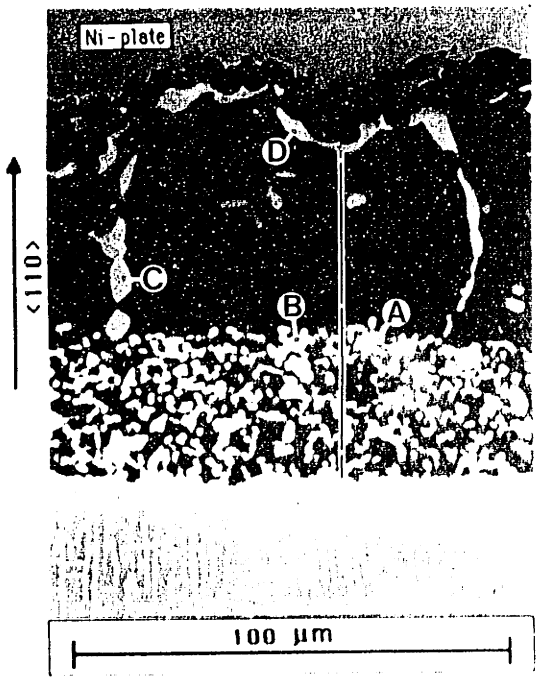

(h) <110> (−0.29% < ϵ < 0.08%)

Periphery temperature history (Fig. 7d): 8 s heat, 6 s cool.

Fig. 15 (continued).

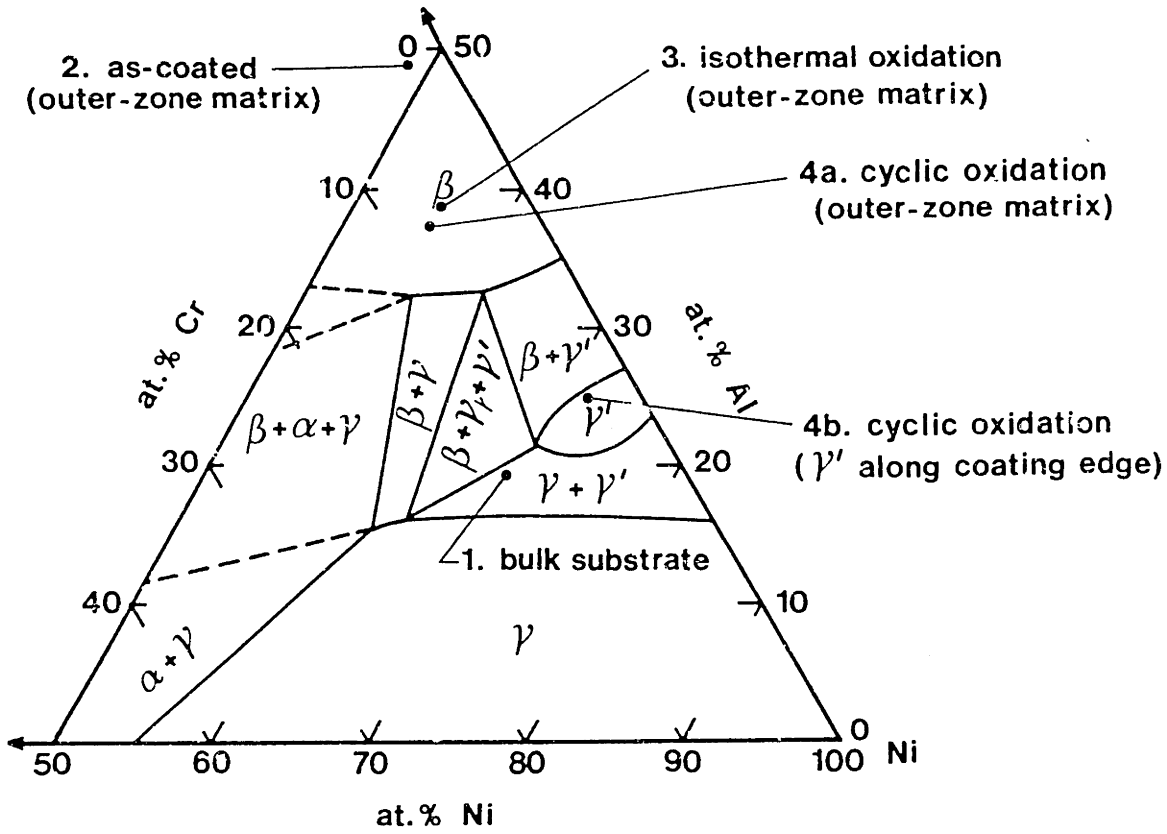

Fig. 16 Ni-Cr-Al phase diagram at 1080°C. From interpolation between Taylor and Floyd's [52] 1000 and 1150°C phase diagrams. The analysis points shown for the coating matrix were taken 10μm from the coating surface.

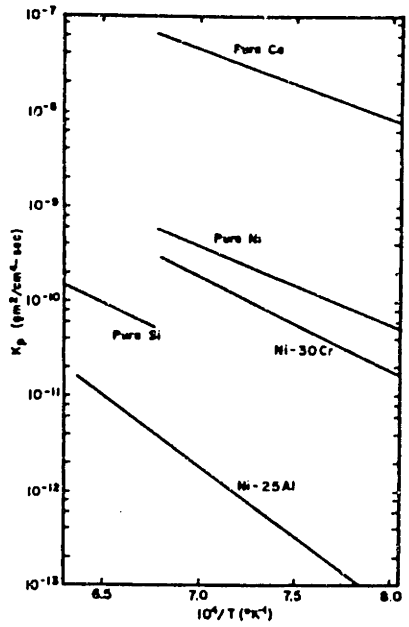

Fig. 17 Temperature dependence of parabolic rate constant for the growth of Al_2O_3 on unalloyed Ni-25Al. From Pettit and Goward [40].

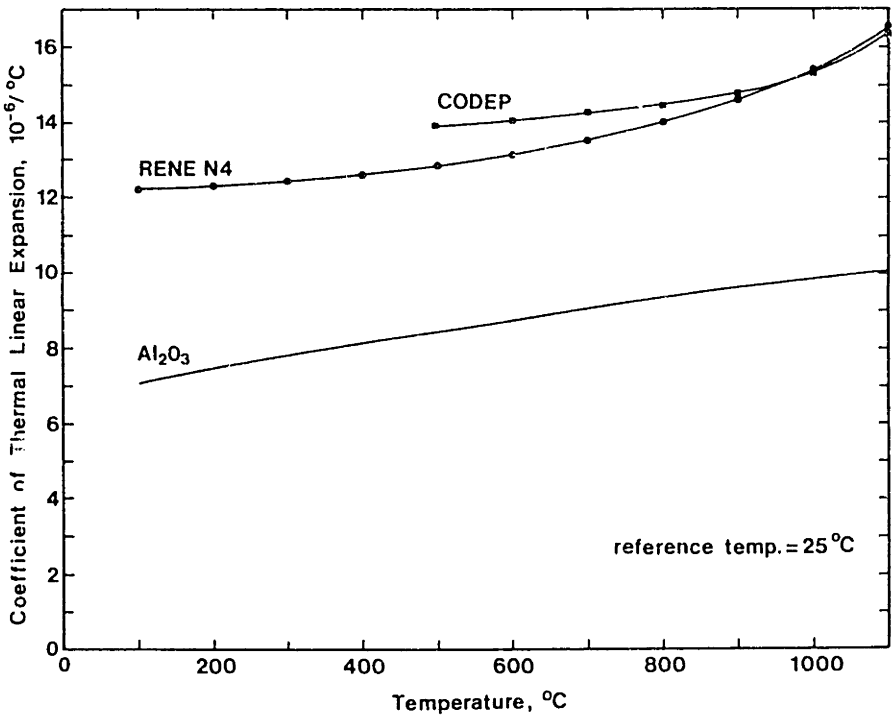

Fig. 18 Coefficient of thermal linear expansion versus temperature for polycrystalline Al_2O_3 [53], Rene N4 [41] and CODEP coating [41].

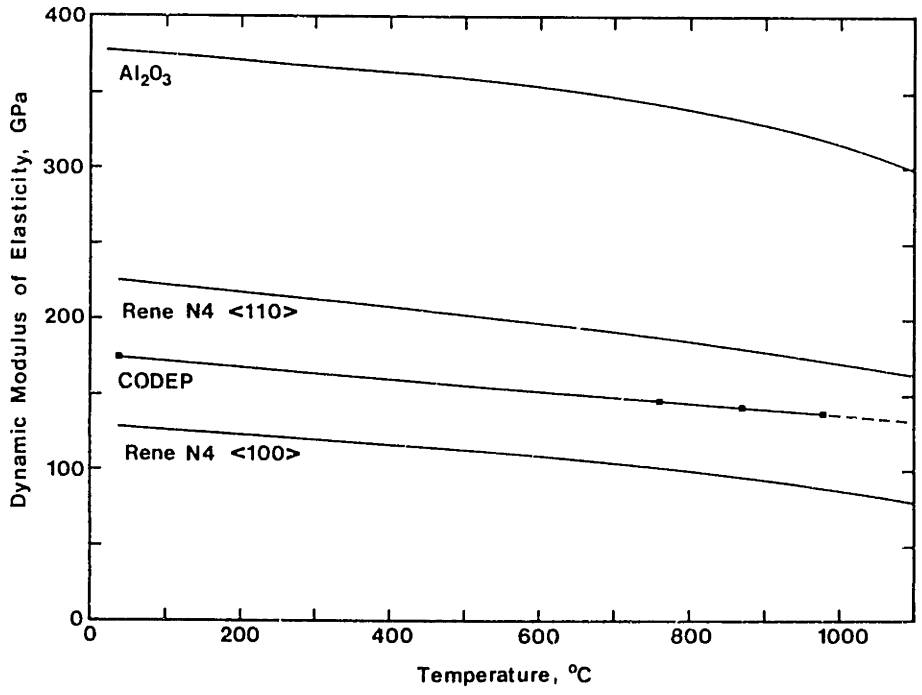

Fig. 19 Dynamic modulus of elasticity versus temperature for polycrystalline Al_2O_3 [54], Rene N4 [41], and CODEP coating [41].

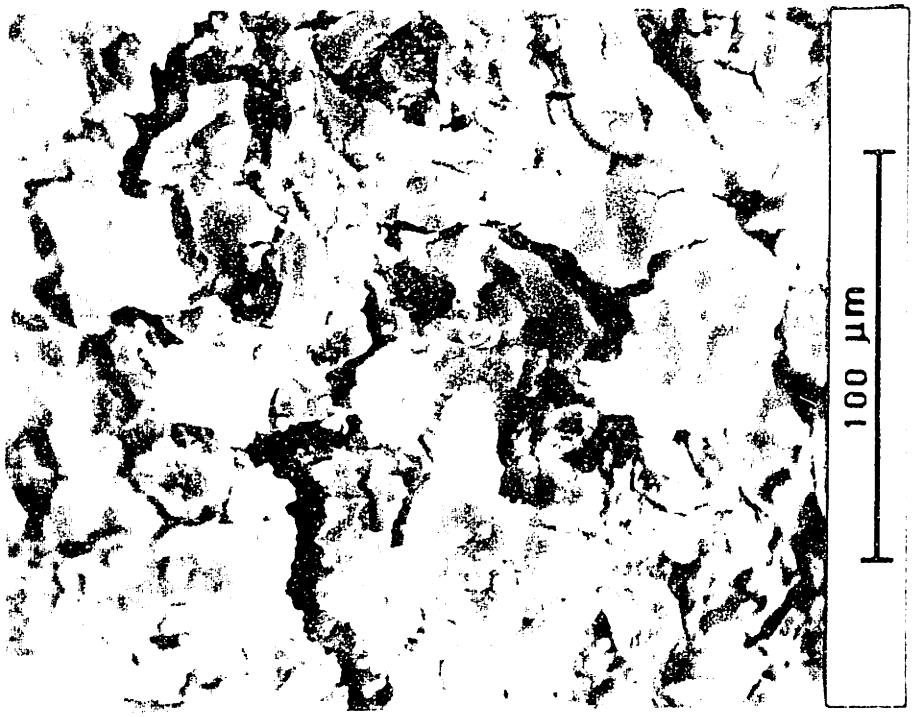

(a) <100> periphery

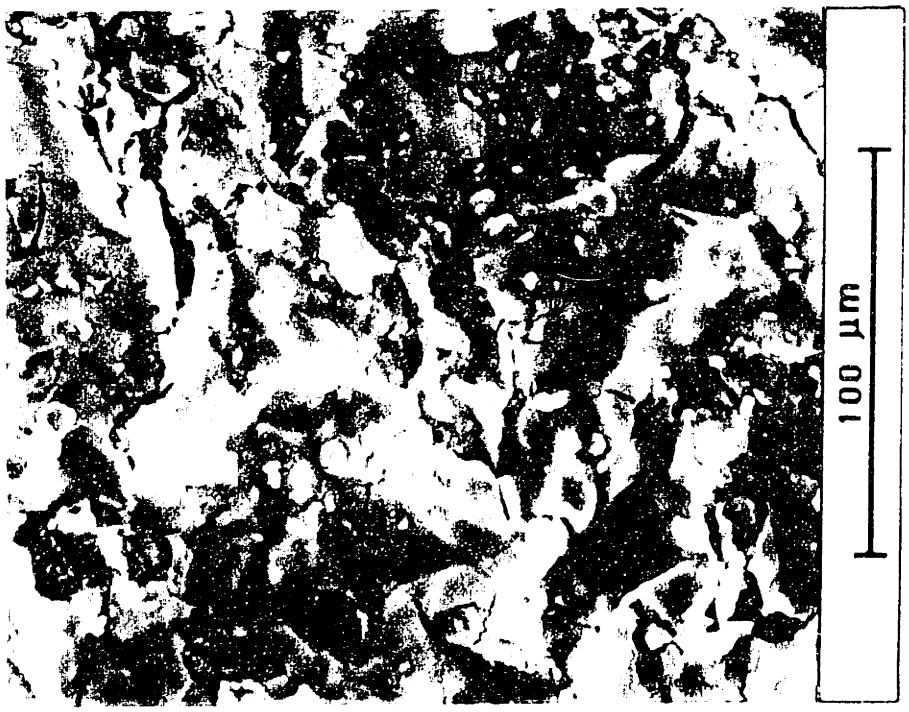

(b) <110> periphery

Fig. 20 SEM micrographs of surface oxide after 6000 cycles of moderate 8s heating and 30s cooling (the corresponding coating degradation is given in Figs. 11c-d and 15c-d). The micrographs were taken normal to the radial specimen direction, with the circumferential periphery strain acting horizontal in the plane of the micrographs.

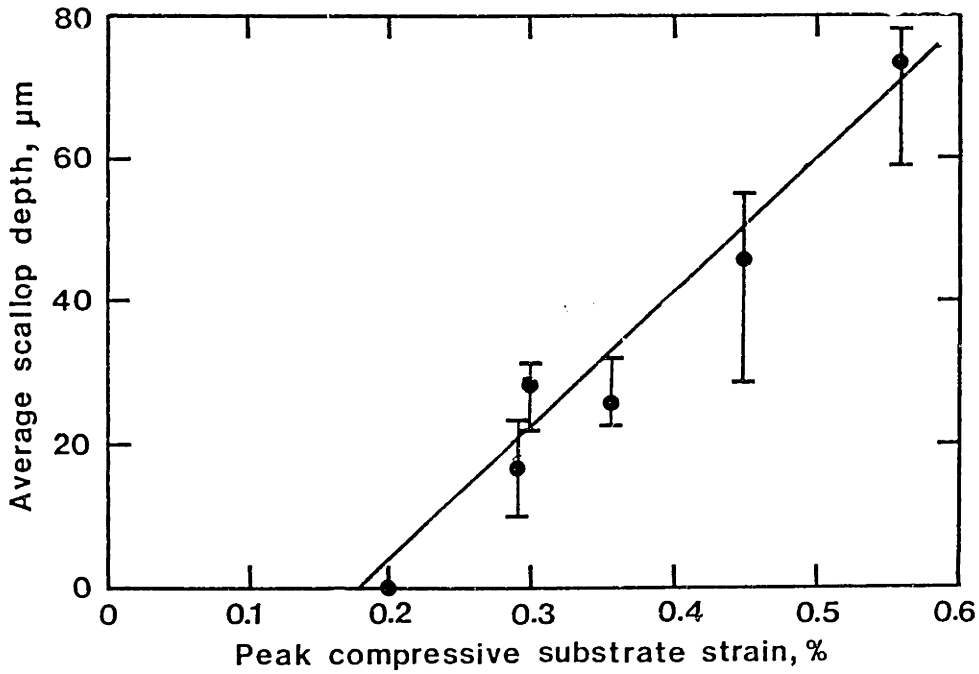

Fig. 21a Average scallop depth versus peak compressive substrate strain (≈ peak compressive coating strain). Vertical bars give range of scallop depths observed. Data summarized in Table 4.

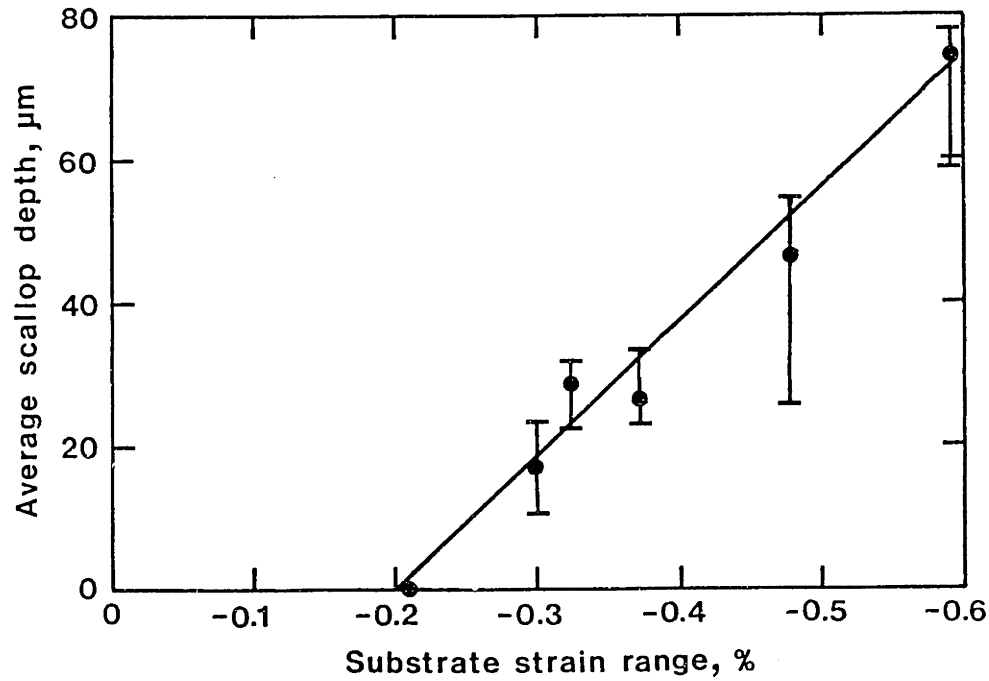

Fig. 21b Average scallop depth versus substrate strain-range (≈ coating strain-range). Vertical bars give range of scallop depths observed. Data summarized in Table 4.

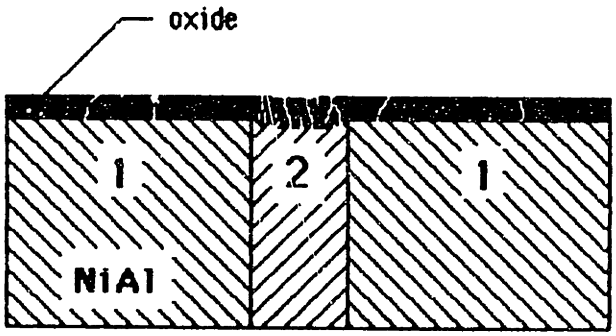

(a) Surface roughening due to repeated oxide breakdown produces an area difference between adjacent coating regions (elements 1 and 2).

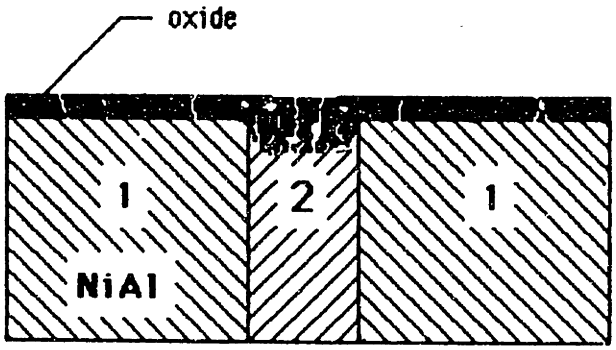

(b) Due to the Bauschinger component of primary creep, cyclic coating strains will further increase the strain in element 2 relative to element 1. This strain difference increases the area difference between elements. The magnitude of the area difference depends upon strain amplitude and the number of strain cycles.

Fig. 22 Schematic illustration of scallop growth by kinematically irreversible cyclic creep. This mechanism is consistent with the correlation of scallop depth with coating strain amplitude (see Fig. 21b)

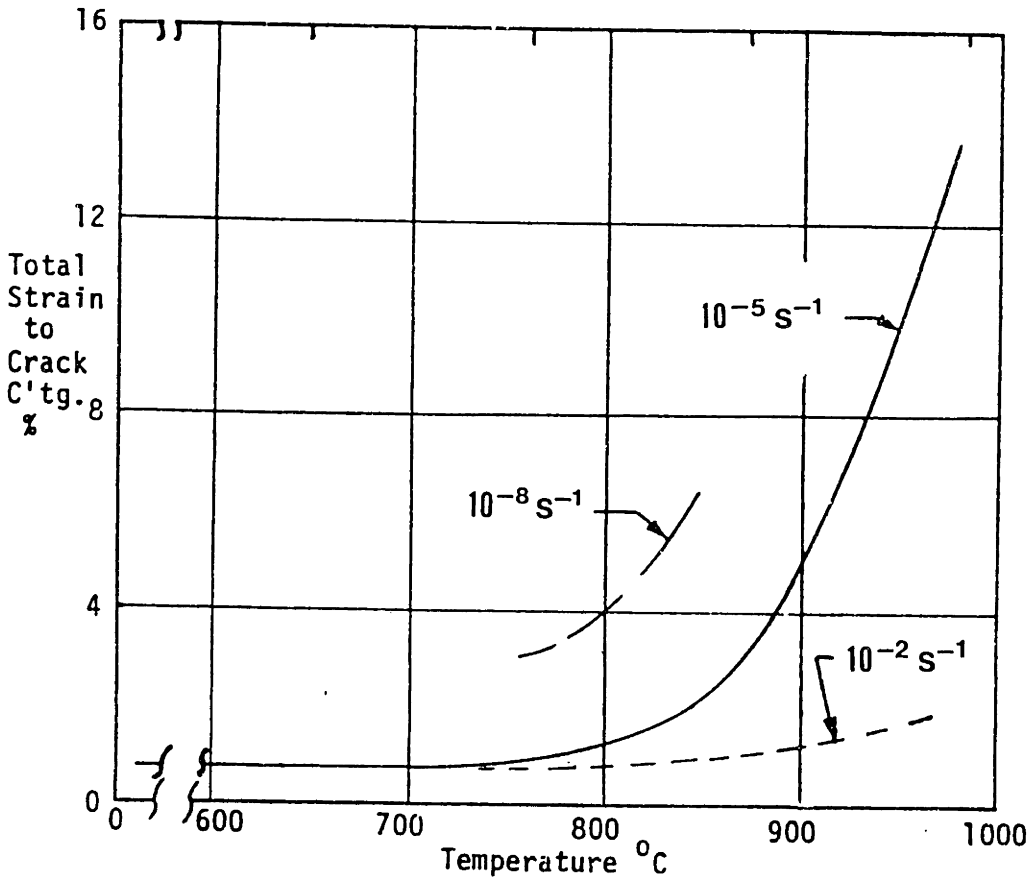

Fig. 23 Strain to cracking versus temperature for Codep B-1 coating applied to Rene 125. From Kaufman [42].

Chapter 4

Effect of Simultaneous Hot-Corrosion and Thermal Fatigue on Aluminide Coating Durability

Abstract

This Chapter describes the use of induction heating of stepped-disk specimens to study the effect of substrate strain history on the corrosive (Na_2SO_4-SO_2-O_2) attack of aluminide coated Rene N4.

The degradation of the coating was found to be strongly dependent upon the strain history of the aluminide coating. The coating was degraded to 40% of its original thickness by formation of Al-Cr-Ni sulfides after 6000 cycles between strains of -0.26% at 925^{0}C and 0.03% at 650^{0}C. Only minor degradation was observed for 6000 cycles between strains of -0.16% at 925^{0}C and 0.01% at 790^{0}C.

A mechanism to explain the acceleration in corrosive attack with thermal cycling is proposed. The mechanism assumes that oxide breakdown due to thermal cycling results in direct contact between the molten Na_2SO_4 and the aluminide coating, resulting in an increase in oxygen ion activity, which promotes basic fluxing of Al_2O_3.

Introduction

A common feature of the combustion of petroleum fuels is the formation of Na_2SO_4 by the reaction

$$2NaCl(v) + SO_2(v) + (1/2)O_2(v) + H_2O(v) = Na_2SO_4(v) + 2HCl(v). \quad (1)$$

Stearns et al [56], using free-jet sampling mass spectrometry of combustion flames, have observed that Na_2SO_4 typically forms in less than 1 ms, which compares with typical combustion gas residence-times in a turbine of 5-10 ms [57]. Thus, as sea air typically contains 0.01 ppm NaCl [58], the direct formation of Na_2SO_4 in a turbine by Eq. 1 is certainly possible. Na_2SO_4 can also be supplied directly by sea water, which contains about 2600 ppm of this salt.

In the first-stage of an advanced gas turbine, the combustion gas stream typically reaches a temperature in excess of 1300^{0}C, with airfoil temperatures in the range of 1000 - 1100^{0}C. Thus, as discussed in Chapter 1, in the first-stage of a gas turbine, Na_2SO_4 formed by combustion exists in the vapor state and condensation of Na_2SO_4 onto airfoils is not observed. However, the combustion gases expand and cool as they pass through the turbine stages, with the result that airfoil temperatures in the second or third-stage of a turbine rarely exceed 950^{0}C. The lower-stage airfoil temperatures are below the dew-point of

Na_2SO_4, which promotes the condensation of Na_2SO_4 onto the airfoils. After condensation of Na_2SO_4, rapid sulfidation of Ni-based coatings and substrates can occur [9, 59-64].

Over the past 20 years many techniques have been developed to study the Na_2SO_4 induced corrosion (hot-corrosion) of turbine airfoils. These techniques include gas-burner rigs, furnace tests and crucible tests.

In ***burner-rigs*** [3, 65-68] specimens are exposed to high velocity combustion gases produced by burning jet fuel (see Fig. 24). Although burner-rigs can simulate the combustion gas composition existing in a turbine their use has come under considerable debate lately due to the wide differences in test results obtained by different laboratories [3,69]. This typical variation in test results is clearly shown in the results of an ASTM round-robin test, Fig. 25. The principal reason for the variation in test results, which occurs even among rigs which burn the same fuel, can be attributed to the variation in specimen strain history resulting from the use of various specimen geometries (e.g., wedges, squares, circular pins) and burner-rig velocities. Due to the complex coupled heat-transfer analysis required for the determination of specimen strain history, rarely, if ever, is the strain history of the test specimens determined. This makes the transfer of test results to actual gas turbines empirical at best.

In the frequently used ***furnace test*** [6,8, 70-72] cylindrical specimens are coated with a thin layer of Na_2SO_4 and heated in the presence of a simulated combustion gas (typically SO_2-SO_3-O_2). Although inexpensive, these tests are unable to simulate the temperature and strain histories experienced by turbine airfoils.

In ***crucible tests*** [73-75] a specimen is partially or totally immersed in molten sulfates. In general, poor correlation exists between crucible test results and actual in-service performance of a particular alloy or coating [73]. This is most likely attributable to the unrealistically low values of oxygen pressure in the vicinity of specimens contained in deep static melts, compared to the higher oxygen activity that would be expected across the thin Na_2SO_4 layer formed on turbine blades. This low oxygen pressure results in an increase in sulfur activity at the specimen surface, with a correspondingly rapid rate of sulfidation attack.

In view of the limitations of the test techniques discussed above, this chapter describes the use of induction heating of thin disk-specimens as an alternative. Induction heating, which was described in detail in Chapter 2 for testing in air environments, allows close control of specimen temperature and strain history and is easily modified for corrosive atmosphere testing. To illustrate the use of induction heating in corrosion studies, the effect of substrate strain history on the corrosive attack of

aluminide coated Rene N4 is examined.

Experimental Technique

Specimen geometry, substrate composition and aluminide coatng. As discussed in detail in Chapter 2, 17 mm diameter stepped-disk specimens were machined from a monocrystal rod of Rene N4 such that their faces were normal to the [100] crystal growth direction (Fig. 3) The composition of the Rene N4 and details of the specimen heat treatment and aluminization process are given in Chapter 2.

Test apparatus. The induction heating apparatus described in Chapter 2 was modified for corrosive atmosphere containment by insertion of a 22 mm diameter quartz tube between the induction-coil and specimen (see Fig. 26). The quartz tube precludes the use of cooling manifolds (Figs. 4,5) to obtain additional tension in the specimen periphery during cooldown. *However,* in view of the slow cooling rates of third stage airfoils (typically 930 to 450^{0}C in 10 to 30s versus 1080 to 500^{0}C in 4 to 15 s for first stage airfoils) this is not considered a serious limitation to the test technique. In addition, the tests performed in air (Chapter 3) showed that coating compression developed during heatup can be as damaging to coating life as tension produced on cooldown (compare Figs. 11a-h).

Specimens are positioned in the induction coil by a 304 stainless steel support-rod attached to the exhaust manifold (Fig.

26). This 6 mm diameter support-rod also serves as a heat-sink to aid in maintaining a temperature gradient between the specimen periphery and core.

Specimen temperature was monitored and controlled by two 0.20 mm diameter Pt/Pt-10%Rh thermocouples attached to the specimen at a radius of 6.5 mm. To calibrate the control thermocouple for the particular temperature history used (Fig. 27) and to obtain the temperature data required in the finite-element analysis for specimen stress-strain history, a specimen with 0.13 mm diameter chromel-alumel thermocouples positioned at specimen radii of 3.5, 4.0, 5.0, 6.0, 6.5, and 8.3 mm were used (additional details concerning thermocouple attachement and accuracy of temperature measurement are given in Chapter 2). To simulate the conditions used during an actual corrosion test, argon at a flow rate of 100 cm^3/min was passed through the apparatus. The gas was heated in the hot-zone to the corrosion test temperature of 930^{0}C.

After calibration of the control thermocouple, all subsequent testing was performed using only the two Pt/Pt-10%Rh thermocouples.

Test atmosphere. The simultaneous thermal fatigue and hot-corrosion tests involved coating the specimen periphery with 1.0 mg/cm^2 Na_2SO_4 and flowing an 20%O_2-0.10%SO_2-bal. argon

gas mixture through the quartz tube isolating the specimen from the induction-coil.

The Na_2SO_4 was applied by rotating the specimen on a mandrel at 200 RPM and heating the specimen to 200^{0}C over a hot-plate. An airbrush was then used to spray a metered quantity of an aqueous sodium sulfate solution to the entire periphery step (the specimen core was protected from overspray by use of thin foil disks). Specimens were weighed before and after spraying to verify the quantity of Na_2SO_4 applied to the periphery step.

During preliminary corrosion tests it was observed that after thermal cycling the Na_2SO_4 applied to the periphery step migrated towards the specimen core. This was most likely caused by surface tension effects, which were accentuated by the smooth specimen finish and curvature of the periphery. To alleviate this problem, specimens were pre-oxidised to provide a rougher surface. The oxidation was performed by rotating Na_2SO_4-coated specimens at 1700 RPM, while heating in a refractory furnace at 930^{0}C for a period of 10 hr. The rapid rotation of the specimens was necessary to overcome the surface tension of Na_2SO_4, ensuring its even distribution along the periphery. The surface oxide formed by this isothermal treatment was found to "peg" the Na_2SO_4 along the periphery step. This was verified by examining the periphery step while thermally cycling a specimen between 450 and 930^{0}C in the induction-heating apparatus. It was observed that above the melting point of Na_2SO_4 the entire

periphery step was covered with a thin layer of molten Na_2SO_4, with no migration observed during the thermal cycling.

The gas composition was chosen to simulate roughly the mole fractions of SO_2 and O_2 present in the third-stage of a gas-turbine operating under 90% power conditions in a marine atmosphere (10^{-4} to 10^{-6} SO_2, 0.15-0.20 O_2). To obtain the desired gas composition the gases SO_2, O_2, and argon were mixed in a 3-tube gas-mixer prior to entering the quartz tube. For greater accuracy in the gas metering and mixing, the SO_2 was obtained as an 0.1%SO_2-bal. argon mixture, which allowed using a higher flow rate for a given concentration of SO_2. On a volumetric basis, the composition of the gas mixture prior to entering the quartz tube was: 20.00% O_2, 0.010% SO_2, 79.99% argon. After entering the quartz tube the gas-mixture passed through a 250 mm long hot-zone, where it was heated to the test temperature of 930^{0}C[1]. To aid in establishment of equilibrium at 930^{0}C, a platinum catalyst (6 grams of 80 mesh Pt-screen) was placed in the furnace hot-zone. Assuming complete equilibrium[2], the composition of the gas exiting the hot-zone (at 930^{0}C) was: 0.0089% SO_2, 0.0011% SO_3, 20.00% O_2, 79.99% argon (see Appendix C).

---

[1]This gas temperature was maintained 10mm from the specimen surface (measured with a shielded thermocouple).

[2]For a flow rate of 100 cm^3/min, the average gas velocity in the quartz tube (cross-sectional area = 2.8 cm^2) is 0.03 cm/s. This gives an average time in the hot-zone of 800 seconds, which is more than adequate for establishment of equilibrium [76].

Isothermal corrosion tests

To provide a reference to compare with the corrosion obtained with thermal cycling, isothermal corrosion tests were carried out by placing the Na_2SO_4-coated test specimen in the test apparatus and heating in the SO_2-O_2 atmosphere to 930°C, for times of 100 and 200 hours.

Cyclic corrosion tests. To determine the effect of cyclic thermal strains on the corrosion process, heating and cooling rates representative of those encountered by third-stage blades and vanes during takeoff and landing of a jet-helicopter were chosen: 450 to 930°C in 8s, followed by a 60s hold at 930°C, followed by cooling to 930°C in 30s (see Fig. 27). The substrate stress-strain history corresponding to this temperature history was determined by a thermoelastic analysis and is shown in Fig. 28 (details of a similar thermoelastic analysis are given in Chapter 2). The cyclic corrosion tests were performed for 3000 and 6000 cycles.

Results and Discussion

After completion of testing, the surface scales formed on the specimens were analyzed. After this preliminary analysis, specimens were cut in half along a <110> orientation and one of the halves was Ni-plated and cold-mounted in epoxy; the other half stored for additional later analysis of the surface scale. The mounted specimen was next ground and polished to its mid-plane

in preparation for microprobe-analysis.

Isothermal corrosion. As shown in the <100> micrograph of Fig. 29, no visible corrosive attack of the coating has occurred. The approximately 1 μm thick black band formed along the coating surface was identified as stiochiometric Al_2O_3.

Microprobe analysis[3] of the outer coating matrix (analysis Points a-d) showed that the Al-equivalent (Al+Ti+Ta+Mo) had dropped from 49 at% as-coated, to approximately 43 at% after 100 hr at 930°C and 40 at% after 200 hr at 930°C. No sulfur was identified in the coating matrix (resolution for sulfur ≈0.5 at%).

Cyclic corrosion tests. Along the <110> peripheries, with strains of -0.16% at 925°C to 0.01% at 790°C, there was only minor corrosion after 3000 and 6000 cycles (see Figs. 30a,b). Along the <100> peripheries, however, with strains of -0.26% at 925°C to 0.03% at 650°C, coating attack to 70% of the original coating thickness has occurred after 3000 cycles with attack extending to 30% of original coating thickness after 6000 cycles (see Figs. 30c,d).

Microprobe analysis of the coating matrix along <100> peripheries showed essentially the same composition as obtained

---

[3]See Chapter 3 for details of microprobe parameters used in a similar analysis of the coating matrix.

with isothermal exposure. No sulfur was detected along these orientations. Microprobe analysis of the coating matrix along <100> peripheries showed the presence of Al sulfides (analysis Point 1), typically occurring at the corrosion fronts. (Identification of coating grain boundaries is made difficult by the extensive corrosion attack.)

Discussion. The stability diagram of Fig. 31 shows the gas compositions and oxygen ion activity for which Al_2O_3 is stable beneath Na_2SO_4 at 930°C. For the gas composition used in this study (Fig. 31, Point 1), Al_2O_3 should be stable beneath a Na_2SO_4 melt at 930°C and 1 atmosphere total pressure. Thus, direct fluxing of the Al_2O_3 should not occur, which is consistent with the lack of corrosive attack observed in the isothermal tests. Thus, as discussed below, it appears that another mechanism, driven by coating strains, is responsible for the corrosive coating attack observed along the <100> substrate orientations.

Proposed mechanism for the acceleration of hot-corrosion attack by thermal fatigue. To explain the extensive coating degradation observed along the high strain <100> periphery orientations it is proposed that thermally induced strains can crack an otherwise protective Al_2O_3 layer, exposing the coating directly to molten Na_2SO_4, as illustrated schematically in Fig. 32. This direct exposure would lower the O^{2-} concentration by the

reaction:

$$\frac{2}{3}Al_2 + SO_4^{2-} = O^{2-} + \frac{1}{3}Al_2S_3 + \frac{3}{2}O_2 \qquad (2)$$

As the dashed path on the stability diagram of Fig. 31 shows, this increase in $a_{O^{2-}}$ obtained by this reaction can promote basic fluxing of Al_2O_3.

To verify this mechanism, the specimen halves from the cyclic tests (3000 and 6000 cycles) that still had undisturbed corrosion scales were cut into 10^0 sectors along the <100> and <110> periphery directions. The water soluble corrosion products on these sectors were then analyzed. These analyses clearly showed Al in the leach water from the <100> peripheries, with only trace amounts detected along <110> peripheries. In a similar analysis of water soluble products obtained from the isothermally exposed specimens, only Na and S were detected.

Conclusions

1. Induction heating of stepped-disk specimens offers an alternative to the use of gas-burner rigs and furnace testing in hot-corrosion studies. The technique has the advantage of allowing close control over specimen temperature and strain history, and corrosive atmosphere.

2. Hot-corrosion attack of aluminide coated Rene N4 was

strongly dependent upon coating strain history. After 6000 cycles between strains of -0.26% at 925^{0}C and 0.03% at 540^{0}C the coating was penetrated by sulfides to the substrate. Only minor degradation was observed for 6000 cycles between strains of -0.16% at 930^{0}C and 0.01% at 540^{0}C.

3. A mechanism has been proposed to explain the acceleration of hot-corrosion attack by coating strains. This mechanism assumes oxide breakdown caused by thermal cycling results in direct interaction between the aluminide and molten Na_2SO_4. This direct interaction increases the oxygen ion activity at the coating/oxide interface and promotes basic fluxing of Al_2O_3.

The feasibility of the mechanism was verified by identification of aluminum sulfides in the corrosion scale, which are predicted by the proposed mechanism.

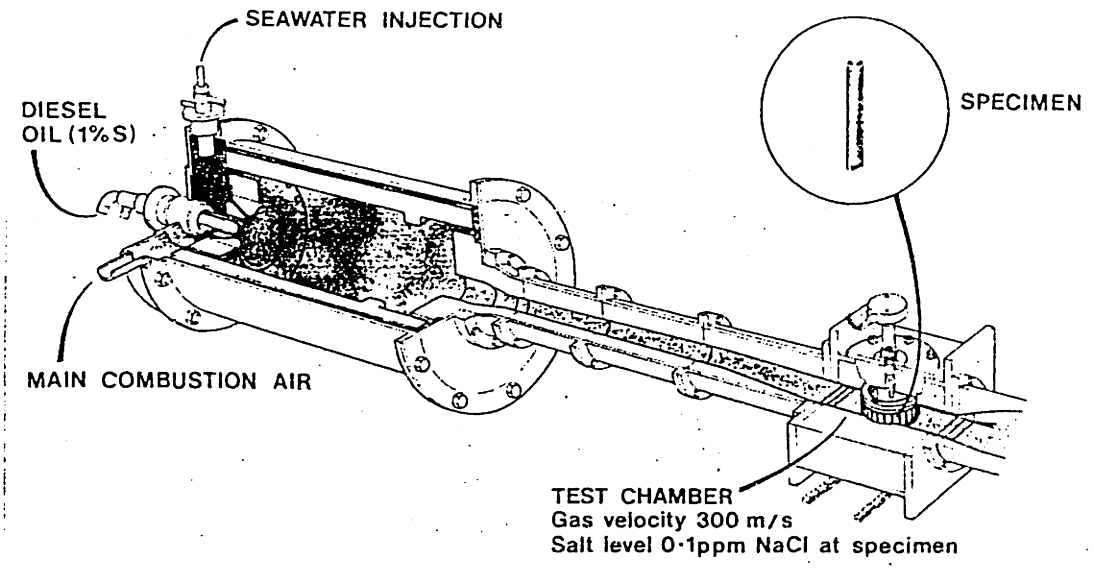

Fig. 24 Typical gas-burner rig used to study hot-corrosion of coated alloys. From Conde et al [64].

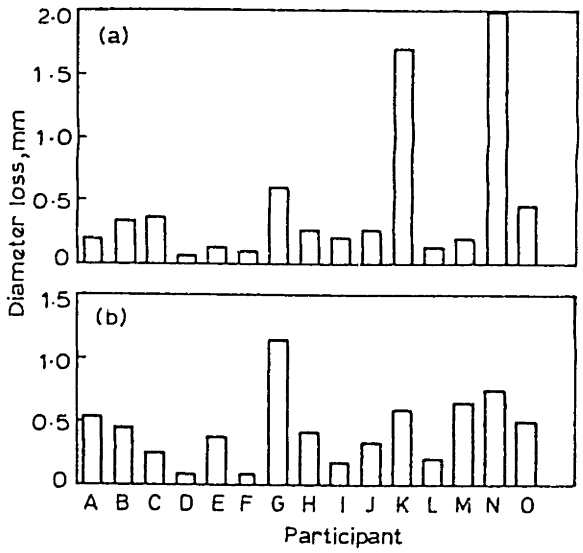

a Udimet 500; *b* IN 738

Fig. 25 Results of ASTM Round Robin test program to determine the variability in corrosion rates obtained with gas-burner rigs [69]. The test program involved measurement of the diameter loss obtained with cylindrical specimens of Udimet 500 and IN 738 exposed for 200 hours in the various burner rigs.

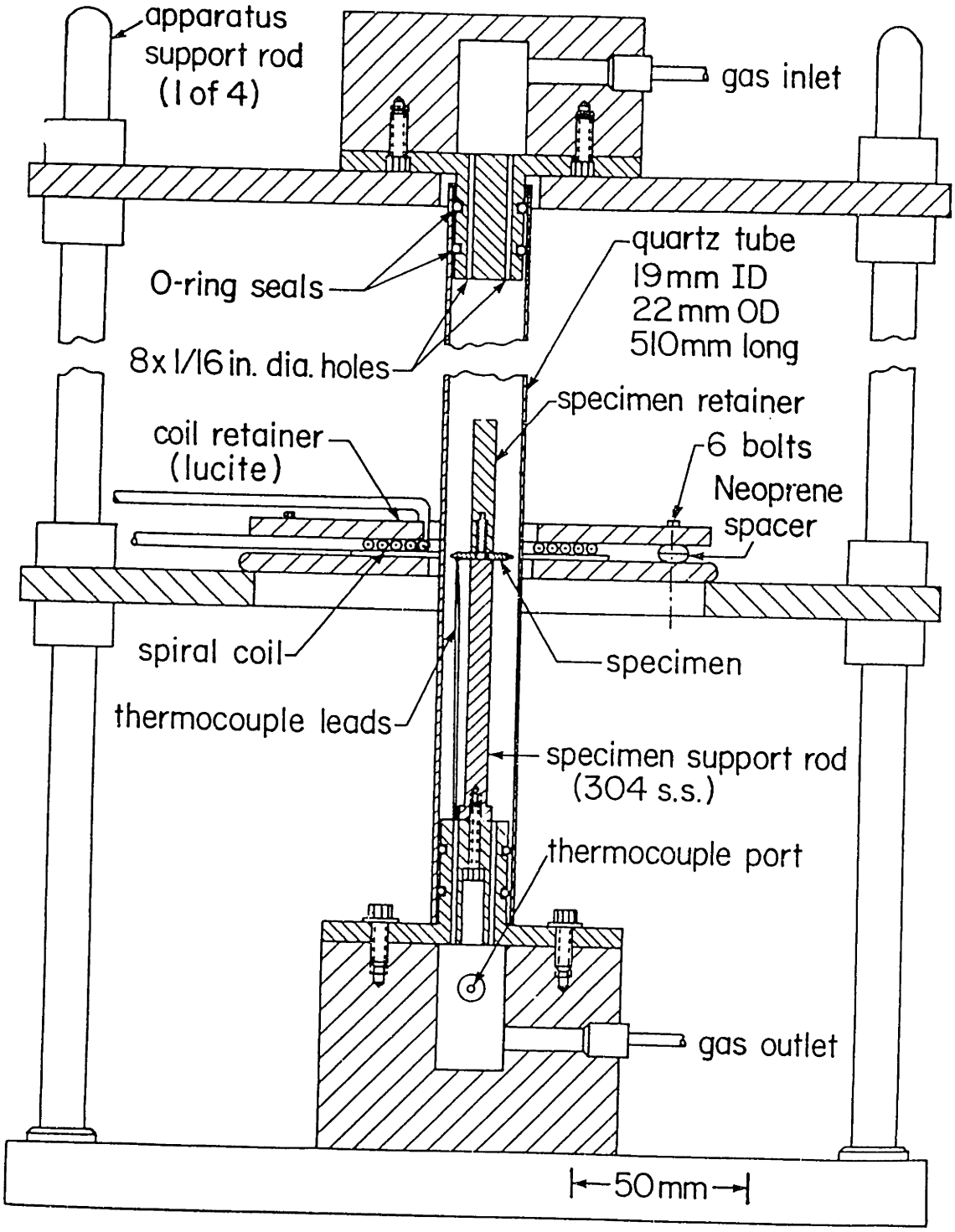

Fig. 26 Experimental apparatus used to study simultaneous thermal fatigue and hot-corrosion.

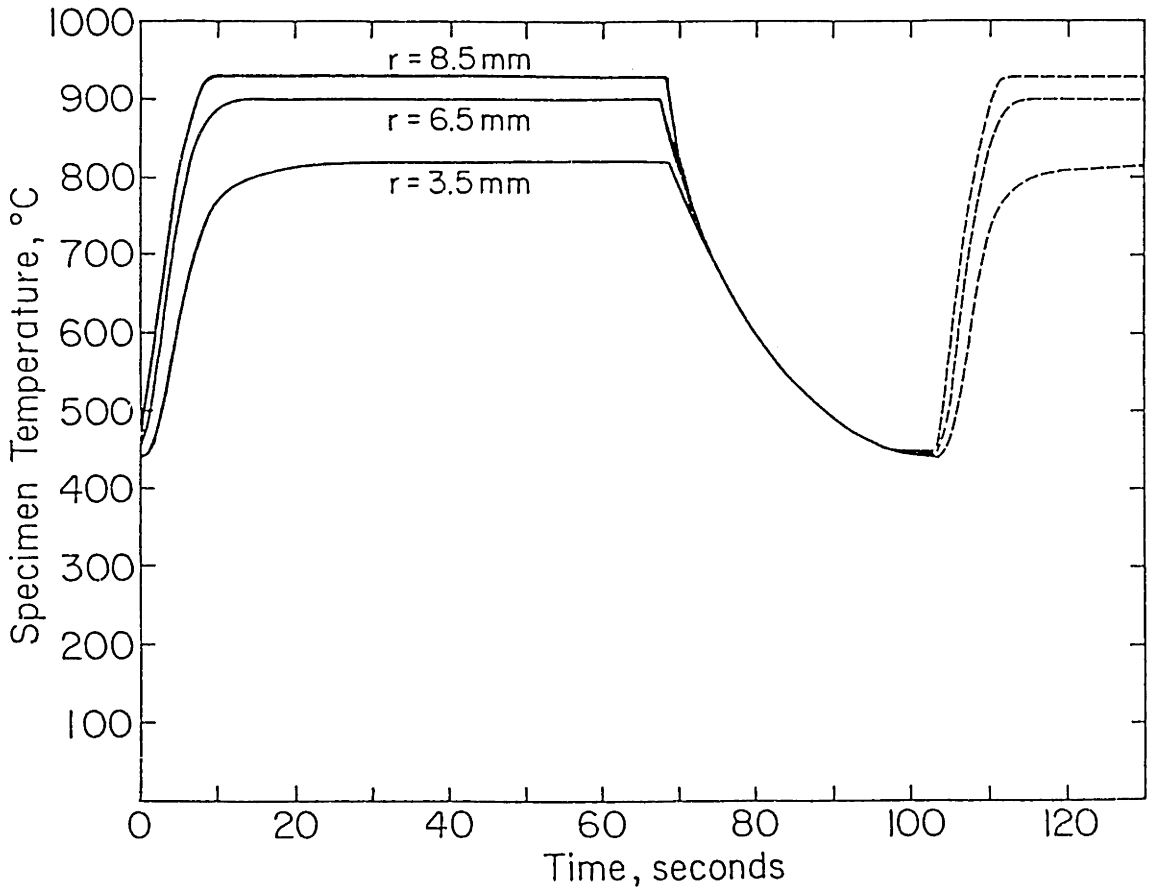

Fig. 27 Temperature history of stepped-disk specimens used to study the effect of thermal strains on aluminide coating degradation in a corrosive Na_2SO_4-SO_2-O_2 atmosphere.

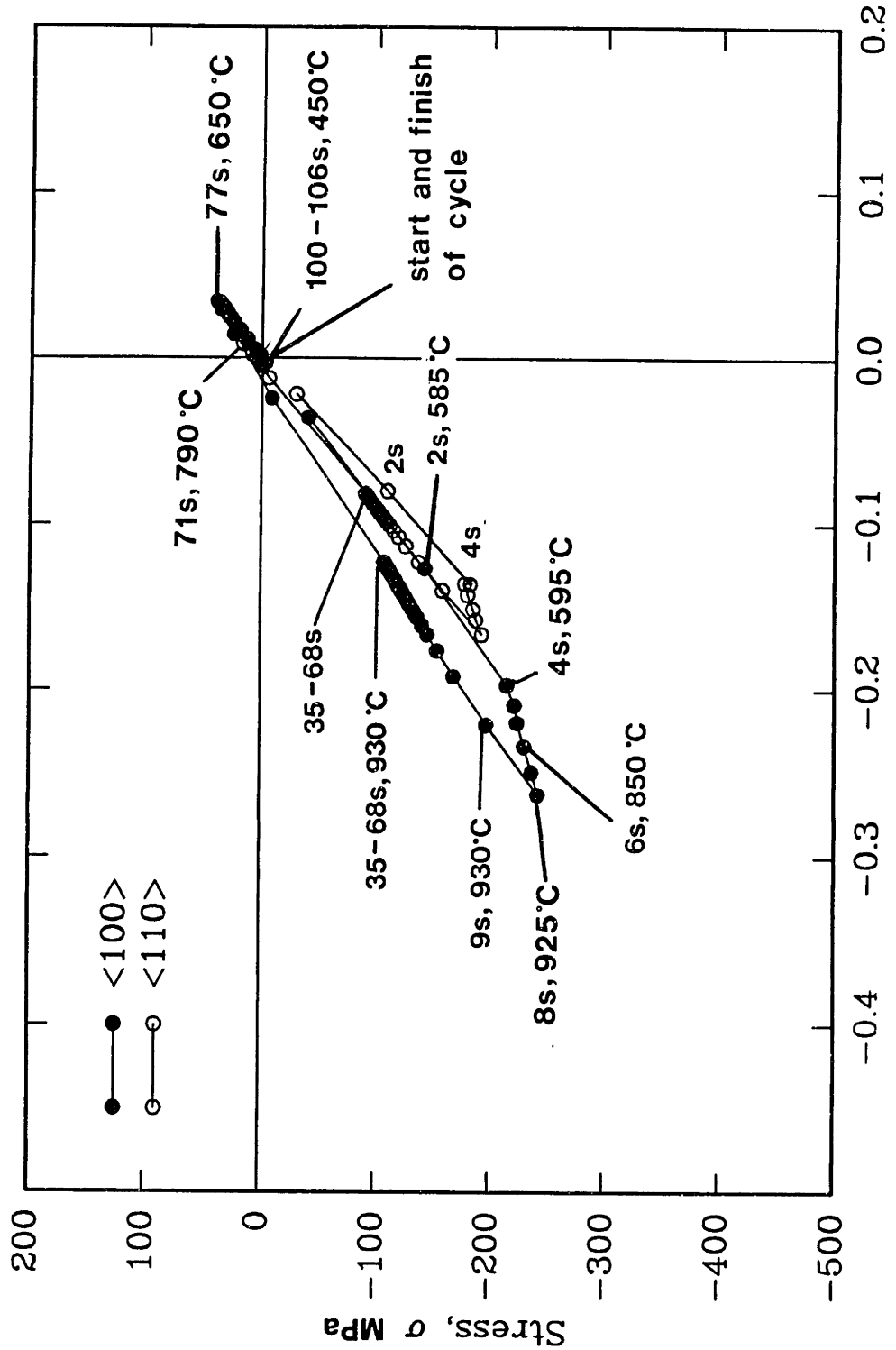

Fig. 28 Circumferential stress-strain history of <100> and <110> periphery orientations. Determined by a thermoelastic finite-element analysis for the temperature history of Fig. 27: 450 to 930°C in 9s + 60s hold at 930°C, followed by cooling to 450°C in 30s.

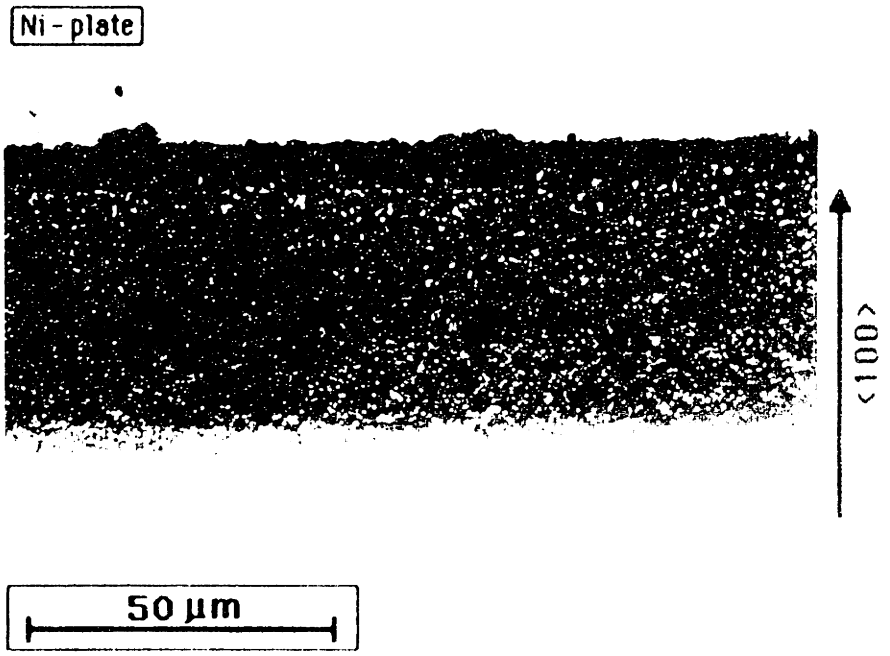

(a) 100 hr at 930°C

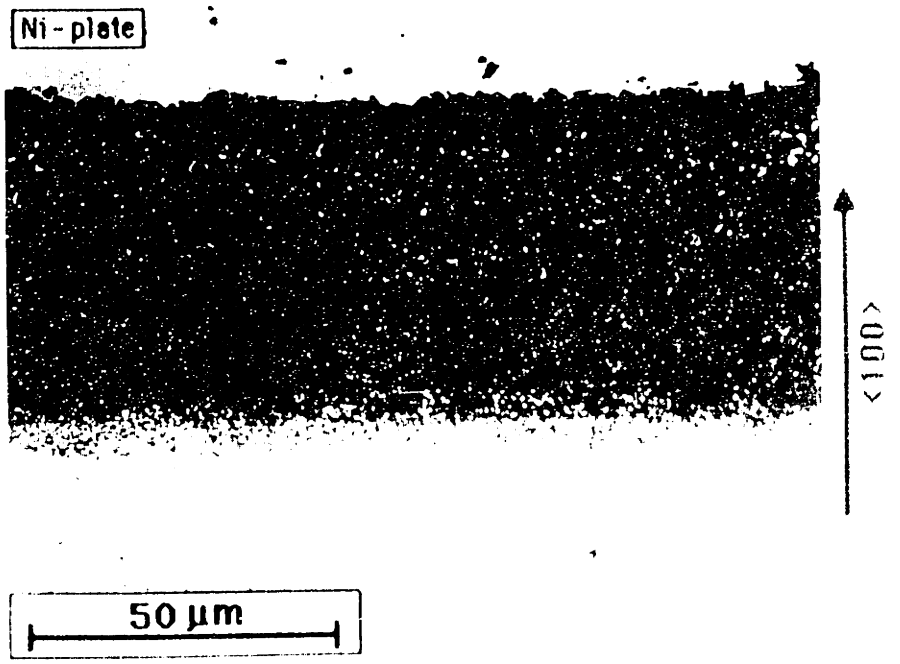

(b) 200 hr at 930°C

Fig. 29a,b Backscattered electron micrographs of aluminide coating after 100 and 200 hr at 930°C. Na_2SO_4-SO_2-SO_3-O_2 environment.

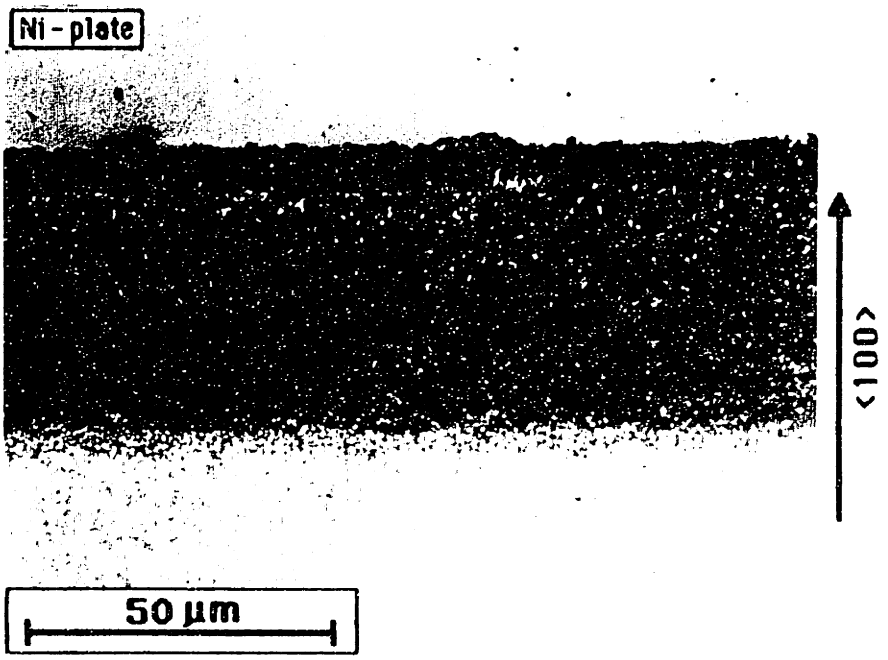

(a) 100 hr at 930°C

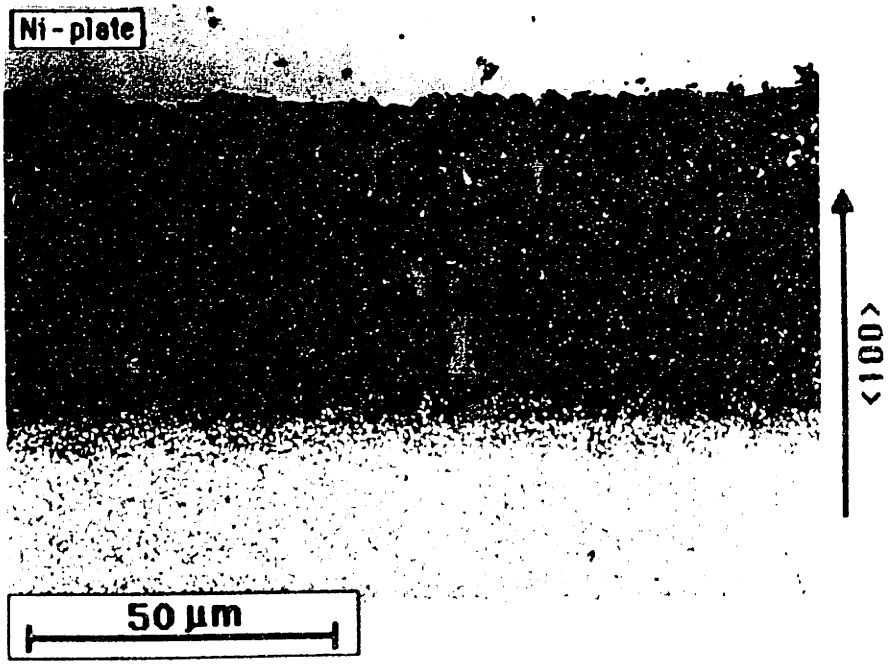

(b) 200 hr at 930°C

Fig. 29a,b Backscattered electron micrographs of aluminide coating after 100 and 200 hr at 930°C. Na_2SO_4-SO_2-SO_3-O_2 environment.

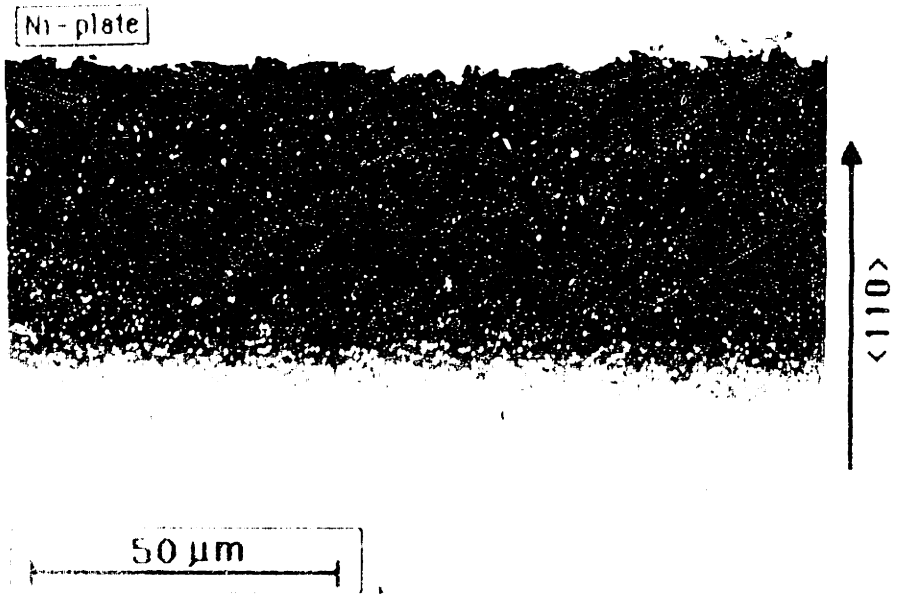

(a) 3000 cycles

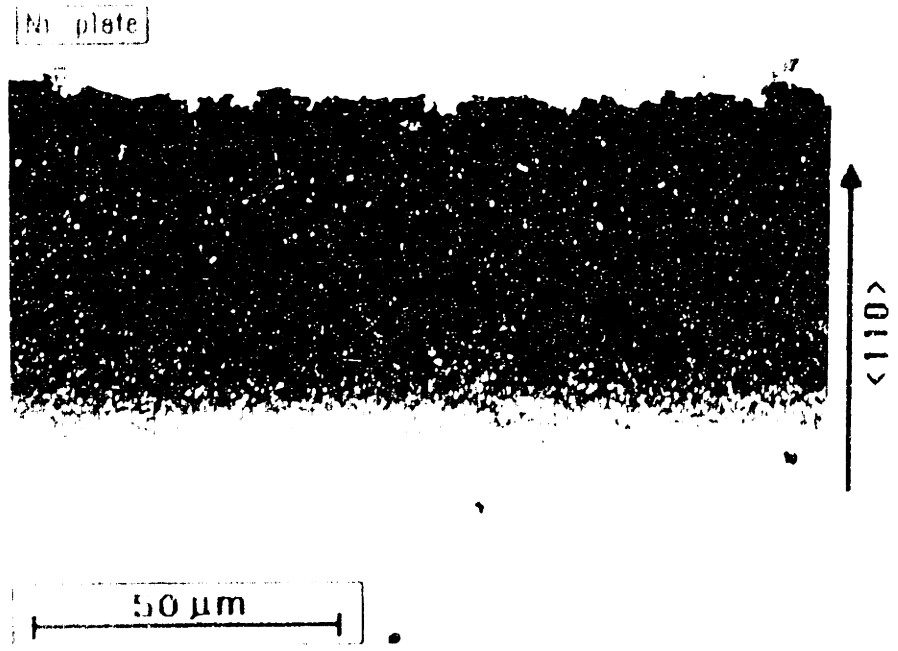

(b) 6000 cycles

Fig. 30a,b Backscattered electron micrographs of aluminide coating after 3000 and 6000 cycles between strains of -0.16% and 0.01%. Na_2SO_4-SO_2-SO_3-O_2 environment, <110> periphery direction.

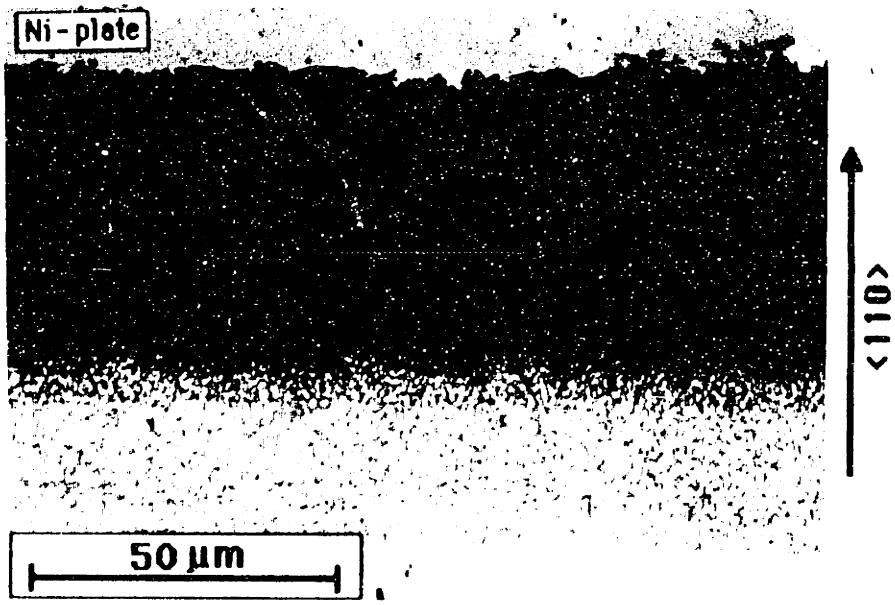

(a) 3000 cycles

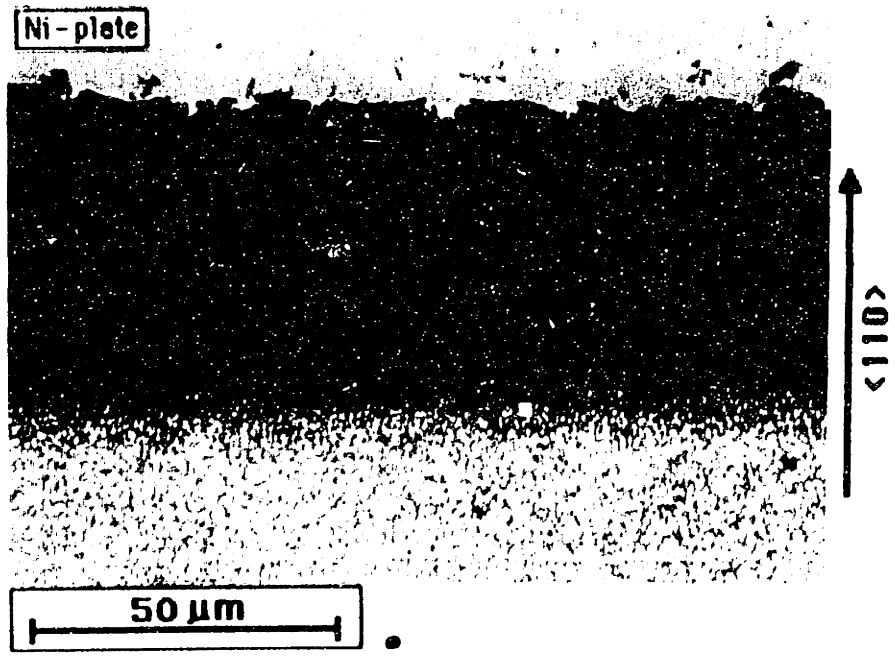

(b) 6000 cycles

Fig. 30a,b Backscattered electron micrographs of aluminide coating after 3000 and 6000 cycles between strains of -0.16% and 0.01%. Na_2SO_4-SO_2-SO_3-O_2 environment, <110> periphery direction.

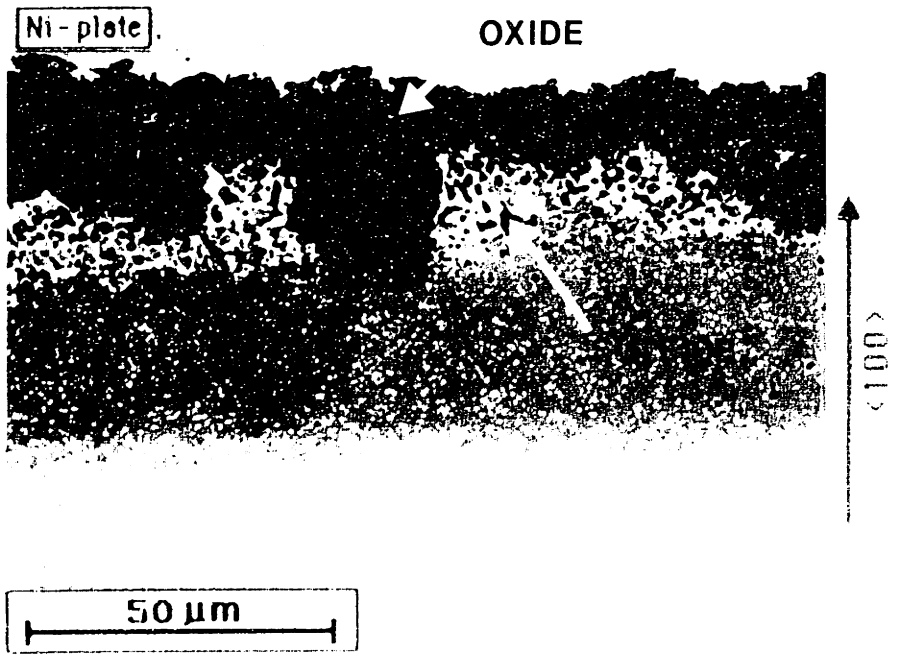

(c) 3000 cycles

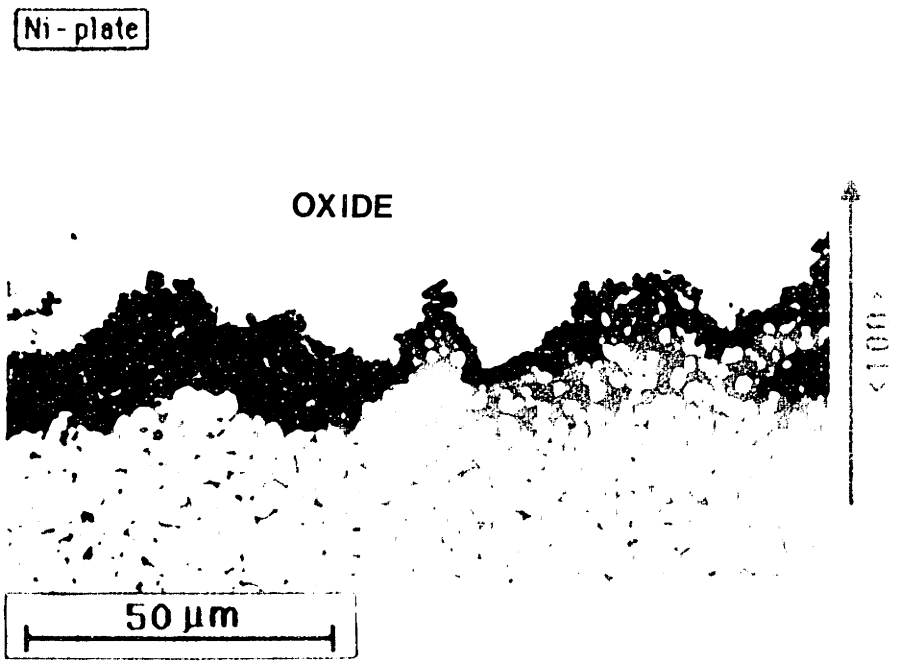

(d) 6000 cycles

Fig. 30c,d Backscattered electron micrographs of aluminide coating after 3000 and 6000 cycles between strains of -0.26% and 0.03% Na_2SO_4-SO_2-SO_3-O_2 environment, <100> periphery direction

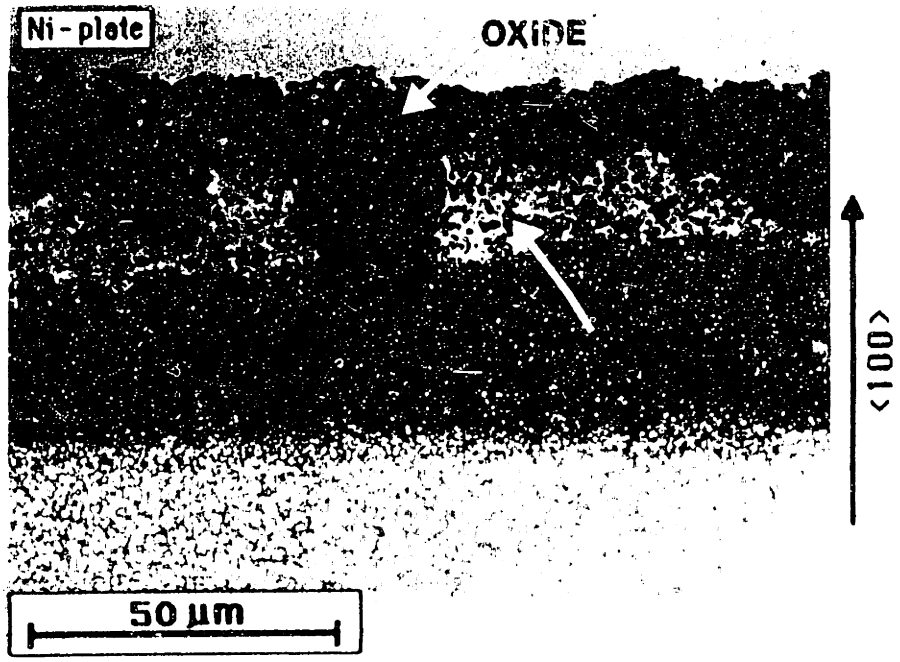

(c) 3000 cycles

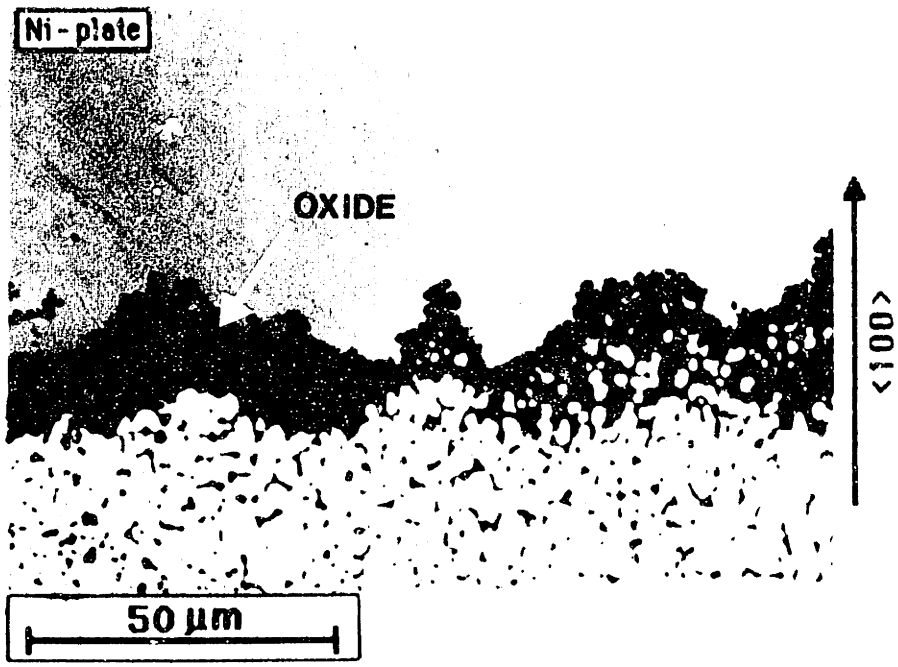

(d) 6000 cycles

Fig. 30c,d Backscattered electron micrographs of aluminide coating after 3000 and 6000 cycles between strains of -0.26% and 0.03%. Na_2SO_4-SO_2-SO_3-O_2 environment, <100> periphery direction.

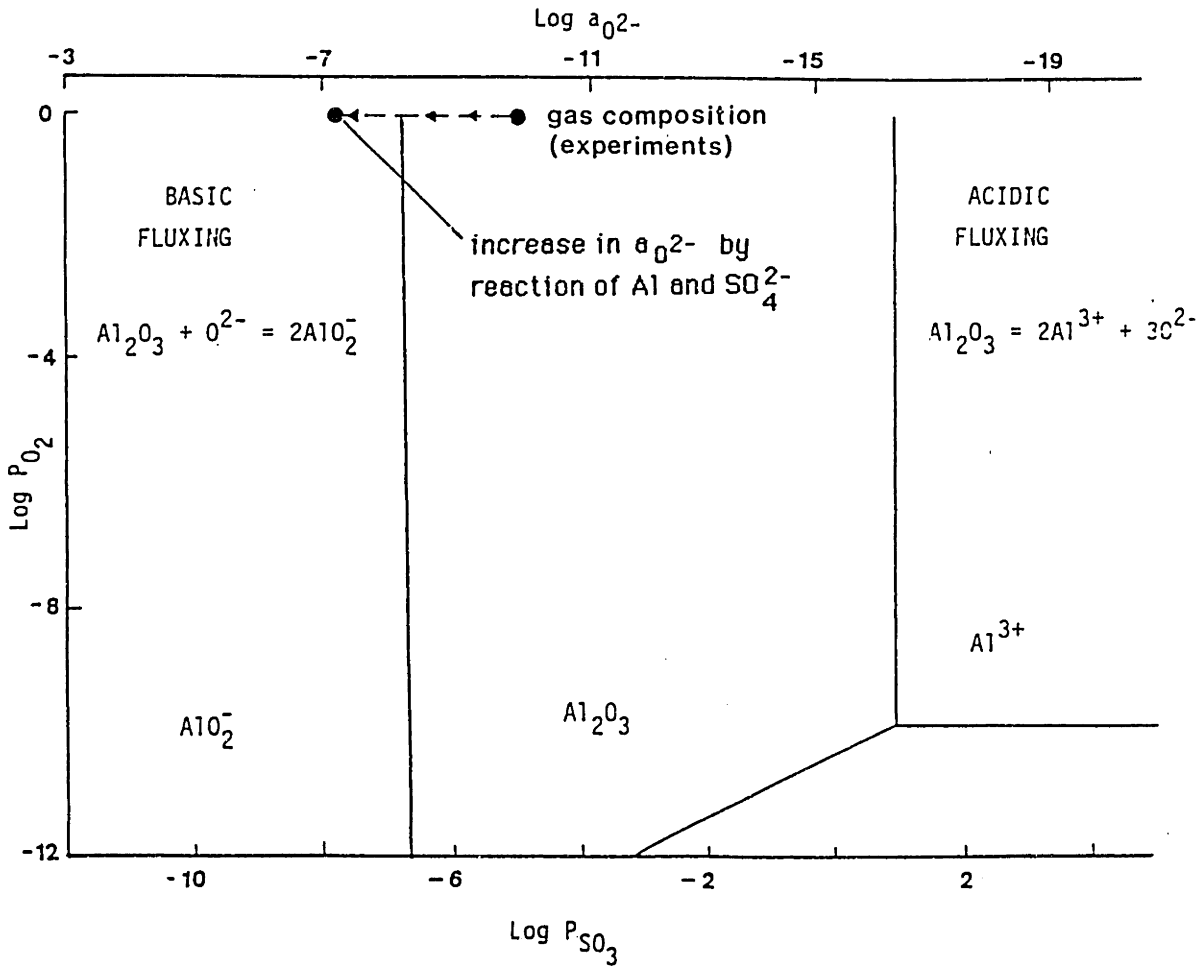

Fig. 31 Stability diagram showing phases of Al that are stable in Na_2SO_4 at 930°C.

For 0.0089 %SO_2 - 20.0 %O_2 - 0.0011 %SO_3 - Bal. Argon, Al_2O_3 is stable beneath Na_2SO_4 at 930 °C:

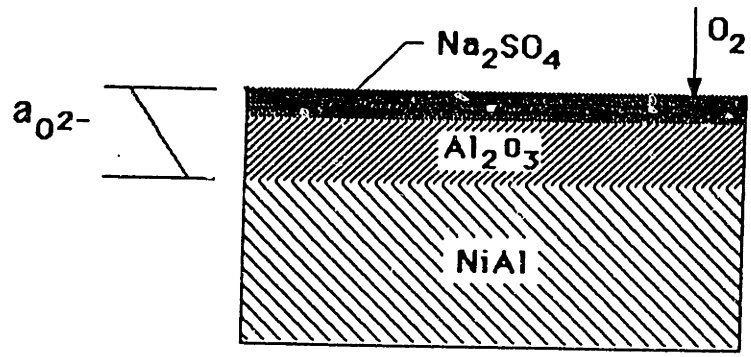

However, thermal strains can result in oxide cracking or spalling:

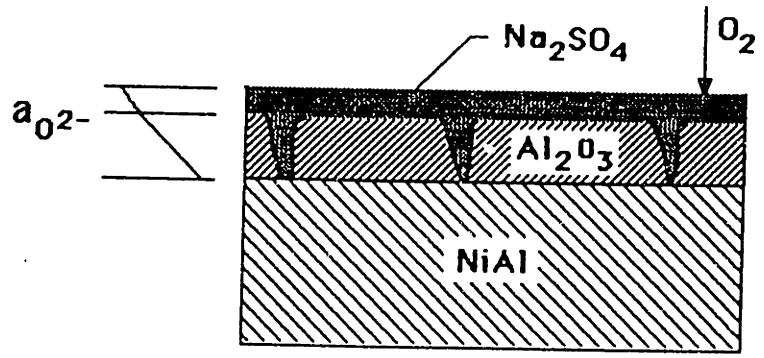

Na_2SO_4 can now react directly with Al in the coating:

$$\frac{2}{3}Al + SO_4^{2-} = O^{2-} + \frac{1}{3}Al_2S_3 + \frac{3}{2}O_2$$

The increase in $a_{O^{2-}}$ can lead to basic fluxing:

$$Al_2O_3 + O^{2-} = 2AlO_2^-$$

Fig. 32 Proposed mechanism by which thermal strains can accelerate hot-corrosion attack of aluminide coatings.

Chapter 5

Recommendations for Future Studies

As an extension of the work presented in this thesis the following further work is suggested:

1. Examination of the effect of substrate compression on the degradation of other coating systems, in particular Ni-Cr-Al-(Y) and Co-Cr-Al-(Y) overlay coatings. These coatings are typically applied at thicknesses twice that of aluminide coatings and are less prone to degradation by interdiffusion with the substrate. However, from the results of the present work it would be expected that scalloping would still occur with these coatings. That is, although the more stable Al content of the overlay coatings will aid in long term Al_2O_3 formation, initial surface roughening due to oxide cracking followed by scalloping (driven by coating compression) is still expected.

2. Formulation of flow and evolutionary equations for thermal fatigue. These equations are needed to determine the effect of micro-plastic flow on the stress-strain response of the induction heated disks. The equations must be able to model the effect of arbitrary load reversals on the subsequent stress strain response of a material. Changes in metallurgical strength occurring with

time, temperature and strain history should also be (ideally) included. A start in this direction is the formulation of McClintock, Holmes and Kim [77], which incorporates three parameters, Bauschinger stress and strain and rate of hardening ($d\epsilon_{Bausch.}/d\sigma$) in an effort to model the effect of arbitrary load reversals on subsequent stress strain response.

The successful application of these equations to predict stress-strain history depends critically upon the availability of cyclic stress-strain data, in the small strain-amplitude regime of interest for turbine airfoil substrates and coatings. This data is currently quite scarce and it may be necessary to implement a separate research program for its procurement.

3a. Experimental verification of the proposed mechanism for scallop growth by kinematically irreversible cyclic creep (Chapter 3). This could perhaps be verified by initial fatigue testing in air (to promote initial surface roughening) followed by testing in ultra-high purity argon or in vacuum to determine if further scallop growth occurs even in the absence of oxidation.

3b. Development of the models needed for a quantitative prediction of the effect of strain amplitude on scallop growth by kinematically irreversible cyclic creep. By numerical modeling, this could perhaps incorporate the results obtained from improved flow and evolutionary equations [77].

4. Development of a direct method for measurement of the strain history of the induction heated disk specimens. This could take the form of a displacement transducer with prongs inserted into small (≈ 0.3 mm) holes drilled into the specimen periphery. This would have to be accompanied by a redesign of the cooling manifolds to provide access to the specimen faces (one possible redesign of the cooling manifolds would be the use of radial air impingement).

Another possible alternative for strain measurement would be the use of x-ray pulsing to directly measure changes in lattice spacing occurring during the test cycles [78].

References

[1] Goward, G.W., *Journal of Metals,* Vol. 22, No. 10, 1970, pp. 31-39.

[2] Cooper, S.P. and Strang A., in *High Temperature Alloys for Gas Turbines 1982,* R. Brunetaud et al, Eds., D. Reidel Publishing Company, Dordrecht, Holland, 1982, pp. 249-260.

[3] Saunders, S.R.J., Hossain, M.K., and Ferguson, J.M., in *High Temperature Alloys for Gas Turbines 1982,* R. Brunetaud et al, Eds., D. Reidel Publishing Company, Dordrecht, Holland, 1982, pp. 177-206.

[4] Naagarajan, Y., Stringer, J. and Whittle, D.P., *Corrosion Science,* Vol. 22, 1982, pp.407-453.

[5] Lowell, C.E., Deadmore, D.L., and Whittenberger, J.D., *Oxidation of Metals,* Vol. 17, Nos. 3/4, 1982, pp. 205-221.

[6] Bourhis, Y. and St. John, C., *Oxidation of Metals,* Vol. 9, No. 6, 1975, pp. 507-527.

[7] Sivakumar, R., *Oxidation of Metals,* Vol. 17, 1982, pp. 27-41.

[8] Richards, M.N. and Stringer, J., *British Corrosion Journal,* Vol. 8, 1973, pp. 167-173.

[9] Elliot, J.F., in *Solid State Chemistry of Energy Conversion and Storage,* John B. Goodenough and M. Stanley Whittingham, Eds., Paper No. 13, 1977, pp. 225-239.

[10] Schneider, H., Von Arnim, H., and Grunling, H.W., *Thin Solid Films,* Vol. 84, 1981, pp. 29-36.

[11] Hsu, L., and Stetson, A., *Thin Solid Films*, Vol. 73, 1980, pp. 419-428.

[12] Castillo, R., and Willett, K.P., *Metallurgical Transactions*, Vol. 15A, 1984, pp. 229-236.

[13] Felix, P.C., in *Materials and Coatings to resist High Temperature Corrosion*, D.R. Holmes and A. Rahmel, Eds., Applied Science Publishers LTD, London, 1978, pp. 199-212.

[14] Nicoll, A.R., Wahl, G., and Hildebrandt, U.W., in *Materials and Coatings to resist High Temperature Corrosion*, D.R. Holmes and A. Rahmel, Eds., Applied Science Publishers LTD, London, 1978, pp. 233-252.

[15] Smeggil, J.G. and Bornstein, N.S., in *High-Temperature Protective Coatings* , C. Singhal, Ed., The Metallurgical Society of AIME, Warrendale, Pennsylvania, 1982, pp. 61-74.

[16] Levine, S.R., *Metallurgical Transactions A*, Vol. 9A, 1978, pp. 1237-1250.

[17] Fleetwood, M.J., *Journal of The Institute of Metals*, Vol. 98, 1970, pp. 1-7.

[18] Boone, D.H., Crane, D.A., and Whittle, D.P., *Thin Solid Films*, Vol. 84, 1981, pp. 39-47.

[19] Steinmetz, P., Roques, B., Dupre, B., Duret, C., and Morbioli, R., in *High-Temperature Protective Coatings*, S.C. Singhal, Ed., The Metallurgical Society of AIME, Warrendale, Pennsylvania, 1982, pp. 135-157.

[20] Mom, A.J.A., in *Behaviour of High Temperature Alloys in Aggressive Environments*, The Metals Society, London,

1979, pp. 363-374.

[21] Hart, A.B., Laxton, J.W., Stevens, C.G., and Tidy, D. in *Higl. Temperature Alloys for Gas Turbines,* D. Coutsouradis, et al, Eds., Applied Science Publishers Ltd, London, 1978, pp. 81-107.

[22] Saunders, S.R.J., Hossain, M.K., and Fergusion, J.M., in *Higl. Temperature Alloys for Gas Turbines 1982,* R. Brunetaud, et al, Eds., D. Reidel Publishing Company, Dordrecht, Holland, 1982, pp. 177-206.

[23] Mowbray, D.F., Woodford, D.A., and Brandt, D.E., in "*Fatigue at Elevated Temperatures, ASTM STP 520,* American Society for Testing and Materials, 1973, pp. 416-426.

[24] Howes, M.A.H., in "*Thermal Fatigue of Materials and Components, ASTM STP 612,* D.A. Spera and D.F. Mowbray, Eds., American Society for Testing and Materials, 1976, pp. 86-105.

[25] Kaufman, Albert, "Elastic-Plastic Finite-Element Analyses of Thermally Cycled Single-Edge Wedge Specimens", NASA Technical Paper 1982, National Aeronautics and Space Administration. Washington, D.C., 1982.

[26] Holmes, J.W., and McClintock, F.A., *Scripta Metallurgica,* 17, pp. 1365-1370, 1983.

[27] Miner, R.V., Voigt, R.C., Gayda, J., and Gabb, T.P., submitted to Metallurgical Transactions.

[28] Gabb, T.P., Gayda, J., and Miner, R.V., submitted to Metallurgical Transactions.

[29] Pichoir, R., in *High Temperature Alloys for Gas Turbines*, D. Coutsouradis, et al, Eds., Applied Science Press Ltd, London, 1978, pp.191-208.

[30] Goward, G.W., and Boone, D.H., *Oxidation of Metals*, Vol. 3, No.5, 1971, pp. 475-495.

[31] *ABAQUS Users Manual*, Hibbitt, Karlsson and Sorensen, Inc., Providence, R.I., July 1982.

[32] Janssen, M.M.P. and Rieck, G.D., *Transactions of The Metallurgical Society of AIME*, Vol. 239, 1967, pp. 1372-1390.

[33] Goward, G. W., Boone, D.H. and Giggins, C. S., *Transactions of the ASM*, Vol. 60, 1967, pp. 228-241.

[34] Lindblad, N.R., *Oxidation of Metals*, Vol.1, No.1, 1969, pp.143-150.

[35] Kriege, O. W. and Baris, J. M., *Transactions of the ASM*, Vol. 62, 1969, pp. 195-200.

[36] Kriege, O. W. and Sullivan, C.P., *ASM transactions Quarterly*, Vol. 61, 1968, pp. 278-290.

[37] Meng, Z., Sun, G. and Li, M., in *Superalloys 1984*, M. Gell et al, Eds., The Metallurgical Society of AIME, Warrendale Pennsylvania, 1984, pp. 563-572.

[38] Morinaga, M., Yukawa, N., Adachi, H. and Ezaki, H., in *Superalloys 1984*, M. Gell et al, Eds., The Metallurgical Society of AIME, Warrendale Pennsylvania, 1984, pp. 523-532.

[39] Lang, E. and Tottle, L., Preprint "Some Observations Concerning the Structural Stability of Aluminide Coatings on IN738LC", Joint Research Establishment, Petten, The Netherlands, 1986.

[40] Pettit, F.S. and Goward, G.W., in *Metallurgical Treatises*, J.K. Tien and J.F. Elliott, Eds., The Metallurgical Society of AIME, 420 Commonwealth Drive, Warrendale, Pa, 1981, pp. 603-619.

[41] General Electric Corporation, Lynn Massachusetts.

[42] Kaufman, M., "Physical and Mechanical Properties of an Aluminide Coating", TMS-AIME, Paper No. F82-11, 1982.

[43] Stewart, M., PhD thesis, University of Liverpool, 1984.

[44] Rahmel, A., *Oxidation of Metals*, Vol.2, No.1, 1970, pp.120-132.

[45] Kingery, W.D., Bowen, H.K. and Uhlmann, D.R., *Introduction to Ceramics*, John Wiley & Sons, New York, 1976, pp. 240 and 256.

[46] Yurek, G., Department of Materials Science and Engineering, M.I.T., private communication, 1986.

[47] Fleetwood, M.J., *Journal of The Institute of Metals*, Vol. 98, 1970, pp. 1-7.

[48] Berg, C.A. and McClintock, F.A., *Zeit. Angew Math Phys.*, Vol. 17, 1966, pp. 453-456.

[49] McClintock, F.A., *Fracture of Solids*, D.C. Drucker and J.J. Gilman, Eds., 1963, pp. 65-102.

[50] Strang, A. and Lang, E., in *High Temperature Alloys for Gas Turbines 1982,* R. Brunetaud et al, Eds., D. Reidel Publishing Company, Dordrecht, Holland, 1982, pp. 469-506.

[51] Goward, G.W., *Symposium on Properties of High Temperature Alloys,* Las Vegas, October 1976, pp. 806-823.

[52] Taylor, A. and Floyd, R.W., *Journal Institute Metals,* Vol. 81, 1952, pp. 451-464.

[54] Touloukian, Y.S., Kirby, R.K., Taylor, R.E. and Lee, T.Y.R., *Thermophysical Properties of Matter,* Vol. 13, IFI/Plenum, New York, 1979, pg. 176.

[55] Samsonov, G.V., *The Oxide Handbook,* Plenum, New York, 1973, pg. 183.

[56] Stearns, C.A., Miller, R.A., Kohl, F.J. and Fryburg, G.C., *Journal of The Electochemical Society,* Vol. 19, 1977, pp. 1145-1153.

[57] McCreath, C.G., *Tranactions of the Institute of Marine Engineering,* Vol. 88, 1976, pp. 145-158.

[58] Conde, J.F.G. and McCreath, C.G., *Proceedings Conference on Gas Turbines.* New Orleans. The American Society of Mechanical Engineers, March 1980.

[59] Goebel, J.A., Pettit, F.S. and Goward, G.W., *Metallurgical Transactions,* Vol. 4, 1973, pp. 261-278.

[60] Pettit, F.S. and Meier, G.H., *Superalloys 1984,* M. Gell et al, Eds., The Metallurgical Society of AIME, Warrendale Pennsylvania, 1984, pp. 651-687

[61] Shores, D.A., "New Perspectives on Hot Corrosion Mechanisms", General Electric Report No. 81CRD182, August 1981, Available through: General Electric Technical Information Exchange, Bldg. 81, Room A133, Schenectady New York, 12345.

[62] Bornstein, N.S. and DeCrescente, M.A., *Metallurgical Transactions,* Vol. 2, 1971, pp. 2875-2873

[63] Stringer, J., *Annual Review of Materials Science,* Vol. 7, 1977, pp. 477-490.

[64] Conde, J.F.G., Booth, G.C. and Taylor, A.F., *Materials Science and Technology,* Vol. 2, No. 3, 1986, pp. 314-317.

[65] Saunders, S.R.J., *Materials Science and Technology,* Vol. 2, No. 3, 1986, pp. 282-289.

[66] Mom, A.J.A. and Kolkman, H.J., *Proceedings International Gas Turbine Conference,* Amsterdam, American Society of Mechanical Engineers, June 1984.

[67] Hancock, P., *Corrosion Science,* Vol. 22, 1982, pp. 51-59.

[68] Laxton, J.W., Stevens, C.G. and Tidy, D., in *High Temperature Alloys for Gas Turbines 1982,* R. Brunetaud et al, Eds., D. Reidel Publishing Company, Dordrecht, Holland, 1982, pp. 149-175.

[69] Hot Corrosion Task Force for ASTM Gas Turbine Panel: Round Robin Test, American Society for Testing and Materials, Philidelphia, PA, 1970.

[70] Dean, A.V., National Gas Turbine Establishment, Pyestock, Farnborough, Report, Jan. 1964.

[71] Richards, M.N. and Stringer, J., *British Corrosion Journal*, Vol. 8, 1973, pp. 167-172.

[72] Barkalow, R.H. and Pettit, F.S., "Marine Gas Turbine Hot-Corrosion Dependence on Ingested Salt Levels", Report AD 071055, Pratt and Whitney Aircraft, Middletown, Conn., 1979.

[73] Schultz, J.W. and Hulsizer, W.R., *Materials Engineering Quarterly*, August, 1976, pp. 15-24.

[74] Sivakumar, R., *Oxidation of Metals*, Vol. 17, 1982, pp. 27-41.

[75] Wu. W.T., Rahmel, A. and Schorr, M., *Oxidation of Metals*, Vol. 22, 1984, pp. 59-71.

[76] Johnson, T., Department of Materials Science and Engineering, M.I.T., private communication, 1985.

[77] McClintock, F.A., Holmes, J.W. and Kim, A., "Flow and Evolutionary Equations For Thermal Fatigue", Research Memorandum No. 287, Fatigue and Plasticity Laboratory, M.I.T., 1986.

[78] Allen, S., Department of Materials Science and Engineering, M.I.T., private communication, 1985.

Appendix A

Calculation of Stiffness Constants for Rene M4

The stiffness constants E_{ijkl} used in ABAQUS [31] are obtained from the usual two-index stiffness constants C_{ij}, which for cubic symmetry are given by the isotropic elastic relations in terms of the <100> dynamic moduli E_{100}, G_{100} and Poisson's ratio υ_{100}:

$$E_{1111} = E_{2222} = E_{3333} \equiv C_{11} = E_{100}(1 - \upsilon_{100})/(1 + \upsilon_{100})(1 - 2\upsilon_{100}) \quad \text{(A1)}$$

$$E_{1122} = E_{1133} = E_{2233} \equiv C_{12} = E_{100}\upsilon_{100}/(1+ \upsilon_{100})(1-2\upsilon_{100}) \quad \text{(A2)}$$

$$E_{1212} = E_{1313} = E_{2323} \equiv C_{66} = G_{100} \ . \quad \text{(A3)}$$

Dynamic moduli. To determine whether the frequency of 5000 Hz at which the dynamic moduli were determined was high enough to preclude anelasticity, the bulk modulus ($B = E_{100}/3(1 - 2\upsilon_{100})$) was plotted versus temperature using the original values of E_{100} and υ_{100} given in Tables A2 and A3. As Fig. A1 shows, there is a sharp increase in apparent bulk modulus above approximately 900^0C, indicating that inelasticity occurs even at 5000 Hz. This

is further verified by the original values for υ_{100} which approach 0.5 at 1093^{0}C (see Table A2).

To isolate anelastic effects, E_{100} and G_{100} were normalized with respect to the extrapolated bulk modulus, B_{ex}. These normalized quantities were then extrapolated, as shown in Figs. A2a,b. The extrapolated ratios, along with the extrapolated bulk modulus (Fig. A1), gave corrected values for E_{100} and G_{100} (see Table A3). Likewise, corrected values for υ_{100} (Table A2) were obtained using the extrapolated values for E_{100}/B.

With the corrected values for E_{100}, G_{100}, and υ_{100} the stiffness constants C_{ij} were calculated from Eqs. A1-A3 and are plotted in Fig. A3.

Table A1 Bulk modulus and extrapolated bulk modulus obtained from Fig. A1.

Temp., °C	B, GPa (Original Data)	B_{ex}, GPa (Extrapolated Data)
25	179.6	179.6
204	173.4	173.4
427	165.9	165.9
538	161.5	161.5
649	157.3	157.3
760	154.1	152.3
871	152.6	147.0
982	179.6	139.7
1038	258.7	136.0
1093	428.0	131.7

Table A2 <100> - Poisson's ratio and extrapolated values for Poisson's ratio.

Temp., °C	$\upsilon_{<100>}$ (Original Data)	$\upsilon_{<100>}$ (Corrected Data)
25	0.380	0.380
204	0.381	0.381
427	0.383	0.383
538	0.384	0.384
649	0.386	0.386
760	0.390	0.388
871	0.396	0.391
982	0.420	0.394
1038	0.448	0.396
1093	0.471	0.398

Table A3 Dynamic moduli E_{100} and G_{100} (obtained at 5000 Hz) and corrected values of dynamic moduli obtained from Fig. A2.

Temp., °C	E_{100}, GPa (Original Data)	E_{100}, GPa (Corrected Data)	G_{100}, GPa (Original Data)	G_{100}, GPa (Corrected Data)
25	129.3	129.3	126.9	126.9
204	123.8	123.8	122.0	122.0
427	116.5	116.5	115.1	115.1
538	112.4	112.4	111.0	111.0
649	107.6	107.6	106.9	106.9
760	101.7	102.3	102.7	102.7
871	95.2	96.1	96.5	97.6
982	86.2	88.8	88.3	90.9
1038	80.7	84.9	81.4	87.4
1093	74.5	80.6	75.3	83.6

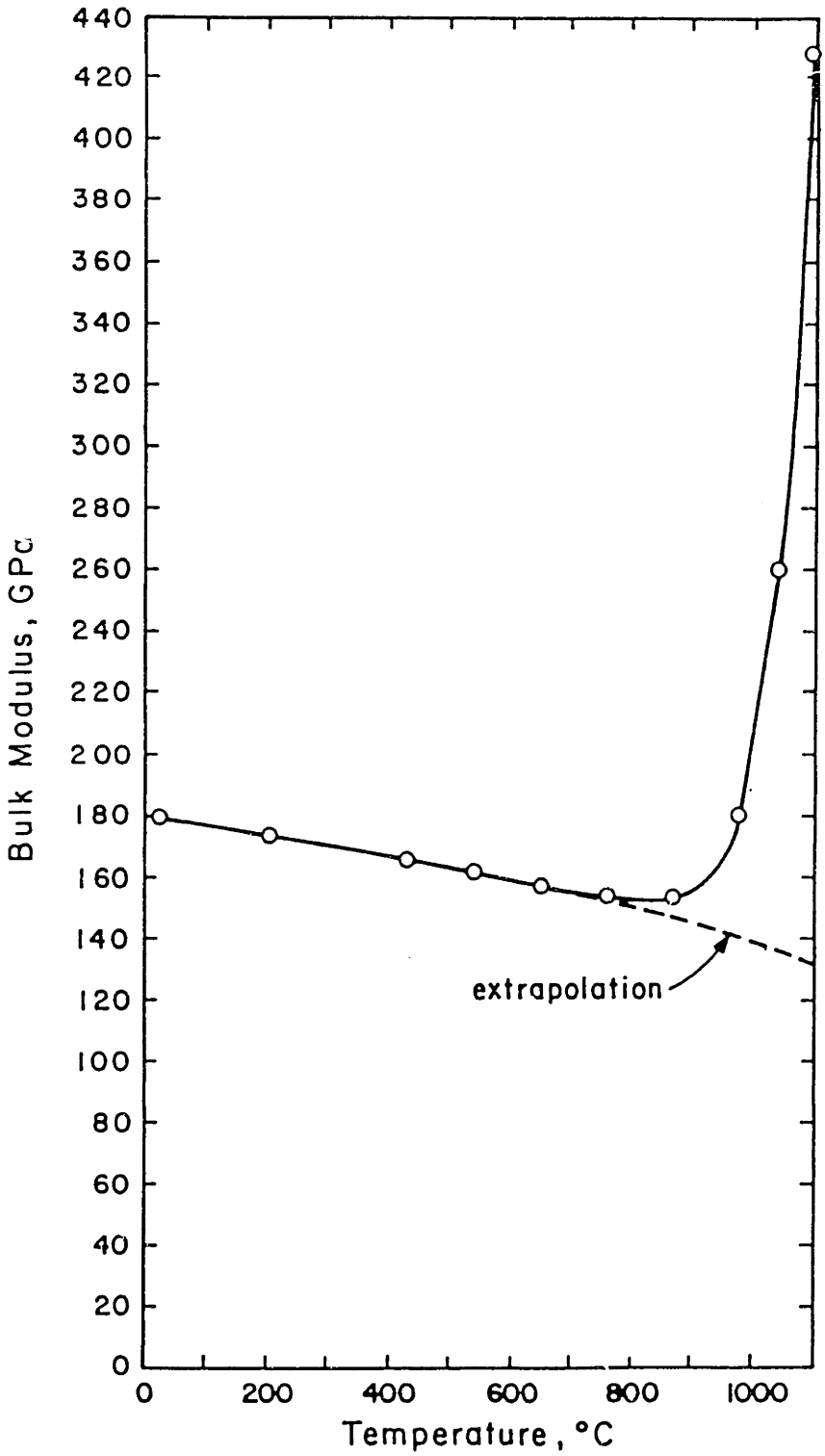

Fig. A1 Bulk modulus and extrapolated bulk modulus versus temperature for monocrystalline Rene N4. Bulk modulus was determined using <100> material constants in the relation $B = E_{100}/(1 - 2\upsilon_{100})$.

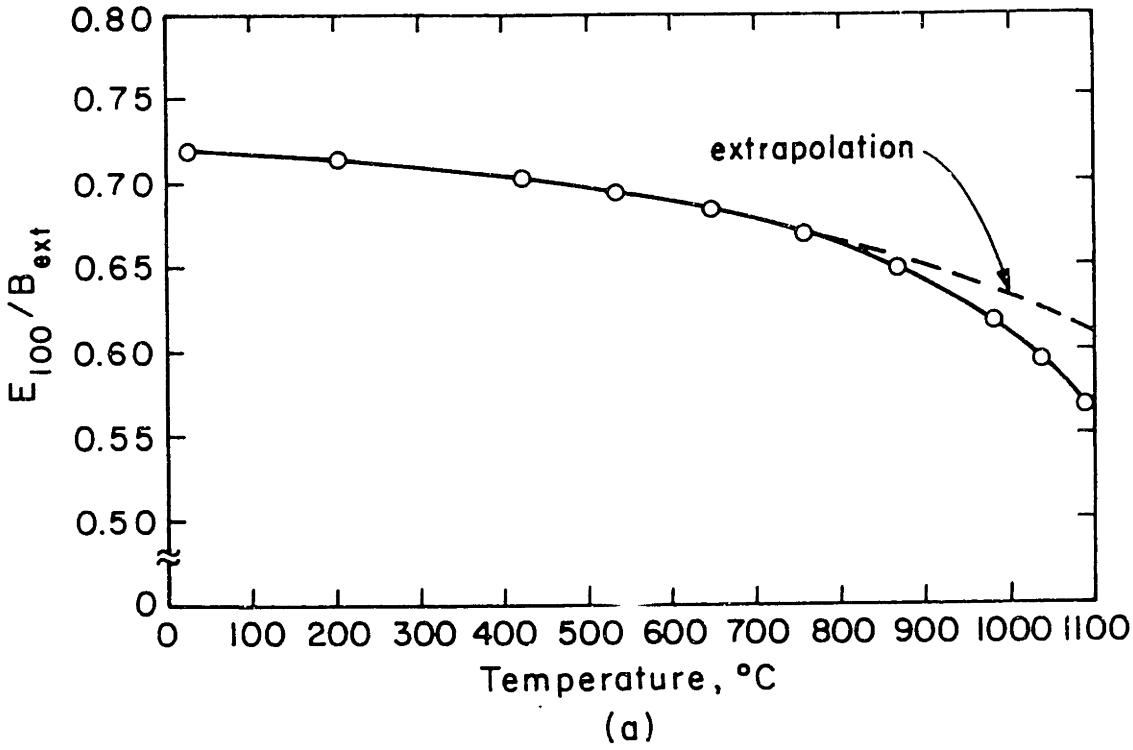

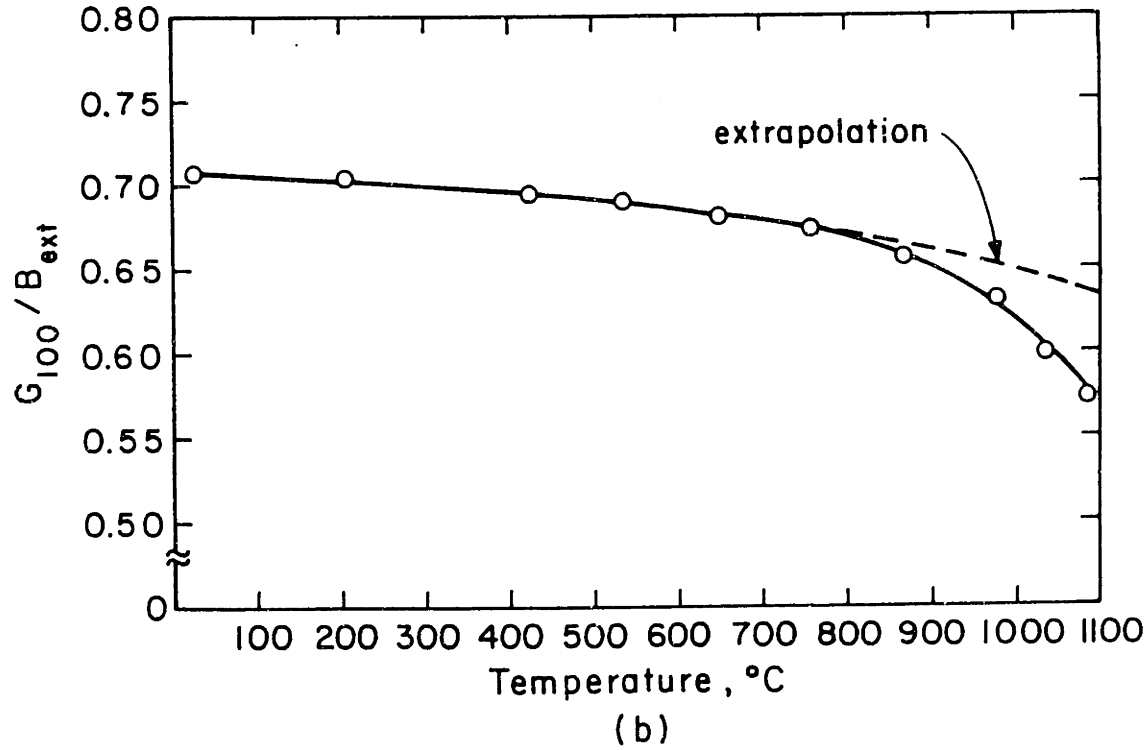

Fig. A2a,b Normalized <100> elastic and shear moduli (E_{100}/B, G_{100}/B) versus temperature for Rene N4.

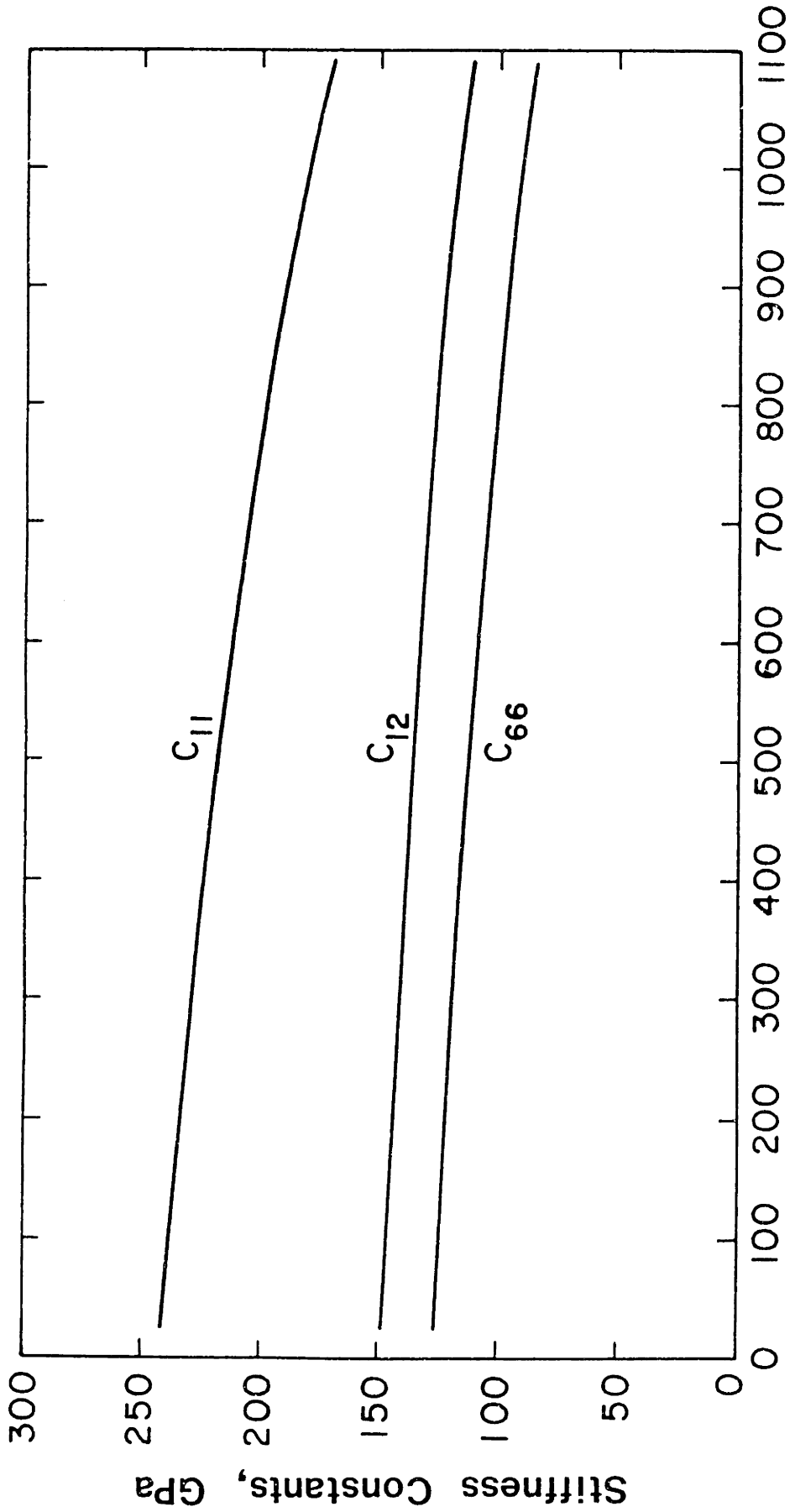

Fig. A3 Stiffness constants C_{ij} versus temperature for monocrystalline Rene N4.

Appendix B

Sample Input and Output Files For Thermoelastic Finite-Element Analysis of Specimen Stress-Strain History

Sample input and output files from the thermoelastic finite-element analysis for specimen stress-strain history are given in this appendix. The sample files presented are for the specimen temperature history of Fig. 7b. The results of the stress-strain analysis for this temperature history are plotted in Fig. 10b. To conserve space, only the first three seconds of the output file are given.

This example is on file at the Laboratory for Computational Mechanics of Materials and Manufacturing, M.I.T., Room 1-307 under file name R31.INFO.

Additional details can be obtained from: *ABAQUS Users Manual*, Hibbitt, Karlsson and Sorensen, Inc., Providence, R.I., July 1982.

```
*HEADING
** File R31.INFO, user: HOLMES, Data General MV 10000, 7 Jun 86
** Lab. for Computational Mechanics of Materials and Manufacturing
**
** NODEs (Users' 6.4.2-1) are grouped into nodesets (NSET) with
**a rectangular coordinate SYSTEM.  Each NSET has a radius,
**theta from 45 to 0 degrees.  Node numbers are theta, r coordinate.
**Numbers from theta = 45 degrees.
*NODE, NSET=R1, SYSTEM=R
**Node number, X-coord (meters), Y-coord (meters)
  101, .0009545, .0009545
  201, .0009065, .0010001
  301, .0008563, .0010434
  401, .0008041, .0010842
  501, .0007499, .0011223
  601, .0006939, .0011578
  701, .0006363, .0011904
  801, .0005771, .0012202
  901, .0005165, .0012471
 1001, .0004547, .0012709
 1101, .0003918, .0012917
 1201, .0003280, .0013093
 1301, .0002633, .0013239
 1401, .0001981, .0013352
 1501, .0001323, .0013433
 1601, .0000662, .0013482
 1701, .0000000, .0013498
*NODE, NSET=R2, SYSTEM=R
  102, .0011047, .0011047
  302, .0009911, .0012077
  502, .0008680, .0012990
  702, .0007365, .0013778
  902, .0005979, .0014434
 1102, .0004535, .0014950
 1302, .0003048, .0015323
 1502, .0001531, .0015548
 1702, .0000000, .0015623
*NODE, NSET=R3, SYSTEM=R
  103, .0012550, .0012550
  203, .0011919, .0013150
  303, .0011259, .0013719
  403, .0010572, .0014255
  503, .0009860, .0014757
  603, .0009124, .0015223
  703, .0008366, .0015652
  803, .0007588, .0016044
  903, .0006792, .0016397
 1003, .0005979, .0016711
 1103, .0005152, .0016984
 1203, .0004312, .0017216
 1303, .0003462, .0017407
 1403, .0002604, .0017556
 1503, .0001740, .0017663
 1603, .0000871, .0017727
 1703, .0000000, .0017748
*NODE, NSET=R4, SYSTEM=R
  104, .0014052, .0014052
  304, .0012607, .0015362
  504, .0011041, .0016524
  704, .0009368, .0017526
  904, .0007605, .0018360
 1104, .0005769, .0019017
 1304, .0003877, .0019491
```

```
 1504, .0001948, .0019777
 1704, .0000000, .0019873
*NODE, NSET=R5, SYSTEM=R
  105, .0015555, .0015555
  205, .0014773, .0016299
  305, .0013955, .0017005
  405, .0013104, .0017669
  505, .0012221, .0018291
  605, .0011309, .0018868
  705, .0010370, .0019400
  805, .0009405, .0019886
  905, .0008418, .0020323
 1005, .0007411, .0020712
 1105, .0006386, .0021051
 1205, .0005345, .0021339
 1305, .0004292, .0021575
 1405, .0003228, .0021760
 1505, .0002156, .0021892
 1605, .0001079, .0021972
 1705, .0000000, .0021998
*NODE, NSET=R6, SYSTEM=R
  106, .0017058, .0017058
  306, .0015303, .0018647
  506, .0013402, .0020058
  706, .0011372, .0021275
  906, .0009231, .0022287
 1106, .0007003, .0023084
 1306, .0004706, .0023659
 1506, .0002365, .0024007
 1706, .0000000, .0024123
*NODE, NSET=R7, SYSTEM=R
  107, .0018560, .0018560
  207, .0017627, .0019448
  307, .0016652, .0020290
  407, .0015636, .0021083
  507, .0014583, .0021824
  607, .0013494, .0022514
  707, .0012373, .0023149
  807, .0011222, .0023728
  907, .0010045, .0024250
 1007, .0008843, .0024714
 1107, .0007619, .0025118
 1207, .0006378, .0025461
 1307, .0005121, .0025744
 1407, .0003851, .0025964
 1507, .0002573, .0026122
 1607, .0001288, .0026216
 1707, .0000000, .0026248
*NODE, NSET=R8, SYSTEM=R
  108, .0020063, .0020063
  308, .0018000, .0021933
  508, .0015763, .0023591
  708, .0013375, .0025023
  908, .0010858, .0026213
 1108, .0008236, .0027151
 1308, .0005535, .0027828
 1508, .0002781, .0028236
 1708, .0000000, .0028373
*NODE, NSET=R9, SYSTEM=R
  109, .0021565, .0021565
  209, .0020481, .0022598
  309, .0019348, .0023575
  409, .0018168, .0024496
```

```
  509, .0016944, .0025358
  609, .0015679, .0026159
  709, .0014377, .0026897
  809, .0013040, .0027570
  909, .0011671, .0028176
 1009, .0010275, .0028715
 1109, .0008853, .0029185
 1209, .0007410, .0029584
 1309, .0005950, .0029912
 1409, .0004475, .0030168
 1509, .0002989, .0030351
 1609, .0001497, .0030461
 1709, .0000000, .0030498
*NODE, NSET=R10, SYSTEM=R
  110, .0025099, .0025099
  310, .0022518, .0027439
  510, .0019721, .0029514
  710, .0016733, .0031305
  910, .0013584, .0032794
 1110, .0010304, .0033968
 1310, .0006925, .0034814
 1510, .0003479, .0035325
 1710, .0000000, .0035496
*NODE, NSET=R11, SYSTEM=R
  111, .0028640, .0028640
  211, .0027200, .0030010
  311, .0025695, .0031309
  411, .0024127, .0032532
  511, .0022502, .0033677
  611, .0020822, .0034740
  711, .0019093, .0035720
  811, .0017317, .0036614
  911, .0015500, .0037419
 1011, .0013645, .0038135
 1111, .0011757, .0038758
 1211, .0009841, .0039289
 1311, .0007902, .0039724
 1411, .0005943, .0040064
 1511, .0003970, .0040307
 1611, .0001987, .0040454
 1711, .0000000, .0040502
*NODE, NSET=R12, SYSTEM=R
  112, .0032174, .0032174
  312, .0028865, .0035172
  512, .0025279, .0037832
  712, .0021449, .0040128
  912, .0017412, .0042037
 1112, .0013208, .0043541
 1312, .0008877, .0044626
 1512, .0004460, .0045281
 1712, .0000000, .0045501
*NODE, NSET=R13, SYSTEM=R
  113, .0035708, .0035708
  213, .0033913, .0037417
  313, .0032036, .0039036
  413, .0030082, .0040561
  513, .0028056, .0041988
  613, .0025961, .0043314
  713, .0023805, .0044536
  813, .0021591, .0045650
  913, .0019325, .0046655
 1013, .0017012, .0047547
 1113, .0014659, .0048324
```

```
 1213, .0012270, .0048985
 1313, .0009852, .0049528
 1413, .0007410, .0049952
 1513, .0004950, .0050255
 1613, .0002478, .0050438
 1713, .0000000, .0050499
*NODE, NSET=R14, SYSTEM=R
  114, .0039242, .0039242
  314, .0035207, .0042899
  514, .0030832, .0046144
  714, .0026161, .0048944
  914, .0021238, .0051272
 1114, .0016110, .0053107
 1314, .0010827, .0054430
 1514, .0005440, .0055229
 1714, .0000000, .0055497
*NODE, NSET=R15, SYSTEM=R
  115, .0042782, .0042782
  215, .0040631, .0044830
  315, .0038383, .0046769
  415, .0036042, .0048596
  515, .0033614, .0050306
  615, .0031105, .0051895
  715, .0028521, .0053359
  815, .0025868, .0054694
  915, .0023154, .0055897
 1015, .0020383, .0056966
 1115, .0017563, .0057898
 1215, .0014701, .0058690
 1315, .0011804, .0059340
 1415, .0008878, .0059848
 1515, .0005930, .0060212
 1615, .0002969, .0060430
 1715, .0000000, .0060503
*NODE, NSET=R16, SYSTEM=R
  116, .0046316, .0046316
  316, .0041553, .0050633
  516, .0036390, .0054462
  716, .0030877, .0057767
  916, .0025066, .0060515
 1116, .0019014, .0062681
 1316, .0012779, .0064242
 1516, .0006420, .0065186
 1716, .0000000, .0065501
*NODE, NSET=R17, SYSTEM=R
  117, .0049790, .0049790
  217, .0047287, .0052173
  317, .0044670, .0054431
  417, .0041946, .0056557
  517, .0039120, .0058547
  617, .0036200, .0060396
  717, .0033193, .0062100
  817, .0030106, .0063653
  917, .0026946, .0065054
 1017, .0023722, .0066298
 1117, .0020440, .0067382
 1217, .0017109, .0068304
 1317, .0013737, .0069061
 1417, .0010332, .0069652
 1517, .0006902, .0070075
 1617, .0003455, .0070329
 1717, .0000000, .0070414
*NODE, NSET=R18, SYSTEM=R
```

```
  118, .0050734, .0050734
  318, .0045517, .0055462
  518, .0039861, .0059657
  718, .0033822, .0063277
  918, .0027457, .0066287
 1118, .0020828, .0068659
 1318, .0013997, .0070370
 1518, .0007033, .0071403
 1718, .0000000, .0071748
*NODE, NSET=R19, SYSTEM=R
  119, .0051263, .0051263
  219, .0048686, .0053716
  319, .0045991, .0056041
  419, .0043186, .0058230
  519, .0040277, .0060279
  619, .0037271, .0062182
  719, .0034175, .0063936
  819, .0030996, .0065536
  919, .0027743, .0066978
 1019, .0024423, .0068259
 1119, .0021045, .0069375
 1219, .0017615, .0070324
 1319, .0014143, .0071103
 1419, .0010637, .0071712
 1519, .0007106, .0072147
 1619, .0003557, .0072409
 1719, .0000000, .0072496
*NODE, NSET=R20, SYSTEM=R
  120, .0052146, .0052146
  320, .0046784, .0057006
  520, .0040971, .0061318
  720, .0034764, .0065038
  920, .0028221, .0068132
 1120, .0021407, .0070570
 1320, .0014387, .0072329
 1520, .0007228, .0073391
 1720, .0000000, .0073746
*NODE, NSET=R21, SYSTEM=R
  121, .0053036, .0053036
  221, .0050370, .0055574
  321, .0047582, .0057979
  421, .0044680, .0060244
  521, .0041670, .0062364
  621, .0038560, .0064333
  721, .0035357, .0066148
  821, .0032068, .0067803
  921, .0028703, .0069295
 1021, .0025268, .0070620
 1121, .0021773, .0071774
 1221, .0018225, .0072756
 1321, .0014633, .0073563
 1421, .0011005, .0074192
 1521, .0007352, .0074643
 1621, .0003680, .0074914
 1721, .0000000, .0075004
*NODE, NSET=R22, SYSTEM=R
  122, .0053913, .0053913
  322, .0048369, .0058938
  522, .0042359, .0063395
  722, .0035942, .0067242
  922, .0029178, .0070441
 1122, .0022133, .0072962
 1322, .0014875, .0074780
```

```
 1522, .0007473, .0075878
 1722, .0000000, .0076245
*NODE, NSET=R23, SYSTEM=R
  123, .0054803, .0054803
  223, .0052048, .0057426
  323, .0049167, .0059911
  423, .0046169, .0062251
  523, .0043058, .0064441
  623, .0039845, .0066477
  723, .0036535, .0068352
  823, .0033137, .0070062
  923, .0029659, .0071603
 1023, .0026110, .0072972
 1123, .0022498, .0074166
 1223, .0018832, .0075180
 1323, .0015120, .0076014
 1423, .0011372, .0076664
 1523, .0007597, .0077130
 1623, .0003803, .0077410
 1723, .0000000, .0077503
*NODE, NSET=R24, SYSTEM=R
  124, .0055686, .0055686
  324, .0049960, .0060876
  524, .0043753, .0065480
  724, .0037124, .0069453
  924, .0030137, .0072758
 1124, .0022861, .0075361
 1324, .0015364, .0077239
 1524, .0007719, .0078373
 1724, .0000000, .0078752
*NODE, NSET=R25, SYSTEM=R
  125, .0056570, .0056570
  225, .0053726, .0059278
  325, .0050753, .0061842
  425, .0047657, .0064258
  525, .0044447, .0066519
  625, .0041129, .0068620
  725, .0037713, .0070555
  825, .0034205, .0072321
  925, .0030615, .0073912
 1025, .0026952, .0075325
 1125, .0023223, .0076557
 1225, .0019439, .0077604
 1325, .0015608, .0078465
 1425, .0011739, .0079136
 1525, .0007842, .0079617
 1625, .0003926, .0079906
 1725, .0000000, .0080002
*NODE, NSET=R26, SYSTEM=R
  126, .0057129, .0057129
  326, .0051254, .0062453
  526, .0044886, .0067176
  726, .0038085, .0071253
  926, .0030918, .0074643
 1126, .0023453, .0077314
 1326, .0015762, .0079240
 1526, .0007919, .0080403
 1726, .0000000, .0080792
*NODE, NSET=R27, SYSTEM=R
  127, .0057700, .0057700
  227, .0054799, .0060462
  327, .0051767, .0063078
  427, .0048609, .0065542
```

```
  527, .0045335, .0067848
  627, .0041951, .0069991
  727, .0038466, .0071965
  827, .0034889, .0073766
  927, .0031227, .0075389
 1027, .0027490, .0076830
 1127, .0023687, .0078086
 1227, .0019827, .0079155
 1327, .0015919, .0080032
 1427, .0011973, .0080717
 1527, .0007998, .0081207
 1627, .0004004, .0081502
 1727, .0000000, .0081600
*NODE, NSET=R28, SYSTEM=R
  128, .0058000, .0058000
  328, .0052036, .0063406
  528, .0045571, .0068201
  728, .0038666, .0072340
  928, .0031390, .0075781
 1128, .0023811, .0078493
 1328, .0016002, .0080449
 1528, .0008040, .0081630
 1728, .0000000, .0082025
*NODE, NSET=R29, SYSTEM=R
  129, .0058301, .0058301
  229, .0055370, .0061091
  329, .0052306, .0063735
  429, .0049115, .0066224
  529, .0045807, .0068555
  629, .0042388, .0070720
  729, .0038867, .0072714
  829, .0035252, .0074534
  929, .0031552, .0076174
 1029, .0027777, .0077630
 1129, .0023934, .0078900
 1229, .0020034, .0079979
 1329, .0016085, .0080866
 1429, .0012098, .0081558
 1529, .0008082, .0082053
 1629, .0004046, .0082351
 1729, .0000000, .0082450
*NODE, NSET=R30, SYSTEM=R
  130, .0058601, .0058601
  330, .0052575, .0064063
  530, .0046043, .0068908
  730, .0039067, .0073089
  930, .0031715, .0076567
 1130, .0024057, .0079306
 1330, .0016161, .0081283
 1530, .0008123, .0082476
 1730, .0000000, .0082875
*NODE, NSET=R31, SYSTEM=R
  131, .0058902, .0058902
  231, .0055941, .0061721
  331, .0052845, .0064392
  431, .0049622, .0066907
  531, .0046279, .0069261
  631, .0042825, .0071449
  731, .0039267, .0073464
  831, .0035615, .0075302
  931, .0031878, .0076959
 1031, .0028063, .0078431
 1131, .0024181, .0079713
```

```
 1231, .0020240, .0080804
 1331, .0016251, .0081699
 1431, .0012223, .0082398
 1531, .0008165, .0082899
 1631, .0004087, .0083200
 1731, .0000000, .0083300
*NODE, NSET=R32, SYSTEM=R
  132, .0059203, .0059202
  332, .0053115, .0064720
  532, .0046515, .0069615
  732, .0039468, .0073839
  932, .0032040, .0077352
 1132, .0024304, .0080120
 1332, .0016334, .0082116
 1532, .0008207, .0083322
 1732, .0000000, .0083725
*NODE, NSET=R33, SYSTEM=R
  133, .0059503, .0059503
  233, .0056512, .0062351
  333, .0053384, .0065049
  433, .0050128, .0067590
  533, .0046751, .0069968
  633, .0043262, .0072178
  733, .0039668, .0074214
  833, .0035979, .0076071
  933, .0032203, .0077744
 1033, .0028349, .0079231
 1133, .0024428, .0080527
 1233, .0020447, .0081628
 1333, .0016417, .0082533
 1433, .0012347, .0083239
 1533, .0008248, .0083745
 1633, .0004129, .0084049
 1733, .0000000, .0084150
*NODE, NSET=R34, SYSTEM=R
  134, .0059804, .0059804
  334, .0053654, .0065377
  534, .0046987, .0070322
  734, .0039868, .0074588
  934, .0032365, .0078137
 1134, .0024551, .0080933
 1334, .0016500, .0082950
 1534, .0008290, .0084168
 1734, .0000000, .0084575
*NODE, NSET=R35, SYSTEM=R
  135, .0060104, .0060104
  235, .0057083, .0062981
  335, .0053923, .0065706
  435, .0050634, .0068273
  535, .0047224, .0070675
  635, .0043699, .0072907
  735, .0040069, .0074963
  835, .0036342, .0076839
  935, .0032528, .0078530
 1035, .0028636, .0080031
 1135, .0024674, .0081340
 1235, .0020653, .0082453
 1335, .0016583, .0083367
 1435, .0012472, .0084080
 1535, .0008332, .0084591
 1635, .0004171, .0084898
 1735, .0000000, .0085000
**
```

```
**Node set generator (Users' 6.4.2-1).  All nodes from 1701 to 1735
**(increment of 1) belong to NSET1.   All Nodes from 101 to 135
**belong to NSET2.   These node sets are used later to specify
**boundary conditions along theta = 90, 45 degrees.
*NSET, NSET=NSET1, GENERATE
1701, 1735 ,1
*NSET, NSET=NSET2, GENERATE
101, 135, 1
**
**ELEMENT definition (USERS'3.2.3-3).  CPS8 refers to 8-node biquadratic
**plane stress elements; nodes from corner left ccw around corners.
**then mid-points (see skectch below).
**
*ELEMENT, TYPE=CPS8
**Element number, node numbers of element
1, 301, 101, 103, 303 ,201 ,102 ,203 ,302
2, 501, 301, 303, 503 ,401 ,302 ,403 ,502
3, 701, 501, 503, 703 ,601 ,502 ,603 ,702
4, 901, 701, 703, 903 ,801 ,702 ,803 ,902
5, 1101,901, 903, 1103,1001,902 ,1003,1102
6, 1301,1101,1103,1303,1201,1102,1203,1302
7, 1501,1301,1303,1503,1401,1302,1403,1502
8, 1701,1501,1503,1703,1601,1502,1603,1702
9, 303, 103, 105, 305 ,203 ,104 ,205 ,304
10,503, 303, 305, 505 ,403 ,304 ,405 ,504
11,703, 503, 505, 705 ,603 ,504 ,605 ,704
12,903, 703, 705, 905 ,803 ,704 ,805 ,904
13,1103,903, 905, 1105,1003,904 ,1005,1104
14,1303,1103,1105,1305,1203,1104,1205,1304
15,1503,1303,1305,1505,1403,1304,1405,1504
16,1703,1503,1505,1705,1603,1504,1605,1704
17,305, 105, 107, 307 ,205 ,106 ,207 ,306
18, 505, 305, 307, 507 ,405 ,306 ,407 ,506
19, 705, 505, 507, 707 ,605 ,506 ,607 ,706
20, 905, 705, 707, 907 ,805 ,706 ,807 ,906
21,1105,905, 907, 1107,1005,906 ,1007,1106
22,1305,1105,1107,1307,1205,1106,1207,1306
23,1505,1305,1307,1507,1405,1306,1407,1506
24,1705,1505,1507,1707,1605,1506,1607,1706
25, 307, 107, 109, 309 ,207 ,108 ,209 ,308
26, 507, 307, 309, 509 ,407 ,308 ,409 ,508
27, 707, 507, 509, 709 ,607 ,508 ,609 ,708
28, 907, 707, 709, 909 ,807 ,708 ,809 ,908
29,1107,907, 909, 1109,1007,908 ,1009,1108
30,1307,1107,1109,1309,1207,1108,1209,1308
31,1507,1307,1309,1509,1407,1308,1409,1508
32,1707,1507,1509,1709,1607,1508,1609,1708
33, 309, 109, 111, 311 ,209 ,110 ,211 ,310
34, 509, 309, 311, 511 ,409 ,310 ,411 ,510
35, 709, 509, 511, 711 ,609 ,510 ,611 ,710
36, 909, 709, 711, 911 ,809 ,710 ,811 ,910
37,1109,909, 911, 1111,1009,910 ,1011,1110
38,1309,1109,1111,1311,1209,1110,1211,1310
39,1509,1309,1311,1511,1409,1310,1411,1510
40,1709,1509,1511,1711,1609,1510,1611,1710
41, 311, 111, 113, 313 ,211 ,112 ,213 ,312
42, 511, 311, 313, 513 ,411 ,312 ,413 ,512
43, 711, 511, 513, 713 ,611 ,512 ,613 ,712
44, 911, 711, 713, 913 ,811 ,712 ,813 ,912
45,1111,911, 913, 1113,1011,912 ,1013,1112
46,1311,1111,1113,1313,1211,1112,1213,1312
47,1511,1311,1313,1513,1411,1312,1413,1512
48,1711,1511,1513,1713,1611,1512,1613,1712
```

```
49, 313, 113, 115, 315 ,213 ,114 ,215 ,314
50, 513, 313, 315, 515 ,413 ,314 ,415 ,514
51, 713, 513, 515, 715 ,613 ,514 ,615 ,714
52, 913, 713, 715, 915 ,813 ,714 ,815 ,914
53,1113,913, 915, 1115,1013,914 ,1015,1114
54,1313,1113,1115,1315,1213,1114,1215,1314
55,1513,1313,1315,1515,1413,1314,1415,1514
56,1713,1513,1515,1715,1613,1514,1615,1714
57, 315, 115, 117, 317 ,215 ,116 ,217 ,316
58, 515, 315, 317, 517 ,415 ,316 ,417 ,516
59, 715, 515, 517, 717 ,615 ,516 ,617 ,716
60, 915, 715, 717, 917 ,815 ,716 ,817 ,916
61,1115,915, 917, 1117,1015,916 ,1017,1116
62,1315,1115,1117,1317,1215,1116,1217,1316
63,1515,1315,1317,1517,1415,1316,1417,1516
64,1715,1515,1517,1717,1615,1516,1617,1716
65, 317, 117, 119, 319 ,217 ,118 ,219 ,318
66, 517, 317, 319, 519 ,417 ,318 ,419 ,518
67, 717, 517, 519, 719 ,617 ,518 ,619 ,718
68, 917, 717, 719, 919 ,817 ,718 ,819 ,918
69,1117,917, 919, 1119,1017,918 ,1019,1118
70,1317,1117,1119,1319,1217,1118,1219,1318
71,1517,1317,1319,1519,1417,1318,1419,1518
72,1717,1517,1519,1719,1617,1518,1619,1718
73, 319, 119, 121, 321 ,219 ,120 ,221 ,320
74, 519, 319, 321, 521 ,419 ,320 ,421 ,520
75, 719, 519, 521, 721 ,619 ,520 ,621 ,720
76, 919, 719, 721, 921 ,819 ,720 ,821 ,920
77,1119,919, 921, 1121,1019,920 ,1021,1120
78,1319,1119,1121,1321,1219,1120,1221,1320
79,1519,1319,1321,1521,1419,1320,1421,1520
80,1719,1519,1521,1721,1619,1520,1621,1720
81, 321, 121, 123, 323 ,221 ,122 ,223 ,322
82, 521, 321, 323, 523 ,421 ,322 ,423 ,522
83, 721, 521, 523, 723 ,621 ,522 ,623 ,722
84, 921, 721, 723, 923 ,821 ,722 ,823 ,922
85,1121,921, 923, 1123,1021,922 ,1023,1122
86,1321,1121,1123,1323,1221,1122,1223,1322
87,1521,1321,1323,1523,1421,1322,1423,1522
88,1721,1521,1523,1723,1621,1522,1623,1722
89, 323, 123, 125, 325 ,223 ,124 ,225 ,324
90, 523, 323, 325, 525 ,423 ,324 ,425 ,524
91, 723, 523, 525, 725 ,623 ,524 ,625 ,724
92, 923, 723, 725, 925 ,823 ,724 ,825 ,924
93,1123,923, 925, 1125,1023,924 ,1025,1124
94,1323,1123,1125,1325,1223,1124,1225,1324
95,1523,1323,1325,1525,1423,1324,1425,1524
96,1723,1523,1525,1725,1623,1524,1625,1724
97, 325, 125, 127, 327 ,225 ,126 ,227 ,326
98, 525, 325, 327, 527 ,425 ,326 ,427 ,526
99, 725, 525, 527, 727 ,625 ,526 ,627 ,726
100,925, 725, 727, 927 ,825 ,726 ,827 ,926
101,1125,925, 927, 1127,1025,926 ,1027,1126
102,1325,1125,1127,1327,1225,1126,1227,1326
103,1525,1325,1327,1527,1425,1326,1427,1526
104,1725,1525,1527,1727,1625,1526,1627,1726
105,327, 127, 129, 329 ,227 ,128 ,229 ,328
106,527, 327, 329, 529 ,427 ,328 ,429 ,528
107,727, 527, 529, 729 ,627 ,528 ,629 ,728
108,927, 727, 729, 929 ,827 ,728 ,829 ,928
109,1127,927, 929, 1129,1027,928 ,1029,1128
110,1327,1127,1129,1329,1227,1128,1229,1328
111,1527,1327,1329,1529,1427,1328,1429,1528
```

```
112,1727,1527,1529,1729,1627,1528,1629,1728
113,329, 129, 131, 331 ,229 ,130 ,231 ,330
114,529, 329, 331, 531 ,429 ,330 ,431 ,530
115,729, 529, 531, 731 ,629 ,530 ,631 ,730
116,929, 729, 731, 931 ,829 ,730 ,831 ,930
117,1129,929, 931, 1131,1029,930 ,1031,1130
118,1329,1129,1131,1331,1229,1130,1231,1330
119,1529,1329,1331,1531,1429,1330,1431,1530
120,1729,1529,1531,1731,1629,1530,1631,1730
121,331, 131, 133, 333, 231, 132, 233 ,332
122,531, 331, 333, 533, 431, 332, 433, 532
123,731, 531, 533, 733, 631, 532, 633, 732
124,931, 731, 733, 933, 831, 732, 833, 932
125,1131,931, 933, 1133,1031,932 ,1033,1132
126,1331,1131,1133,1333,1231,1132,1233,1332
127,1531,1331,1333,1533,1431,1332,1433,1532
128,1731,1531,1533,1733,1631,1532,1633,1732
129,333, 133, 135, 335, 233, 134, 235, 334
130,533, 333, 335, 535, 433, 334, 435, 534
131,733, 533, 535, 735, 633, 534, 635, 734
132,933, 733, 735, 935, 833, 734, 835, 934
133,1133,933, 935, 1135,1033,934 ,1035,1134
134,1333,1133,1135,1335,1233,1134,1235,1334
135,1533,1333,1335,1535,1433,1334,1435,1534
136,1733,1533,1535,1735,1633,1534,1635,1734
**
**ELSET (Users' 6.5.8-1) allows assigning elements to a set which
**can be called later (e.g., to specify output for specific elements).
**ELSET1 groups elements for output of data along periphery.
**ELSET2, ELSET2, and ELSET3 group together elements for later
**specification of mesh thickness (see ATTRIBUTE).
**
*ELSET, ELSET=ELSET1
129, 136
*ELSET, ELSET=TSET1
1,2,3,4,5,5,7,8,9,10,11,12,13,14,15,
16,17,18,19,20,21,22,23,24,25,26,27,
28,29,30,31,32,33,34,35,36,37,38,39,
40,41,42,43,44,45,46,47,48,49,50,51,
52,53,54,55,56,57,58,59,60,61,62,63,
64
*ELSET, ELSET=TSET2
65,66,67,68,69,70,71,72
*ELSET, ELSET=TSET3
73,74,75,76,77,78,
79,80,81,82,83,84,85,86,87,88,89,90,91,
92,93,94,95,96,97,98,99,100,101,102,103,
104,105,106,107,108,109,110,111,112,113,
114,115,116,117,118,119,120,121,122,123,
124,125,126,127,128,129,130,131,132,133,
134,135,136
**
**ATTRIBUTE (Users' 6.5.2-1) specifies element thickness for
**elements belonging to an element set (ELSET=TSET1 has a
**thickness of 0.0009 meters)
**
*ATTRIBUTE, ELSET=TSET1
.0018
*ATTRIBUTE, ELSET=TSET2
.00135
*ATTRIBUTE, ELSET=TSET3
.0090
**
```

```
**AMPLITUDE (Users' 6.8.1-1) option defines the time (seconds)
**vs. temperature (C) curve followed by the specimen at a particular
**radius. NAME (by radius)defines the AMPLITUDE curve for later recall.
**VALUE=A  designates that the vaules used are Absolute.  TIME=A
**designates that the time is Accumulated.
**
*AMPLITUDE, NAME=RR1, VALUE=A, TIME=A
**Time (s),  Temperature (C)
0.0,  504.,  1.0,  504.,  2.0,  520.,  3.0,  567.
4.0,  628.,  5.0,  685.,  6.0,  745.,  7.0,  796.
8.0,  835.,  9.0,  862., 10.0,  874., 11.0, 879.
12.0, 884.,  13.0, 887., 14.0,  892., 15.0, 894.
20.0, 899.,  25.0, 902., 30.0,  902., 35.0, 902.
40.0, 902.,  45.0, 902., 50.0, 902., 55.0, 902.
60.0, 902.,  67.8, 902., 68.0, 902.,  69.0, 892.
70.0, 860.,  71.0, 825., 72.0, 793., 73.0, 771.
74.0, 740.,  75.0, 721., 76.0, 697., 77.0, 680.
78.0, 664.,  79.0, 645., 81.0, 616., 83.0, 593.
85.0, 572.,  87.0, 553., 89.0, 539., 91.0, 525.
93.0, 518.,  95.0, 513., 97.0, 509., 99.0, 506.
101.0,504., 103.0, 504.
*AMPLITUDE, NAME=RR2, VALUE=A, TIME=A
0.0,  504.,  1.0,  506.,  2.0,  535., 3.0,  591.
4.0,  649.,  5.0,  719.,  6.0,  781., 7.0,  830.
8.0,  872.,  9.0,  895., 10.0,  907., 11.0, 912.
12.0, 914.,  13.0, 917., 14.0,  922., 15.0, 925.
20.0, 930.,  25.0, 935., 30.0,  937., 35.0, 943.
40.0, 943.,  45.0, 943., 50.0, 943.,  55.0, 943.
60.0, 943.,  67.8, 943., 68.0, 940.,  69.0, 910.
70.0, 874.,  71.0, 832., 72.0, 803., 73.0, 774.
74.0, 745.,  75.0, 723., 76.0, 702., 77.0, 680.
78.0, 665.,  79.0, 647., 81.0, 616., 83.0, 593.
85.0, 572.,  87.0, 551., 89.0, 537., 91.0, 525.
93.0, 515.,  95.0, 511., 97.0, 509., 99.0, 506.
101.0,504., 103.0, 504.
*AMPLITUDE, NAME=RR3, VALUE=A, TIME=A
0.0,  508.,  1.0,  518.,  2.0,  591., 3.0,  631.
4.0,  685.,  5.0,  779.,  6.0,  842., 7.0,  899.
8.0,  935.,  9.0,  952., 10.0,  960., 11.0, 962.
12.0, 965.,  13.0, 967., 14.0,  970., 15.0, 973.
20.0, 978.,  25.0, 980., 30.0,  983., 35.0, 983.
40.0, 983.,  45.0, 983., 50.0, 983.,  55.0, 983.
60.0, 983.,  67.8, 984., 68.0, 983.,  69.0, 943.
70.0, 897.,  71.0, 857., 72.0, 825., 73.0, 791.
74.0, 764.,  75.0, 735., 76.0, 714., 77.0, 692.
78.0, 673.,  79.0, 657., 81.0, 624., 83.0, 598.
85.0, 574.,  87.0, 555., 89.0, 541., 91.0, 527.
93.0, 520.,  95.0, 515., 97.0, 513., 99.0, 511.
101.0,508., 103.0, 508.
*AMPLITUDE, NAME=RR4, VALUE=A, TIME=A
0.0,  509.,  1.0,  520.,  2.0,  572., 3.0,  649.
4.0,  731.,  5.0,  803.,  6.0,  867., 7.0,  922.
8.0,  955.,  9.0,  973., 10.0,  975., 11.0, 978.
12.0, 980.,  13.0, 986., 14.0,  986., 15.0, 988.
20.0, 993.,  25.0, 999., 30.0,  999., 35.0, 999.
40.0, 999.,  45.0, 999., 50.0,  999., 55.0, 999.
60.0, 999.,  67.8, 999., 68.0,  996., 69.0, 942.
70.0, 897.,  71.0, 860., 72.0,  825., 73.0, 793.
74.0, 767.,  75.0, 738., 76.0,  716., 77.0, 695.
78.0, 673.,  79.0, 657., 81.0,  621., 83.0, 596.
85.0, 572.,  87.0, 556., 89.0,  539., 91.0, 525.
93.0, 520.,  95.0, 516., 97.0,  513., 99.0, 511.
101.0,511., 103.0, 508.
```

```
*AMPLITUDE, NAME=RR5, VALUE=A, TIME=A
0.0,  511.,  1.0,  532.,  2.0,  603., 3.0,  685.
4.0,  769.,  5.0,  843.,  6.0,  912., 7.0,  958.
8.0,  986.,  9.0,  996., 10.0,  999., 11.0,1001.
12.0,1004.,  13.0,1006., 14.0, 1009., 15.0,1011.
20.0,1014.,  25.0,1017., 30.0, 1017., 35.0,1017.
40.0,1017.,  45.0,1017., 50.0, 1017., 55.0,1017.
60.0,1017.,  67.8,1017., 68.0, 1006., 69.0, 947.
70.0, 900.,  71.0, 857., 72.0,  825., 73.0, 791.
74.0, 764.,  75.0, 738., 76.0,  714., 77.0, 692.
78.0, 674.,  79.0, 657., 81.0,  621., 83.0, 596.
85.0, 572.,  87.0, 551., 89.0,  539., 91.0, 525.
93.0, 520.,  95.0, 518., 97.0,  516., 99.0, 513.
101.0,511., 103.0, 511.
*AMPLITUDE, NAME=RR6, VALUE=A, TIME=A
0.0,  518.,  1.0,  555.,  2.0,  657., 3.0,  767.
4.0,  862.,  5.0,  947.,  6.0, 1006., 7.0, 1053.
8.0, 1080.,  9.0, 1080., 10.0, 1080., 11.0,1080.
12.0,1080.,  13.0,1080., 14.0, 1080., 15.0,1080.
20.0,1080.,  25.0,1080., 30.0, 1080., 35.0,1080.
40.0,1080.,  45.0,1080., 50.0, 1080., 55.0,1080.
60.0,1080.,  67.8,1080., 68.0, 1047., 69.0, 955.
70.0, 900.,  71.0, 858., 72.0,  819., 73.0, 788.
74.0, 757.,  75.0, 728., 76.0,  706., 77.0, 683.
78.0, 666.,  79.0, 645., 81.0,  614., 83.0, 586.
85.0, 565.,  87.0, 544., 89.0,  532., 91.0, 525.
93.0, 520.,  95.0, 520., 97.0,  518., 99.0, 518.
101.0,518., 103.0, 518.
**
**INITIAL CONDITIONS (Users' 6.11.2-1) allows specifying the
**initial temperature history (e.g., all nodes belonging to
**NSET R1 have an initial temperature of 504 C)
**
*INITIAL CONDITIONS, TYPE=TEMPERATURE
R1,  504.
R2,  504.
R3,  504.
R4,  504.
R5,  504.
R6,  504.
R7,  504.
R8,  504.
R9,  504.
R10, 504.
R11, 504.
R12, 504.
R13, 508.
R14, 508.
R15, 509.
R16, 511.
R17, 511.
R18, 518.
R19, 518.
R20, 518.
R21, 518.
R22, 518.
R23, 518.
R24, 518.
R25, 518.
R26, 518.
R27, 518.
R28, 518.
R29, 518.
```

```
R30, 518.
R31, 518.
R32, 518.
R33, 518.
R34, 518.
R35, 518.
**
**The TRANSFORM statement (Users' 6.4.7-1) allows specifying 45 degree
**boundary conditions in another more convenient coordinate system.
**
*TRANSFORM,NSET=NSET2
.0056570, .0056570, 0.0, -.0056570, .0056570, 0.0
**
**BOUNDARY (Users' 6.7.2-1) is used to specify fixed boundary
**conditions for nodes belonging to a node set.
**NSET1 has zero displacement in the 1 direction (dof 1 constrained).
**NSET2 has zero displacement in the transformed 2 direction (dof 2
**constrained).
**
*BOUNDARY
NSET1,1,,0.0
NSET2,2,,0.0
**
**MATERIAL (Users' 6.6.2-1) indicates the beginning of a MATERIAL
**input block.
**
*MATERIAL
**
**ELASTIC (Users' 6.6.8-1) specifies elastic material behavior.
**The level of anisotropy is chosen by the parameter TYPE.  For
**ORTHOtropic behavior the elastic moduli are entered as:
**E1111, E1122, E2222, E1133, E2233, E3333, E1212, E1313,
**E2323, temperature (C)
**
*ELASTIC, TYPE=ORTHO
242.0E9,148.4E9,242.0E9,148.4E9,148.4E9,242.0E9,126.9E9,126.9E9,
126.9E9,25.
233.1E9,143.5E9,233.1E9,143.5E9,143.5E9,233.1E9,122.0E9,122.0E9,
122.0E9,204.
222.1E9,137.9E9,222.1E9,137.9E9,137.9E9,222.1E9,115.1E9,115.1E9,
115.1E9,427.
215.9E9,134.4E9,215.9E9,134.4E9,134.4E9,215.9E9,111.0E9,111.0E9,
111.0E9,537.
209.1E9,131.4E9,209.1E9,131.4E9,131.4E9,209.1E9,106.9E9,106.9E9,
106.9E9,648.
202.9E9,129.7E9,202.9E9,129.7E9,129.7E9,202.9E9,102.7E9,102.7E9,
102.7E9,760.
190.6E9,124.5E9,190.6E9,124.5E9,124.5E9,190.6E9,94.6E9,94.6E9,
94.6E9,871.
178.7E9,119.1E9,178.7E9,119.1E9,119.1E9,178.7E9,87.6E9,87.6E9,
87.6E9,982.
170.6E9,114.7E9,170.6E9,114.7E9,114.7E9,170.6E9,83.4E9,83.4E9,
83.4E9,1038.
161.1E9,110.1E9,161.1E9,110.1E9,110.1E9,161.1E9,78.2E9,78.2E9,
78.2E9,1093.
**
**EXPANSION (Users' 6.6.9-1) - Input card for mean coefficient
**of thermal expansion.  ZERO allows specifying the reference
**temperature at which the data was obtained.
**
*EXPANSION, ZERO=25.
**mean coefficient of thermal expansion, temperature
12.15E-06, 300.
```

```
12.51E-06, 400.
12.78E-06, 500.
13.14E-06, 600.
13.41E-06, 700.
13.97E-06, 800.
14.62E-06, 900.
15.41E-06, 1000.
16.52E-06, 1100.
**
**RESTART (Users' 6.8.4-1) allows periodically writing the data
**to a restart file for use in subsequent runs.
**Parameters:  WRITE - specifies that the data is to be
**written to a restart file every FREQ time increments.
*RESTART, WRITE, FREQ=10
**STEP (Users' 7.2.1-1) begins a time step.
**Parameters:  LINEAR specifies that the analysis is
**entirely elastic.
**INC specifies the maximum number of increments allowed during
**a single step.
**STATIC (Users' 7.3.2-1) specifies that the STEP should be
**analyzed as a static load step.
**Parameters:  DIRECT specifies direct user control of the
**incrementation used during a step (for nonlinear problems
**automatic control over the step size is possible see Users'
**7.3.2-6)
**
*STEP, LINEAR, INC=300  Delete LINEAR For E(T)
*STATIC, DIRECT
**initial time increment (s), total time of step
1.0, 103
**
**TEMPERATURE (Users' 7.5.14-1) specifies temperature curves to
**a stress model.  Temperatures are input at nodes; values at the
**integration points are determined by interpolation.  Parameters:AMP -
**this parameter is set equal to the name of the amplitude curve
**defined earlier (e.g., AMP=RR1 specifies that node set R1 follows
**the temperature history defined by RR1.)
**
*TEMPERATURE, AMP=RR1
**node set, magnification factor for amplitude curve
R1, 1.0
*TEMPERATURE, AMP=RR1
R2, 1.0
*TEMPERATURE, AMP=RR1
R3, 1.0
*TEMPERATURE, AMP=RR1
R4, 1.0
*TEMPERATURE, AMP=RR1
R5, 1.0
*TEMPERATURE, AMP=RR1
R6, 1.0
*TEMPERATURE, AMP=RR1
R7, 1.0
*TEMPERATURE, AMP=RR1
R8, 1.0
*TEMPERATURE, AMP=RR1
R9, 1.0
*TEMPERATURE, AMP=RR1
R10, 1.0
*TEMPERATURE, AMP=RR2
R11, 1.0
*TEMPERATURE, AMP=RR2
R12, 1.0
```

```
*TEMPERATURE, AMP=RR3
R13, 1.0
*TEMPERATURE, AMP=RR3
R14, 1.0
*TEMPERATURE, AMP=RR4
R15, 1.0
*TEMPERATURE, AMP=RR5
R16, 1.0
*TEMPERATURE, AMP=RR5
R17,1.0
*TEMPERATURE, AMP=RR6
R18,1.0
*TEMPERATURE, AMP=RR6
R19,1.0
*TEMPERATURE, AMP=RR6
R20,1.0
*TEMPERATURE, AMP=RR6
R21,1.0
*TEMPERATURE, AMP=RR6
R22,1.0
*TEMPERATURE, AMP=RR6
R23,1.0
*TEMPERATURE, AMP=RR6
R24,1.0
*TEMPERATURE, AMP=RR6
R25, 1.0
*TEMPERATURE, AMP=RR6
R26, 1.0
*TEMPERATURE, AMP=RR6
R27, 1.0
*TEMPERATURE, AMP=RR6
R28, 1.0
*TEMPERATURE, AMP=RR6
R29, 1.0
*TEMPERATURE, AMP=RR6
R30, 1.0
*TEMPERATURE, AMP=RR6
R31, 1.0
*TEMPERATURE, AMP=RR6
R32, 1.0
*TEMPERATURE, AMP=RR6
R33, 1.0
*TEMPERATURE, AMP=RR6
R34, 1.0
*TEMPERATURE, AMP=RR6
R35, 1.0
**
**EL PRINT (Users' 7.7.3-1) allows selection of variables to be
**printed.  Parameters:  COORDS - requests cartesian coordinates
**of nodes to appear on output.  FREQ - to request the frequency
**at which output is desired (e.g., FREQ=1 provides output every
**increment.)   TEMPS - requests the temperature at the nodes.
**ELSET - used to specify the elements for which output data is
**desired.
**Further selection of variables to appear as output is made
**through the print request commands: 2=YES, 1=NO.
**First line: stress components, stress invariants, section stress
**components, energy densities, stress based contribution to nodal
**forces.
**Second line: total strain components, plastic strain components,
**creep strain components, inelastic strain, elastic strain.
**components.
**Third Line:  nodal avg. stress components, nodal avg. strain
```

```
**components, strain jump at node, invariants of nodal avg.
**stress components, nodal avg. plastic strain components.
**
*EL PRINT, COORDS, FREQ=1, TEMPS, ELSET=ELSET1
2,2,1,1,1
2,2,2,2,2
1,1,1,1,1,1,1,1
**
**ENDSTEP defines the end of the data that defines a step.
**
*ENDSTEP
```

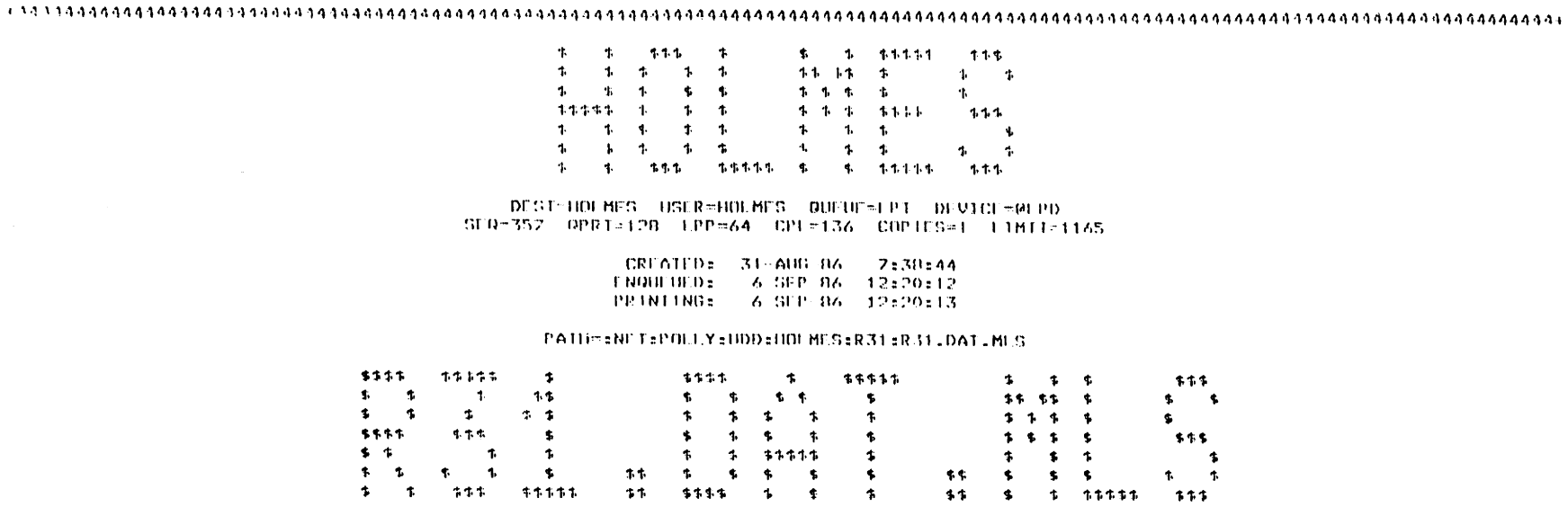

DEST=HOLMES USER=HOLMES QUEUE=LPT DEVICE=(ALPD)
SEQ=352 QPRT=120 LPP=64 CPI=136 COPIES=1 LIMIT=1165

CREATED: 31-AUG 86 7:30:44
ENQUEUED: 6 SEP 86 12:20:12
PRINTING: 6 SEP 86 12:20:13

PATH=\NET\POLLY\UDD\HOLMES\R31\R31.DAT.MLS

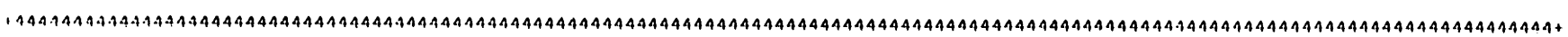

AOS/VS REV 6.03.00.00

AOS/VS REV 06.03
AOS/VS XLPT REV 06.01

ABAQUS input and output files for calculation of thermoelastic

STEP 1 INCREMENT 1

S T E P 1

S T A T I C A N A L Y S I S

USER SPECIFIED INCREMENTS OF 1.00 FOR A TIME PERIOD OF 103.

SMALL DISPLACEMENT THEORY WILL BE USED

MAXIMUM NUMBER OF INCREMENTS ALLOWED IN THIS STEP IS 300
MAXIMUM NUMBER OF ITERATIONS ALLOWED PER INCREMENT IS 1

PRINT OF INCREMENT NUMBER, TIME, ETC., EVERY 1 INCREMENTS

INCREMENT NUMBER 1 ATTEMPT NUMBER 1
TIME INCREMENT = 1.00

TIME COMPLETED DURING THIS STEP 1.00 , TIME INCREMENT COMPLETED IS 1.00 , FRACTION OF STEP IS 9.709E 03
TOTAL ACCUMULATED TIME IS 1.00

E L E M E N T O U T P U T F O R E L S E T ELSET1

ELEMENT 129 POINT 1 COORDINATES 5.4163E 03 6.4527E 03
TEMPERATURE, FIELD VARIABLES 555.
STRESS COMPONENTS 2.240E+07 -1.579E+07 1.914E+07
STRESS INVARIANTS MISES 3.869E+07 TRESCA 3.805E+07 HOU.PRESS 1.273E+07
PRINCIPAL STRESSES 3.853E+07 0.000E 01 3.229E+05
TOTAL STRAIN COMPONENTS 3.999E-04 4.816E 04 1.736E 04
TOTAL PLASTIC STRAIN COMPTS. 1.459E 04 6.424E 05 1.736E-04

ABAQUS input and output files for calculation of thermoelastic STEP 1 INCREMENT 1

ELEMENT 129 POINT 2 COORDINATES 5.6574E 03 6.2432E-03

TEMPERATURE, FIELD VARIABLES	555.				
STRESS COMPONENTS	2.097E+07	1.720E+07	1.931E+07		
STRESS INVARIANTS MISES	3.862E+07	TRESCA	3.879E+07	EQU.PRESS	1.271E+07
PRINCIPAL STRESSES	3.844E+07	0.000E 01	3.330E+05		
TOTAL STRAIN COMPONENTS	4.180E 04	4.640E-04	1.250E 04		
TOTAL ELASTIC STRAIN COMPTS.	1.272E 04	-8.190E-05	1.250E 04		

ELEMENT 129 POINT 3 COORDINATES 5.8908E 03 6.0226E-03

TEMPERATURE, FIELD VARIABLES	555.				
STRESS COMPONENTS	1.934E+07	-1.852E+07	1.926E+07		
STRESS INVARIANTS MISES	3.836E+07	TRESCA	3.853E+07	EQU.PRESS	1.262E+07
PRINCIPAL STRESSES	3.819E+07	0.000E 01	3.370E+05		
TOTAL STRAIN COMPONENTS	4.366E-04	4.468E 04	1.746E-04		
TOTAL ELASTIC STRAIN COMPTS.	1.092E-04	9.905E 05	1.746E 04		

ELEMENT 129 POINT 4 COORDINATES 5.4374E 03 6.4779E-03

TEMPERATURE, FIELD VARIABLES	555.				
STRESS COMPONENTS	2.226E+07	-1.568E+07	1.887E+07		
STRESS INVARIANTS MISES	3.822E+07	TRESCA	3.831E+07	EQU.PRESS	1.265E+07
PRINCIPAL STRESSES	3.812E+07	0.000E-01	1.865E+05		
TOTAL STRAIN COMPONENTS	4.008E 04	4.821E-04	1.710E-04		
TOTAL ELASTIC STRAIN COMPTS.	-1.450E 04	6.372E 05	1.710E-04		

ELEMENT 129 POINT 5 COORDINATES 5.6798E 03 6.2666E 03

TEMPERATURE, FIELD VARIABLES	555.				
STRESS COMPONENTS	2.078E+07	1.708E+07	1.903E+07		
STRESS INVARIANTS MISES	3.815E+07	TRESCA	3.824E+07	EQU.PRESS	1.262E+07
PRINCIPAL STRESSES	3.805E+07	0.000E 01	1.903E+05		
TOTAL STRAIN COMPONENTS	4.188E 04	4.646E-04	1.725E-04		
TOTAL ELASTIC STRAIN COMPTS.	1.270E-04	-8.128E-05	1.725E-04		

ELEMENT 129 POINT 6 COORDINATES 5.9138E 03 6.0442E-03

TEMPERATURE, FIELD VARIABLES	555.				
STRESS COMPONENTS	1.921E+07	1.839E+07	1.898E+07		
STRESS INVARIANTS MISES	3.788E+07	TRESCA	3.797E+07	EQU.PRESS	1.253E+07
PRINCIPAL STRESSES	3.778E+07	0.000E-01	1.870E+05		
TOTAL STRAIN COMPONENTS	4.374E-04	4.475E 04	1.720E-04		
TOTAL ELASTIC STRAIN COMPTS.	-1.085E-04	9.836E-05	1.720E 04		

ELEMENT 129 POINT 7 COORDINATES 5.4586E 03 6.5031E-03

TEMPERATURE, FIELD VARIABLES	555.				
STRESS COMPONENTS	2.211E+07	-1.552E+07	1.860E+07		
STRESS INVARIANTS MISES	3.775E+07	TRESCA	3.777E+07	EQU.PRESS	1.256E+07
PRINCIPAL STRESSES	3.773E+07	0.000E 01	4.414E+04		

TOTAL STRAIN COMPONENTS	1.612E-04	4.824E-04	1.684E-04		
TOTAL ELASTIC STRAIN COMPTS.	1.431E-04	-6.392E-05	1.686E-04		

ELEMENT 129 POINT 8 COORDINATES -5.7019E-03 6.2910E-03

TEMPERATURE, FIELD VARIABLES	555.				
STRESS COMPONENTS	2.064E+07	-1.624E+07	1.874E+07		
STRESS INVARIANTS - MISES	3.767E+07	TRESCA	3.770E+07	EQU.PRESS	1.256E+07
PRINCIPAL STRESSES	3.765E+07	0.000E-01	4.712E+04		
TOTAL STRAIN COMPONENTS	4.174E-04	4.652E-04	1.700E-04		
TOTAL ELASTIC STRAIN COMPTS.	1.262E-04	8.042E-05	1.700E-04		

ELEMENT 129 POINT 9 COORDINATES -5.9368E-03 6.0692E-03

TEMPERATURE, FIELD VARIABLES	555.				
STRESS COMPONENTS	-1.908E+07	-1.826E+07	1.870E+07		
STRESS INVARIANTS - MISES	3.740E+07	TRESCA	3.741E+07	EQU.PRESS	1.245E+07
PRINCIPAL STRESSES	-3.738E+07	0.000E-01	3.688E+04		
TOTAL STRAIN COMPONENTS	4.381E-04	4.482E-04	1.695E-04		
TOTAL ELASTIC STRAIN COMPTS.	1.078E-04	-9.769E-05	1.695E-04		

ELEMENT 136 POINT 1 COORDINATES 2.3263E-05 8.4240E-03

TEMPERATURE, FIELD VARIABLES	555.				
STRESS COMPONENTS	-5.014E+07	4.372E+05	5.571E+05		
STRESS INVARIANTS - MISES	5.037E+07	TRESCA	5.059E+07	EQU.PRESS	1.657E+07
PRINCIPAL STRESSES	-5.015E+07	0.000E-01	4.433E+05		
TOTAL STRAIN COMPONENTS	9.645E-05	7.213E-04	5.049E-06		
TOTAL ELASTIC STRAIN COMPTS.	4.494E-04	1.759E-04	5.049E-06		

ELEMENT 136 POINT 2 COORDINATES 4.1337E-04 8.4144E-03

TEMPERATURE, FIELD VARIABLES	555.				
STRESS COMPONENTS	-4.976E+07	3.359E+05	2.508E+06		
STRESS INVARIANTS - MISES	5.011E+07	TRESCA	5.034E+07	EQU.PRESS	1.647E+07
PRINCIPAL STRESSES	-4.988E+07	0.000E-01	4.612E+05		
TOTAL STRAIN COMPONENTS	1.002E-04	7.195E-04	2.273E-05		
TOTAL ELASTIC STRAIN COMPTS.	4.456E-04	1.737E-04	2.273E-05		

ELEMENT 136 POINT 3 COORDINATES 7.3288E-04 8.3926E-03

TEMPERATURE, FIELD VARIABLES	555.				
STRESS COMPONENTS	-4.939E+07	4.288E+04	4.449E+06		
STRESS INVARIANTS - MISES	5.001E+07	TRESCA	5.023E+07	EQU.PRESS	1.645E+07
PRINCIPAL STRESSES	4.979E+07	0.000E-01	4.401E+05		
TOTAL STRAIN COMPONENTS	1.045E-04	7.157E-04	4.032E-05		
TOTAL ELASTIC STRAIN COMPTS.	4.413E-04	1.698E-04	4.032E-05		

ELEMENT 136 POINT 4 COORDINATES 9.3629E-05 8.4570E-03

TEMPERATURE, FIELD VARIABLES	555.				

ABAQUS input and output files for calculation of thermoelastic STEP 1 INCREMENT 1

STRESS COMPONENTS	-5.014E+07	2.395E+05	5.425E+05		
STRESS INVARIANTS - MISES	5.021E+07	TRESCA	5.040E+07	EQU.PRESS	1.663E+07
PRINCIPAL STRESSES	-5.015E+07	0.000E-01	2.453E+05		
TOTAL STRAIN COMPONENTS	9.709E-05	7.200E-04	4.917E-06		
TOTAL PLASTIC STRAIN COMPTS.	-4.488E-04	1.742E-04	4.917E-06		

ELEMENT 136 POINT 5 COORDINATES 4.1500E-04 8.4473E-03

TEMPERATURE, FIELD VARIABLES 555.

STRESS COMPONENTS	-4.975E+07	1.409E+05	2.479E+06		
STRESS INVARIANTS - MISES	5.001E+07	TRESCA	5.014E+07	EQU.PRESS	1.654E+07
PRINCIPAL STRESSES	-4.988E+07	0.000E-01	2.637E+05		
TOTAL STRAIN COMPONENTS	1.009E-04	7.178E-04	2.247E-05		
TOTAL PLASTIC STRAIN COMPTS.	-4.449E-04	1.719E-04	2.247E-05		

ELEMENT 136 POINT 6 COORDINATES 7.3577E-04 8.4254E-03

TEMPERATURE, FIELD VARIABLES 555.

STRESS COMPONENTS	-4.938E+07	-1.477E+05	4.404E+06		
STRESS INVARIANTS - MISES	4.989E+07	TRESCA	5.001E+07	EQU.PRESS	1.651E+07
PRINCIPAL STRESSES	-4.977E+07	0.000E-01	2.432E+05		
TOTAL STRAIN COMPONENTS	1.052E-04	7.139E-04	3.992E-05		
TOTAL PLASTIC STRAIN COMPTS.	-4.406E-04	1.681E-04	3.992E-05		

ELEMENT 136 POINT 7 COORDINATES 9.3926E-05 8.4099E-03

TEMPERATURE, FIELD VARIABLES 555.

STRESS COMPONENTS	-5.015E+07	4.126E+04	5.280E+05		
STRESS INVARIANTS - MISES	5.018E+07	TRESCA	5.020E+07	EQU.PRESS	1.670E+07
PRINCIPAL STRESSES	-5.015E+07	0.000E-01	4.751E+04		
TOTAL STRAIN COMPONENTS	9.774E-05	7.183E-04	4.785E-06		
TOTAL PLASTIC STRAIN COMPTS.	-4.481E-04	1.724E-04	4.785E-06		

ELEMENT 136 POINT 8 COORDINATES 4.1662E-04 8.4802E-03

TEMPERATURE, FIELD VARIABLES 555.

STRESS COMPONENTS	-4.975E+07	-5.403E+04	2.449E+06		
STRESS INVARIANTS - MISES	4.991E+07	TRESCA	4.994E+07	EQU.PRESS	1.660E+07
PRINCIPAL STRESSES	-4.987E+07	0.000E-01	6.639E+04		
TOTAL STRAIN COMPONENTS	1.016E-04	7.160E-04	2.220E-05		
TOTAL PLASTIC STRAIN COMPTS.	-4.443E-04	1.702E-04	2.220E-05		

ELEMENT 136 POINT 9 COORDINATES 7.3865E-04 8.4582E-03

TEMPERATURE, FIELD VARIABLES 555.

STRESS COMPONENTS	-4.937E+07	-3.382E+05	4.359E+06		
STRESS INVARIANTS - MISES	4.970E+07	TRESCA	4.980E+07	EQU.PRESS	1.657E+07
PRINCIPAL STRESSES	-4.976E+07	0.000E-01	4.640E+04		
TOTAL STRAIN COMPONENTS	1.040E-04	7.122E-04	3.951E-05		
TOTAL PLASTIC STRAIN COMPTS.	-4.392E-04	1.663E-04	3.951E-05		

ABAQUS input and output files for elimination of thermoplastic

STEP 1 INCREMENT 2

INCREMENT NUMBER 2 ATTEMPT NUMBER 1
TIME INCREMENT = 1.00

TIME COMPLETED DURING THIS STEP 2.00 , TIME INCREMENT COMPLETED IS 1.00 , FRACTION OF STEP IS 1.942E-02
TOTAL ACCUMULATED TIME IS 2.00

E L E M E N T O U T P U T F O R E L S E T ELSET1

ELEMENT 129 POINT 1 COORDINATES 5.4163E-03 6.4527E-03
TEMPERATURE, FIELD VARIABLES 657.

STRESS COMPONENTS	-7.409E+07	-5.531E+07	5.467E+07		
STRESS INVARIANTS - MISES	1.158E+08	TRESCA	1.202E+08	EQU.PRESS	4.314E+07
PRINCIPAL STRESSES	-1.202E+08	-9.237E+06	0.000E-01		
TOTAL STRAIN COMPONENTS	1.577E-03	1.820E-03	5.130E-04		
TOTAL PLASTIC STRAIN COMPTS.	4.910E-04	2.420E-04	5.130E-04		

ELEMENT 129 POINT 2 COORDINATES 5.6576E-03 6.2422E 03
TEMPERATURE, FIELD VARIABLES 657.

STRESS COMPONENTS	-6.988E+07	5.931E+07	5.512E+07		
STRESS INVARIANTS - MISES	1.156E+08	TRESCA	1.200E+08	EQU.PRESS	4.306E+07
PRINCIPAL STRESSES	1.200E+08	-9.219E+06	0.000E-01		
TOTAL STRAIN COMPONENTS	1.631E-03	1.760E-03	5.173E-04		
TOTAL PLASTIC STRAIN COMPTS.	4.382E-04	-3.015E-04	5.173E-04		

ELEMENT 129 POINT 3 COORDINATES 5.8908E 03 6.0226E-03
TEMPERATURE, FIELD VARIABLES 657.

STRESS COMPONENTS	-6.545E+07	-6.310E+07	5.506E+07		
STRESS INVARIANTS - MISES	1.150E+08	TRESCA	1.193E+08	EQU.PRESS	4.285E+07
PRINCIPAL STRESSES	-1.193E+08	-9.201E+06	0.000E-01		
TOTAL STRAIN COMPONENTS	1.686E-03	1.716E-03	5.167E-04		
TOTAL PLASTIC STRAIN COMPTS.	-3.832E-04	3.528E-04	5.167E-04		

ELEMENT 129 POINT 4 COORDINATES 5.4374E-03 6.4779E 03
TEMPERATURE, FIELD VARIABLES 657.

STRESS COMPONENTS	-7.377E+07	5.507E+07	5.397E+07		
STRESS INVARIANTS - MISES	1.147E+08	TRESCA	1.192E+08	EQU.PRESS	4.295E+07
PRINCIPAL STRESSES	-1.192E+08	9.644E+06	0.000E-01		

```
      TOTAL STRAIN COMPONENTS      1.590E-03  1.821E-03  5.065E-04
   TOTAL ELASTIC STRAIN COMPTS.   -4.897E-04 -2.479E-04  5.065E-04


ELEMENT  129  POINT    5  COORDINATES  5.6798E-03  6.3666E-03
   TEMPERATURE, FIELD VARIABLES      657.
            STRESS COMPONENTS    -6.957E+07 -5.904E+07  5.442E+07
   STRESS INVARIANTS  -  MISES    1.145E+08     TRESCA   1.190E+08 EQU.PRESS   4.287E+07
      PRINCIPAL STRESSES          -1.190E+08 -9.629E+06  0.000E-01
       TOTAL STRAIN COMPONENTS    1.633E-03  1.769E-03  5.107E-04
   TOTAL ELASTIC STRAIN COMPTS.   -4.362E-04 -3.001E-04  5.107E-04


ELEMENT  129  POINT    6  COORDINATES  5.9138E-03  6.0462E-03
   TEMPERATURE, FIELD VARIABLES      657.
            STRESS COMPONENTS    -6.516E+07 -6.282E+07  5.434E+07
   STRESS INVARIANTS  -  MISES    1.138E+08     TRESCA   1.183E+08 EQU.PRESS   4.266E+07
      PRINCIPAL STRESSES          -1.183E+08 -9.634E+06  0.000E-01
       TOTAL STRAIN COMPONENTS    1.688E-03  1.718E-03  5.100E-04
   TOTAL ELASTIC STRAIN COMPTS.   -3.815E-04 -3.512E-04  5.100E-04


ELEMENT  129  POINT    7  COORDINATES  5.4586E-03  6.5031E-03
   TEMPERATURE, FIELD VARIABLES      657.
            STRESS COMPONENTS    -7.346E+07 -5.483E+07  5.329E+07
   STRESS INVARIANTS  -  MISES    1.135E+08     TRESCA   1.182E+08 EQU.PRESS   4.276E+07
      PRINCIPAL STRESSES          -1.182E+08 -1.005E+07  0.000E-01
       TOTAL STRAIN COMPONENTS    1.582E-03  1.822E-03  5.000E-04
   TOTAL ELASTIC STRAIN COMPTS.   -4.876E-04 -2.468E-04  5.000E-04


ELEMENT  129  POINT    8  COORDINATES  5.7019E-03  6.2910E-03
   TEMPERATURE, FIELD VARIABLES      657.
            STRESS COMPONENTS    -6.927E+07 -5.878E+07  5.373E+07
   STRESS INVARIANTS  -  MISES    1.133E+08     TRESCA   1.180E+08 EQU.PRESS   4.268E+07
      PRINCIPAL STRESSES          -1.180E+08 -1.004E+07  0.000E-01
       TOTAL STRAIN COMPONENTS    1.635E-03  1.771E-03  5.042E-04
   TOTAL ELASTIC STRAIN COMPTS.   -4.344E-04 -2.987E-04  5.042E-04


ELEMENT  129  POINT    9  COORDINATES  5.9368E-03  6.0497E-03
   TEMPERATURE, FIELD VARIABLES      657.
            STRESS COMPONENTS    -6.488E+07 -6.255E+07  5.363E+07
   STRESS INVARIANTS  -  MISES    1.127E+08     TRESCA   1.174E+08 EQU.PRESS   4.247E+07
      PRINCIPAL STRESSES          -1.174E+08 -1.007E+07  0.000E-01
       TOTAL STRAIN COMPONENTS    1.689E-03  1.720E-03  5.033E-04
   TOTAL ELASTIC STRAIN COMPTS.   -3.798E-04 -3.497E-04  5.033E-04


ELEMENT  136  POINT    1  COORDINATES  9.3263E-05  8.4240E-03
   TEMPERATURE, FIELD VARIABLES      657.
```

ABAQUS input and output files for circulation of thermoplastic STEP 1 INCREMENT 2

STRESS COMPONENTS	1.426E+08	9.414E+06	1.465E+06		
STRESS INVARIANTS — MISES	1.387E+08	TRESCA	1.426E+08	EQU.PRESS	5.062E+07
PRINCIPAL STRESSES	1.426E+08	9.398E+06	0.000E-01		
TOTAL STRAIN COMPONENTS	7.230E-04	2.425E-03	1.325E-05		
TOTAL ELASTIC STRAIN COMPTS.	1.296E-03	4.259E-04	1.325E-05		

ELEMENT 136 POINT 2 COORDINATES 4.1332E-04 8.4144E-03

TEMPERATURE, FIELD VARIABLES	657.				
STRESS COMPONENTS	1.419E+08	-9.694E+06	6.607E+06		
STRESS INVARIANTS — MISES	1.378E+08	TRESCA	1.422E+08	EQU.PRESS	5.053E+07
PRINCIPAL STRESSES	1.422E+08	-9.365E+06	0.000E-01		
TOTAL STRAIN COMPONENTS	7.806E-04	2.490E-03	6.200E-05		
TOTAL ELASTIC STRAIN COMPTS.	1.289E-03	4.208E-04	6.200E-05		

ELEMENT 136 POINT 3 COORDINATES 7.3288E-04 8.3926E-03

TEMPERATURE, FIELD VARIABLES	657.				
STRESS COMPONENTS	1.411E+08	-1.042E+07	1.172E+07		
STRESS INVARIANTS — MISES	1.377E+08	TRESCA	1.421E+08	EQU.PRESS	5.051E+07
PRINCIPAL STRESSES	1.421E+08	-9.374E+06	0.000E-01		
TOTAL STRAIN COMPONENTS	7.906E-04	2.480E-03	1.100E-04		
TOTAL ELASTIC STRAIN COMPTS.	1.279E-03	4.119E-04	1.100E-04		

ELEMENT 136 POINT 4 COORDINATES 9.3629E-05 8.4570E-03

TEMPERATURE, FIELD VARIABLES	657.				
STRESS COMPONENTS	-1.425E+08	9.933E+06	1.438E+06		
STRESS INVARIANTS — MISES	1.378E+08	TRESCA	1.425E+08	EQU.PRESS	5.080E+07
PRINCIPAL STRESSES	-1.425E+08	-9.918E+06	0.000E-01		
TOTAL STRAIN COMPONENTS	7.761E-04	2.490E-03	1.349E-05		
TOTAL ELASTIC STRAIN COMPTS.	1.293E-03	4.206E-04	1.349E-05		

ELEMENT 136 POINT 5 COORDINATES 4.1500E-04 8.4473E-03

TEMPERATURE, FIELD VARIABLES	657.				
STRESS COMPONENTS	1.418E+08	1.021E+07	6.548E+06		
STRESS INVARIANTS — MISES	1.374E+08	TRESCA	1.421E+08	EQU.PRESS	5.065E+07
PRINCIPAL STRESSES	1.421E+08	-9.883E+06	0.000E-01		
TOTAL STRAIN COMPONENTS	7.838E-04	2.485E-03	6.145E-05		
TOTAL ELASTIC STRAIN COMPTS.	1.285E-03	4.154E-04	6.145E-05		

ELEMENT 136 POINT 6 COORDINATES 7.3577E-04 8.4254E-03

TEMPERATURE, FIELD VARIABLES	657.				
STRESS COMPONENTS	1.409E+08	-1.092E+07	1.163E+07		
STRESS INVARIANTS — MISES	1.373E+08	TRESCA	1.420E+08	EQU.PRESS	5.062E+07
PRINCIPAL STRESSES	1.420E+08	-9.889E+06	0.000E-01		
TOTAL STRAIN COMPONENTS	7.940E-04	2.475E-03	1.092E-04		
TOTAL ELASTIC STRAIN COMPTS.	1.275E-03	4.059E-04	1.092E-04		

ELEMENT 136 POINT 7 COORDINATES 9.3926E-05 8.4822E-03

ABAQUS input and output files for calculation of thermoplastic STEP 1 INCREMENT 2

TEMPERATURE, FIELD VARIABLES	657.				
STRESS COMPONENTS	-1.423E+08	-1.045E+07	1.411E+06		
STRESS INVARIANTS - MISES	1.324E+08	TRESCA	1.424E+08	EQU.PRESS	5.093E+07
PRINCIPAL STRESSES	-1.424E+08	-1.044E+07	0.000E-01		
TOTAL STRAIN COMPONENTS	7.792E-04	2.485E-03	1.324E-05		
TOTAL ELASTIC STRAIN COMPTS.	1.220E-03	4.153E-04	1.324E-05		

ELEMENT 136 POINT 8 COORDINATES 4.1662E-04 8.4802E-03

TEMPERATURE, FIELD VARIABLES	657.				
STRESS COMPONENTS	1.416E+08	-1.072E+07	6.489E+06		
STRESS INVARIANTS - MISES	1.370E+08	TRESCA	1.419E+08	EQU.PRESS	5.077E+07
PRINCIPAL STRESSES	1.419E+08	-1.040E+07	0.000E-01		
TOTAL STRAIN COMPONENTS	7.871E-04	2.479E-03	6.090E-05		
TOTAL ELASTIC STRAIN COMPTS.	-1.282E-03	4.101E-04	6.090E-05		

ELEMENT 136 POINT 9 COORDINATES 7.3865E-04 8.4582E-03

TEMPERATURE, FIELD VARIABLES	657.				
STRESS COMPONENTS	-1.408E+08	-1.142E+07	1.154E+07		
STRESS INVARIANTS - MISES	1.369E+08	TRESCA	1.418E+08	EQU.PRESS	5.073E+07
PRINCIPAL STRESSES	-1.418E+08	-1.040E+07	0.000E-01		
TOTAL STRAIN COMPONENTS	7.973E-04	2.470E-03	1.083E-04		
TOTAL ELASTIC STRAIN COMPTS.	-1.272E-03	4.006E-04	1.083E-04		

INCREMENT NUMBER 3 ATTEMPT NUMBER 1
TIME INCREMENT = 1.00

TIME COMPLETED DURING THIS STEP 3.00 , TIME INCREMENT COMPLETED IS 1.00 , FRACTION OF STEP IS 2.913E-02
TOTAL ACCUMULATED TIME IS 3.00

E L E M E N T O U T P U T F O R E L S E T ELSET1

ELEMENT 129 POINT 1 COORDINATES 5.4163E-03 6.4527E-03

TEMPERATURE, FIELD VARIABLES	767.				
STRESS COMPONENTS	-1.295E+08	-9.948E+07	8.797E+07		
STRESS INVARIANTS - MISES	1.923E+08	TRESCA	2.037E+08	EQU.PRESS	7.632E+07
PRINCIPAL STRESSES	-2.037E+08	-2.524E+07	0.000E-01		
TOTAL STRAIN COMPONENTS	3.000E-03	3.412E-03	8.608E-04		
TOTAL ELASTIC STRAIN COMPTS.	-8.962E-04	-4.840E-04	8.608E-04		

ELEMENT 129 POINT 2 COORDINATES 5.6576E-03 6.2422E-03

Appendix C

Calculation of Equilibrium SO_2-O_2-SO_3 Composition for the Test Conditions of Chapter 4

Free energy in terms of temperature and partial pressures.

The chemical equation for the SO_2-SO_3-O_2 reaction is

$$SO_2 + (1/2)O_2 = SO_3 \,. \qquad (C1)$$

The temperature variation of the free energy change in Joules for this reaction is

$$\Delta G^0 = -94{,}560 + 89.37\,T \quad (T \text{ in degrees Kelvin}). \qquad (C2)$$

Assuming ideal gas behavior gives the free energy change at equilibrium in terms of the partial pressures of the gas components P_i and a reference pressure P^0 :

$$\Delta G^0 = -RT\ln\left[(P_{SO_3}/p^0)/(P_{SO_2}/p^0)(P_{O_2}/p^0)^{1/2}\right] .$$

For a reference pressure of 1 atm

$$\Delta G^0 = -RT\ln\left[P_{SO_3}/P_{SO_2}(P_{O_2})^{1/2}\right] . \qquad (C3)$$

Calculation of P_{SO_3}, P_{SO_2}, and P_{O_2} at equilibrium. Denoting the initial moles of the gaseous components as $n^i_{SO_2}$, $n^i_{O_2}$, and $n^i_{SO_3}$, and denoting the moles of SO_2 that react by x gives the following relations between initial and equilibrium mole fractions from the stoichiometry of reaction C1:

	SO_2	+	$(1/2)O_2$	=	SO_3
initial moles:	$n^i_{SO_2}$		$n^i_{O_2}$		0
moles at equil.:	$(n^i_{SO_2} - x)$		$(n^i_{O_2} - 0.5x)$		x

The partial pressure P_j exerted by the j^{th} component of an ideal gas mixture is related to its mole fraction n_j/n_{total}, and the total gas pressure P_{total} by

$$P_j = (n_j/n_{total})\, P_{total} \quad [atm]\,. \qquad (C4)$$

If the above gas mixture contains an inert component (e.g., A),

the total number of moles at equilibrium is

$$n_{total} = n^i_{SO_2} + n^i_{O_2} + n_A - 0.5x \ . \qquad (C5)$$

Therefore, the equilibrium partial pressures of SO_2, O_2, and SO_3 are:

$$P_{SO_2} = (n^i_{SO_2} - x)P_{total} / (n^i_{SO_2} + n^i_{O_2} + n_A - 0.5x), \qquad (C6)$$

$$P_{O_2} = (n^i_{O_2} - 0.5x)P_{total} / (n^i_{SO} + n^i_{O_2} + n_A - 0.5x), \qquad (C7)$$

$$P_{SO_3} = x P_{total}/(n^i_{SO_2} + n^i_{O_2} + n_A - 0.5x), \qquad (C8)$$

$$P_A = n_A P_{total}/ (n^i_{SO_2} + n^i_{O_2} + n_A - 0.5x) \ , \qquad (C9)$$

Substituting these expressions for partial pressure into Eq. C3 gives,

$$\Delta G^0 = - RT \ln \left[x(n_{total})^{1/2} / (n^i_{SO_2} - x) (n^i_{O_2} - 0.5x)^{1/2} (P_{total})^{1/2} \right]. \qquad (C10)$$

Calculation of equilibrium gas composition for the test conditions employed in Chapter 4. On a volumetric basis, the initial composition of the gas mixture entering the furnace hot zone is: 0.01% SO_2, 20.00% O_2, and 79.99% A. Therefore, based upon one mole of total gas mixture, the initial moles of each component are: $n^i_{SO_2} = 1.00 \times 10^{-4}$, $n^i_{O_2} = 20.00 \times 10^{-2}$, $n^i_{SO_3} = 0$ and $n_A = 79.99 \times 10^{-2}$.

For a gas temperature of 1203 K in the furnace hot zone, Eq. C2 gives $\Delta G^0(1203\ K) = 12{,}950$ Joules. Substituting the above values into Eq. C10 and solving iteratively, gives $x = 1.1 \times 10^{-5}$ moles.

From Eqs. C6-C9, the equilibrium partial pressures of SO_2, SO_3, O_2, and A are: 8.90×10^{-5} atm SO_2, 1.1×10^{-5} atm SO_3, 20.00×10^{-2} atm O_2, and 79.99×10^{-2} atm A. The initial and equilibrium gas compositions are summarized in Table C1.

Table C1 Summary of initial and equilibrium gas compositions.

Moles	SO_2	O_2	SO_3	A
n_i	1.00×10^{-4}	20.00×10^{-2}	0	79.99×10^{-2}
n_{equil}	8.90×10^{-5}	20.00×10^{-2}	1.10×10^{-5}	79.99×10^{-2}